Observation of spontaneous density-wave patterns using a quantum gas magnifier
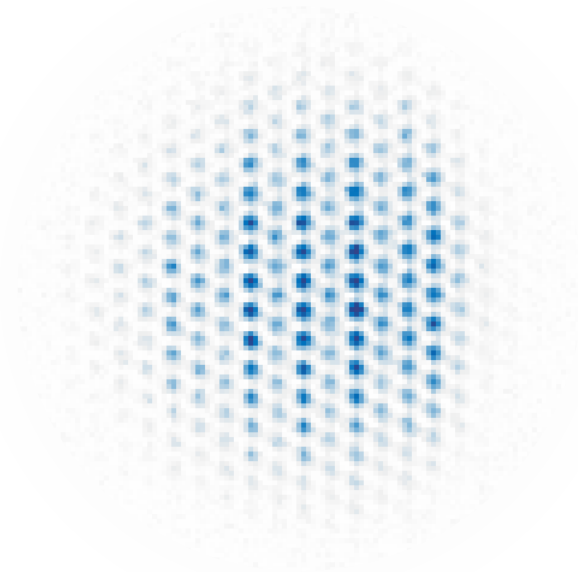
Dissertation

zur Erlangung des Doktorgrades
an der Fakultät für Mathematik, Informatik und Naturwissenschaften
Fachbereich Physik

der Universität Hamburg

vorgelegt von
Henrik Pascal Zahn
aus Konstanz

Hamburg
2022

Gutachter

Gutachter der Dissertation:	Prof. Dr. Klaus Sengstock
	Prof. Dr. Ludwig Mathey
Gutachter der Disputation:	Prof. Dr. Klaus Sengstock
	Prof. Dr. Ludwig Mathey
	Prof. Dr. Michael Potthoff
	Prof. Dr. Ralf Riedinger
	Dr. Guillaume Salomon
Vorsitzender der Prüfungskommission:	Prof. Dr. Michael Potthoff
Datum der Disputation:	08. September 2022
Vorsitzender des Promotionsausschusses:	Prof. Dr. Wolfgang J. Parak
Leiter des Fachbereichs PHYSIK:	Prof. Dr. Günter H. W. Sigl
Dekan der Fakultät für Mathematik, Informatik und Naturwissenschaften:	Prof. Dr. Heinrich Graener

Erklärung zur Eigenständigkeit

Hiermit versichere ich an Eides statt, die vorliegende Dissertationsschrift selbst verfasst und keine anderen als die angegebenen Hilfsmittel und Quellen benutzt zu haben. Wörtlich oder dem Sinn nach aus anderen Werken entnommene Stellen sind unter Angabe der Quellen kenntlich gemacht.

Henrik Pascal Zahn   *Hamburg – 13.5.2022*

Abstract

This thesis reports the implementation of a matter wave optics protocol for the magnification of quantum gases. The protocol consists of a quarter period evolution in a harmonic trap followed by a free expansion. Subsequently, we image the magnified density distribution via standard absorption imaging. We reach a magnification of more than 90, allowing for sub-lattice site resolved imaging of the atomic density in an optical lattice with a lattice constant of $709\,\text{nm}$. The technique overcomes several limitations of established methods as it has very large depth of focus, does not induce light assisted collisions, and records the density in a single shot. We benchmark the method by high precision thermometry of the normal to superfluid transition and demonstrate its capabilities by achieving pattern preparation using magnetic resonance techniques, by presenting measurements of sub-lattice site dynamics, and by an analysis of thermal and quantum fluctuations of on-site populations.

In a next step we leverage the advantages of the quantum gas magnifier to observe spontaneous pattern formation in a Bose-Einstein condensate in a tilted triangular lattice with weak transverse confinement, i.e., in a three-dimensional system. To the best of our knowledge, this phenomenon was not observed or predicted beforehand and explicitly requires the capabilities of matter wave magnification to be visible. We explain the observation by a theoretical modelling in terms of an effective Hamiltonian for large tilts and in terms of a c-field numerical simulation.

Zusammenfassung

Diese Dissertation berichtet die Implementierung eines Materiewellenoptikprotokolls zur Vergrößerung von Quantengasen. Das Protokoll besteht aus einer Zeitentwicklung in einer harmonischen Falle für die Dauer einer Viertelperiode gefolgt von einer freien Expansion. Anschließend bilden wir die vergrößerte Dichteverteilung durch Standard Absorptionsabbildung ab. Wir erreichen eine Vergrößerung von mehr als 90, was subgitteraufgelöste Abbildung der atomaren Dichte in einem optischen Gitter mit einer Gitterkonstante von 709 nm erlaubt. Die Technik überwindet mehrere Limitierungen etablierter Methoden, da sie sehr große Tiefenschärfe hat, keine lichtinduzierten Stöße verursacht und die Dichte in einem einzigen Schuss aufnimmt. Wir benchmarken die Methode durch Hochpräzisionsthermometrie des normal zu superfluid Übergangs und zeigen ihre Fähigkeiten durch Präparation von Mustern unter Benutzung von Magnetresonanztechniken, durch die Darstellung von sub-Gitterplatzdynamik und durch eine Analyse von thermischen und Quantenfluktuationen von Gitterplatzbesetzungen.

In einem nächsten Schritt nutzen wir die Vorteile des Quantengasvergrößerers um spontane Musterbildung in einem Bose-Einstein Kondensat in einem verkippten Dreiecksgitter mit schwachem Einschluss, d.h. in einem dreidimensionalen System, zu beobachten. Nach bestem Wissen wurde dieses Phänomen zuvor weder beobachtet noch vorhergesagt und benötigt explizit die Fähigkeiten des Quantengasvergrößerers um sichtbar zu sein. Wir erklären die Beobachtung durch theoretische Modellierung mit einem effektiven Hamiltonian für große Verkippung und durch eine numerische c-Feld Simulation.

Contents

1. Introduction

Spontaneous symmetry breaking is a central concept in physics. It describes a state that does not respect the symmetry of the Hamiltonian of the system. Most of the time this concept is encountered in ground states ranging from examples in condensed matter—like the spin orientation in a ferromagnet—all the way to particle physics where the spontaneous symmetry breaking of the Higgs field determines the mass of fundamental particles [1, 2]. But also out of equilibrium the phenomenon of spontaneous symmetry breaking arises, e.g., in the form of pattern formation [3]. There are numerous examples comprising condensed matter [4], non-linear optics [5], fluid dynamics [6], convection [7], or morphogenesis [8, 9].

Ultracold atoms are very controlled experimental systems which are therefore well-suited for quantum simulation [10]. A large variety of paradigmatic models such as the Hubbard model, various types of spin models or topological models can be implemented with the right choice of element, isotope, laser setup, and magnetic fields. As such ultracold atom experiments also shed light on the intriguing topic of pattern formation. Recent results include, e.g., Z_2 symmetry breaking in the tilted Mott insulator [11–13], pattern formation in a Rydberg tweezer array [14] as well as in a Bose-Einstein condensate [15], and the observation of a supersolid [16]. In this thesis we report the observation of spontaneous pattern formation in a tilted triangular lattice. In contrast to the aforementioned tilted Mott insulators we work in a superfluid regime with around 10^3 atoms per lattice site. The confinement perpendicular to the lattice plane is weak, hence the system is forming a lattice of tubes. In this regime, experiments with accelerated [17–19] or shaken [20] lattices were performed previously, as well as experiments where the external trap was quickly reduced [21], resulting in patterns either large enough to be resolved without single-site resolution or periodic ones with coherence which hence can be detected after a free expansion of the gas via its interference pattern. Here we use quantum gas magnification, a new technique developed in the course of this thesis [22], which enables us to resolve spontaneous patterns in lattice of tubes systems with single site resolution as outlined in the following.

The quantum gas magnifier is based on matter wave optics. First, a quarter period evolution in a harmonic trap maps the particles' positions onto their momenta. Subsequently all trapping potentials are abruptly switched off resulting in a free expansion which maps momentum back to position in the limit of infinite expansion time. Actually, we can show that a slight adjustment of the hold time in the harmonic trap allows to reach an exact mapping back to position even for finite expansion time. The idea of using a harmonic trap as a matter wave lens goes back to the technique of

matter wave focusing [23] and is used in setups with very good real space resolution to map momentum to position which can then be imaged without the need of a long free expansion [24–28]. More involved protocols combining different trap frequencies or manipulation in the Fourier plane were proposed [29]. The technique introduced in this thesis significantly enriches the real space imaging tool box in the discipline of ultracold atoms. Here the most prominent method in the field is quantum gas microscopy [30–32] where an objective with high numerical aperture is used to obtain single-site resolution. However, this implies that the depth of focus is small, restricting this technique to two-dimensional systems. Quantum gas magnification imposes only little constraints on the resolution of the optical imaging thus allowing for single site resolution and large depth of focus at the same time, enabling the imaging of three-dimensional systems integrated along the line of sight. Electron scanning microscopy [33] or ion microscopy [34] are also able to image three dimensional systems, at the cost of being a scanning technique or the need of ionizing the sample, respectively. Furthermore, quantum gas magnification can enlarge the sample to such a degree that even features below the scale of a lattice constant, such as the motion on a singular lattice site, can be resolved. Superresolution microscopy [35, 36] also offers this possibility but as a global probe it assumes the density of all lattice sites being equal and is furthermore a scanning technique. In fact, for the observation of spontaneous density patterns in a lattice of tubes, as described in this thesis, none of the mentioned established methods would be suitable since the pattern would wash out, either due to the implicit averaging connected to scanning or due to blurring connected to small depth of focus.

Thesis Outline

This thesis is organized as follows. In chapter 2 the experimental sequence from room temperature vapour to a Bose-Einstein condensate (BEC) is explained, as well as the optical lattice, and the detection via absorption imaging. In chapter 3 we introduce the quantum gas magnifier technique. The working principle is illustrated and experimental characterization of the resolution is shown. We present experiments on the normal to superfluid phase transition, pattern preparation via magnetic resonance, sub-lattice site dynamics, and on-site atom number fluctuations. We proceed with chapter 4 where we present the observation of spontaneous pattern formation in a tilted triangular lattice. We explain two possible theoretical perspectives: an effective Hamiltonian description for strong tilt and a numerical approach in the form of a c-field simulation. We investigate the domain statistics of the pattern, its formation dynamics and decay, and its dependence on various system parameters.

List of Publications

The following research articles have been published in the course of this thesis. Im Rahmen der vorliegenden Arbeit sind die folgenden wissenschaftlichen Veröffentlichungen entstanden.

- **Quantum gas magnifier for sub-lattice-resolved imaging of 3D quantum systems**

  L. Asteria, H. P. Zahn, M. N. Kosch, K. Sengstock, C. Weitenberg
  Nature **599**, 571-575 (2021)
  DOI: 10.1038/s41586-021-04011-2

- **Formation of Spontaneous Density-Wave Patterns in dc Driven Lattices**

  H. P. Zahn, V. P. Singh, M. N. Kosch, L. Asteria, L. Freystatzky,
  K. Sengstock, L. Mathey, C. Weitenberg
  Physical Review X **12**, 021014 (2022)
  DOI: 10.1103/PhysRevX.12.021014

2. The quantum gas machine

Quantum many-body physics is extremely relevant for the understanding of numerous phenomena [37]. However, due to the typically very large Hilbert spaces required for such problems it is only possible to simulate systems of small particle number on classical computers. One approach to circumvent this limitation is the mapping of a physical question onto another system which can be studied in a controlled way, which is known as analogue quantum simulation [38]. In this chapter we will introduce our quantum gas machine which is a quantum simulation platform using ultracold atoms in optical lattices and, for the most part, has been set up by earlier generations of students. My colleagues Luca Asteria, Marcel Kosch and I mainly implemented the multi-frequency lattice, which will be explained. Concerning the setup, we will summarize the most important facts here. Details can be found, e.g., in references [39–41]—to name only the first theses—and in appendix A.

2.1. Quantum simulation with ultracold atoms in optical lattices

Ultracold atoms in optical lattices are an established platform for the quantum simulation of solid state physics [42]. The atoms take the role of the electrons and the optical lattice takes the role of the periodic potential formed by the Coulomb interaction with the crystal. Many milestones were achieved in this field: from the realization of a BEC [43, 44] and a degenerate Fermi gas [45] to phenomena like the superfluid to Mott-insulator transition [46], the BEC-BCS crossover [47, 48], the observation of topological matter [49, 50], and the observation of anti-ferromagnetic correlations in the doped Fermi-Hubbard model [51], to name only a few. Still there are many outstanding questions like the observation of the fractional quantum Hall effect, or superfluidity in the doped Fermi-Hubbard model.

2.2. The route to BEC

The starting point for most of our experiments is a BEC in a magnetic trap. The preparation of a BEC has evolved from a Nobel price winning achievement to a demanding, but standard experimental sequence. The steps we use for condensation are explained in this section.
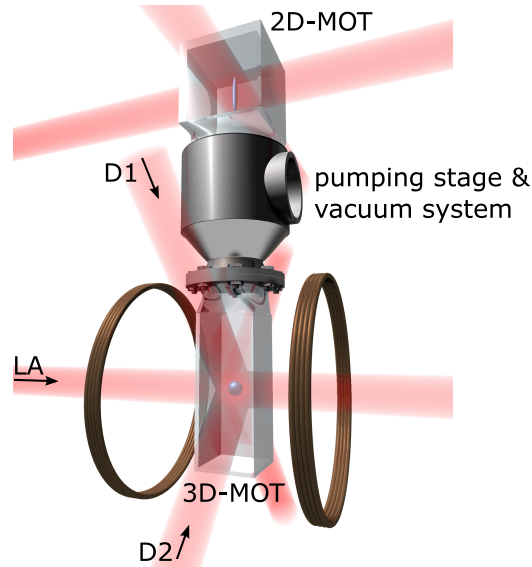
Figure 2.1.: Setup of the 2D and 3D MOT. The atoms are first precooled in a 2D MOT which is shown at the top. Subsequently they get transferred into the 3D MOT at the bottom by a push beam (not shown). The two glass cells are separated by a differential pumping stage. The 3D MOT consists of three pairs of beams labeled D1, D2 and LA and a pair of anti-Helmholtz coils. Adapted from [52].

2.2.1. 2D and 3D MOT, optical molasses

A magneto-optical trap (MOT) [53] is a trap capable of capturing and cooling of room temperature atoms via photon absorption. Its working principle is based on counter-propagating circularly polarized laser beams, red detuned with respect to a suitable atomic transition, which slow the atoms as a consequence of velocity dependent absorption due to the Doppler-effect and which confine the atoms as a consequence of position dependent absorption due to the Zeeman effect in the magnetic field of anti-Helmholtz coils. Our setup consists of the combination of a two-dimensional (2D) and a three-dimensional (3D) MOT, see Fig. 2.1 for a 3D rendering and appendix A for the optical setup. This design allows for fast loading of the 3D MOT and at the same time for optimal vacuum conditions in the 3D MOT. The atoms—in our case ^{87}Rb—are supplied from a dispenser that is electrically heated. In the 2D MOT the atoms get confined and cooled in two directions creating an elongated cloud of atoms. A push laser beam propagates along the long axis of this cloud and accelerates atoms towards the lower glass cell. The best loading rate is achieved for blue detuning, i.e., when accelerating the atoms that have the correct propagation direction already. In this way a beam of pre-cooled atoms is formed. This beam propagates through a differential pumping stage between the 2D and 3D MOT glass cells. In the 3D MOT laser beams from all six directions form a cloud of atoms. In our setup we have one horizontal pair of beams and two pairs under 45° with respect

to gravity and perpendicular to the horizontal pair. The temperature in the MOT is limited by the recoil temperature $T_{\mathrm{R}} = h^2/(m\lambda^2) = 360\,\mathrm{nK}$ and the Doppler temperature $T_{\mathrm{D}} = \hbar\Gamma/(2k_{\mathrm{B}}) = 150\,\mu\mathrm{K}$. Here we used the mass $m = 87\,\mathrm{u}$ of $^{87}\mathrm{Rb}$, the wavelength $\lambda = 780\,\mathrm{nm}$ of the D_2 ($5^2\mathrm{S}_{1/2} \rightarrow 5^2\mathrm{P}_{3/2}$) transition and the decay rate $\Gamma = 2\pi \times 6.07\,\mathrm{MHz}$ [54]. h is the Planck constant, $\hbar = h/(2\pi)$ is the reduced Planck constant, and k_{B} is the Boltzmann constant.

The Doppler limit can be overcome in the next step, the bright molasses. It is initialized by switching off the magnetic fields using insulated-gate bipolar transistors (IGBTs) which are protected against voltage spikes by varistors connected in parallel. As a result of switching off the magnetic fields the Zeeman splitting vanishes. Still the m_F sublevels are not degenerate because they experience different AC Stark shifts depending on the local polarization of the light. Given that the counter-propagating, circularly polarized beams create a standing polarization wave, the atoms see a periodic potential landscape. The atoms move in this potential and due to the detuning for excitation being minimal at maximal potential energy the atoms get excited most likely in this situation. The spontaneous decay from the excited state however is not energy selective and the atoms therefore experience a net loss of energy corresponding to a cooling.

2.2.2. Magnetic trap and evaporative cooling

In order to cross the phase transition to a BEC the phase space density still must be increased substantially. This is achieved by evaporation, i.e. the removal of the hottest atoms from the cloud. It turns out that the cooling effect can overcompensate the loss of particles resulting in an increase of phase space density by this technique. First, the atoms need to be transferred into a magnetic trap (MT) because photon scattering as in MOTs will represent a source of heating. Therefore the molasses beams are quickly switched off by the combination of a Pockels cell and a polarizing beam splitter.

A magnetic trap exploits the fact that states with a magnetic moment which is parallel to a magnetic field will energetically favour regions of low magnetic field. In contrast to a local maximum, a local minimum of a static magnetic field is realizable and constitutes a trap for these low-field seeking states. In order to obtain good transfer efficiency between the optical molasses and the MT an optical pumping puls is needed to transfer the atoms to the low-field seeking state $|F = 2, m_{\mathrm{F}} = 2\rangle$. Our magnetic trap is a hybrid between cloverleaf and 4D trap (Fig. 2.2), inducing a harmonic potential for the low-field seekers and avoiding a zero of the magnetic field which would induce spin-flips to untrapped states [39–41]. The design allows for an isotropic trap during loading from the molasses which can then be compressed into a cigar shaped trap for higher densities for the evaporation by ramping down the
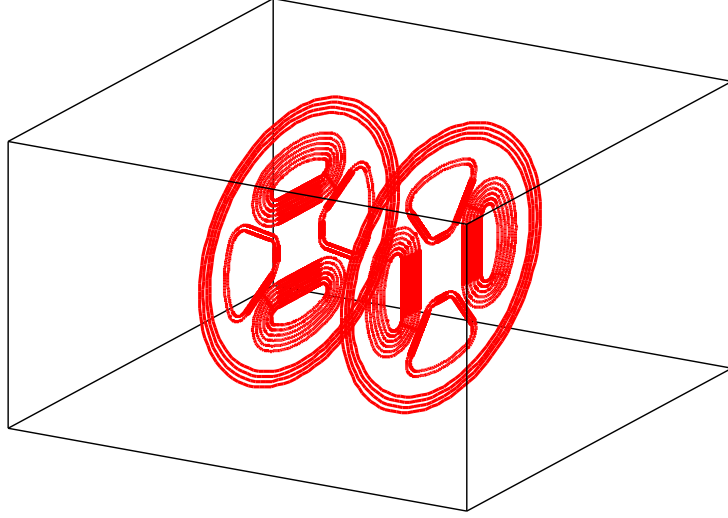
Figure 2.2.: Coil setup of the magnetic trap. It consists of a pair of Helmholtz coils and a pair of coils winding similar to a cloverleaf but with half of the leaves having significantly less windings. Taken from [39].

Helmholtz field. The resulting magnetic field can be written as [39]

$$\boldsymbol{B} = B_0 \begin{pmatrix} 0 \\ 0 \\ 1 \end{pmatrix} + B' \begin{pmatrix} x \\ -y \\ 0 \end{pmatrix} + \frac{B''}{2} \begin{pmatrix} -xz \\ -yz \\ z^2 - 1/2(x^2 + y^2) \end{pmatrix}, \qquad (2.1)$$

with bias field B_0, radial gradient B' and axial curvature B''. The magnitude of the magnetic field, which is proportional to the trapping potential, can be expanded to be

$$B(\rho, z) = B_0 + \frac{1}{2}\rho^2 \left(\frac{B'^2}{B_0} - \frac{B''}{2} \right) + \frac{1}{2}z^2 B'', \qquad (2.2)$$

revealing the harmonic nature of the trap. The trap was characterized in detail [39, 40] before mounting. Yet, in practice, the trapping frequency in plane is determined by analysis of dipole oscillations in the trap and the calibration is only used for the computation of the trapping frequency in z-direction (appendix B).

The evaporation is realized by a RF-knife: A radio frequency (RF) field is applied with a frequency chosen such that at the outer regions of the cloud spin flips are driven. As soon as an atom gets transferred to a state that is not trapped it is lost from the cloud. Due to collisions the cloud rethermalizes to a lower temperature in response to the loss of particles of high energy. The frequency of the RF-knife is slowly lowered, moving the resonance surface closer to the trap center. This must be done fast enough compared to the vacuum limited lifetime of the cold atoms and slow enough for the system to be in thermal equilibrium at every point in time. The onset of condensation is detected via the appearance of a bimodal momentum distribution

corresponding to the coexistence of condensate and thermal cloud. In our setup we start the evaporation ramp at a RF frequency of $\sim 20\,\mathrm{MHz}$ and lower it to a final frequency of $\sim 90\,\mathrm{kHz}$ within $\sim 20\,\mathrm{s}$.

2.3. The optical lattice

For the quantum simulation of periodic potentials an optical lattice can be used. Optical lattices leverage the AC Stark effect [55]: Atoms in a light field experience a negative(positive) energy shift if the frequency of the light is red(blue) detuned from the atomic resonance. Therefore the antinodes(nodes) of the light field constitute potential minima for the atoms. In order to suppress heating via lattice light scattering, the detuning must be chosen large. Due to the fact that the potential depth decreases slower with increasing detuning as the scattering rate, a significant optical lattice potential with low light scattering can be achieved, yet usually requiring powers of the order of Watt. In our experiment a triangular lattice and a boron-nitride lattice—i.e., a honeycomb lattice with unequal on-site energies in the unit cell—are possible as will be explained below.

The loading into the lattice is achieved by an exponential ramp up of the lattice beam intensities in a time of several hundreds of milliseconds.

2.3.1. Polarization approach

One possible way of implementing a lattice that can be tuned between triangular and boron-nitride is the intersection of three beams under 120° with tunable polarization. This approach is discussed in detail in [56]. If the polarization of the beams is in the lattice plane (p-polarization), the maxima of the resulting intensity patterns are arranged as a honeycomb lattice, whereas in the case of the polarization being perpendicular to the lattice plane (s-polarization), a triangular lattice is formed. The idea is now to choose a polarization that has both s- and p-component to create more complex lattices. In particular if one chooses the same ratio of s- and p-polarization in all beams this results in a potential which consists of the sum of a triangular and a honeycomb lattice. The relative position of the two addends can be chosen by the phase between s- and p-polarization, i.e., by the ellipticity.

In the following we want to formalize this approach. Using the conventions introduced in [56] we describe the electric fields $\mathbf{E}_i(\boldsymbol{r}, t)$ ($i = 1, 2, 3$) of the three lattice beams as

$$\boldsymbol{E}_i(\boldsymbol{r}, t) = E_{0,i}\hat{\boldsymbol{e}}_i \exp\left[i\left(\boldsymbol{k}_i\boldsymbol{r} - \omega t - \phi_i\right)\right], \tag{2.3}$$

where $E_{0,i}$ is proportional to the square root of the laser intensity, ω is the laser frequency, and the ϕ_i denote the phases of the laser beams. The wave vectors $\boldsymbol{k}_i$ are
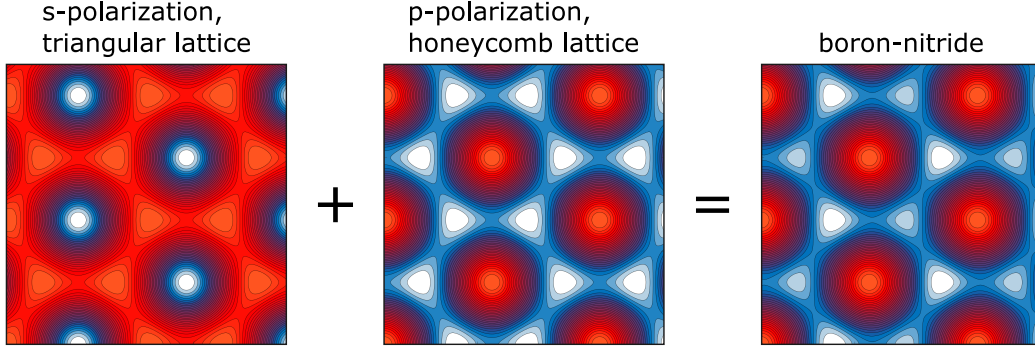
Figure 2.3.: Polarization approach. A boron-nitride lattice (right) can be obtained by adding the triangular lattice formed by the s-polarization (left) and the honeycomb lattice formed by the p-polarization (middle) when choosing the relative position such that the potential minima of the triangular lattice are at the same position as the minima of one sublattice of the honeycomb lattice. Here we used $\theta_1 = \theta_2 = \theta_3 = 9°$ and $\alpha_1 = 0°$, $\alpha_2 = 120°$, $\alpha_3 = 360°$. Note that the colorscale for every image is rescaled to the respective maximal values.

given by

$$\boldsymbol{k}_1 = k_{\mathrm{L}} \begin{pmatrix} 0 \\ 1 \\ 0 \end{pmatrix}, \quad \boldsymbol{k}_2 = k_{\mathrm{L}} \begin{pmatrix} -\sqrt{3}/2 \\ -1/2 \\ 0 \end{pmatrix}, \quad \boldsymbol{k}_3 = k_{\mathrm{L}} \begin{pmatrix} \sqrt{3}/2 \\ -1/2 \\ 0 \end{pmatrix}, \tag{2.4}$$

with $k_{\mathrm{L}} = 2\pi/\lambda$ being the magnitude of the wave vector of the laser given by its wavelength λ. The polarization $\hat{\boldsymbol{e}}_i = \cos\theta_i \hat{\boldsymbol{e}}_{\mathrm{p},i} + \exp(i\alpha_i)\sin\theta_i \hat{\boldsymbol{e}}_{\mathrm{s},i}$ is decomposed into s- and p-polarization with mixing angle θ and relative phase α. The polarization vectors are given by

$$\hat{\boldsymbol{e}}_{\mathrm{s},1} = \hat{\boldsymbol{e}}_{\mathrm{s},2} = \hat{\boldsymbol{e}}_{\mathrm{s},3} = \begin{pmatrix} 0 \\ 0 \\ 1 \end{pmatrix}, \quad \hat{\boldsymbol{e}}_{\mathrm{p},1} = \begin{pmatrix} -1 \\ 0 \\ 0 \end{pmatrix}, \quad \hat{\boldsymbol{e}}_{\mathrm{p},2} = \begin{pmatrix} 1/2 \\ -\sqrt{3}/2 \\ 0 \end{pmatrix}, \quad \hat{\boldsymbol{e}}_{\mathrm{p},3} = \begin{pmatrix} 1/2 \\ \sqrt{3}/2 \\ 0 \end{pmatrix}. \tag{2.5}$$

The potential energy landscape $V(\boldsymbol{r})$ is proportional to the intensity averaged over one period of the laser frequency [55] which in turn is proportional to the absolute value squared of the total electric field. Hence we can write

$$V(\boldsymbol{r}) \propto |\boldsymbol{E}_1 + \boldsymbol{E}_2 + \boldsymbol{E}_3|^2 = \mathrm{const} + 2\mathrm{Re}\left(\bar{\boldsymbol{E}}_1 \boldsymbol{E}_2\right) + 2\mathrm{Re}\left(\bar{\boldsymbol{E}}_1 \boldsymbol{E}_3\right) + 2\mathrm{Re}\left(\bar{\boldsymbol{E}}_2 \boldsymbol{E}_3\right). \tag{2.6}$$

We can see that the lattice can be thought of as a sum of three 1D lattices. Omitting the constant, we therefore define $V(\boldsymbol{r}) = \sum_{i<j} V_{ij}(\boldsymbol{r})$ with [56]

$$
\begin{aligned}
V_{ij}(\boldsymbol{r}) = &\sqrt{V_i V_j} \cos\theta_i \cos\theta_j \cos\left[(\boldsymbol{k}_i - \boldsymbol{k}_j)\boldsymbol{r} + \phi_j - \phi_i\right] \\
&- 2\sqrt{V_i V_j} \sin\theta_i \sin\theta_j \cos\left[(\boldsymbol{k}_i - \boldsymbol{k}_j)\boldsymbol{r} + \phi_j - \phi_i - \alpha_j + \alpha_i\right],
\end{aligned} \tag{2.7}
$$

where V_i is proportional to the intensity of beam i (see appendix B for their calibration via Kapitza-Dirac scattering). Hence the lattice is indeed the sum of a potential coming from the p-polarization ($\cos\theta$-terms) and a potential coming from the s-polarization ($\sin\theta$-terms). Due to the different sign the p-polarization forms a honeycomb lattice and the s-polarization a triangular lattice. The phases of the laser beams determine the origin of the lattice whereas the phases of the polarizations shift the two lattices with respect to each other. For the choice $\alpha_{1(2,3)} = 0°(120°, 240°)$ the relative position is such that the resulting lattice is a boron-nitride lattice (Fig. 2.3). More possible lattice geometries are presented in [56].

2.3.2. Multi-frequency approach

The polarization approach allows for a flexible lattice geometry, yet the polarization of the lattice beams cannot be controlled on arbitrary time scales and thus, e.g., a quench of the lattice geometry cannot be realized. Furthermore, with this approach the local polarization on the sublattices of the honeycomb lattice are different and therefore the potential depth can be dependent on the m_F-state due to the vector light shift. These problems do not occur when using what we want to call the multi-frequency approach. The idea is to be able to independently control the origin of three linearly polarized 1D lattices, which will be possible if they do not interfere do to a detuning, as discussed below.
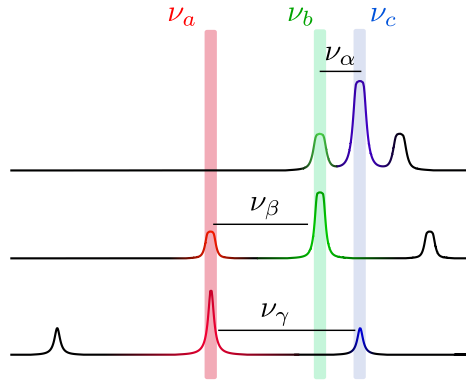
Figure 2.4.: Frequency setup for the multi-frequency lattice. The three schematic spectra correspond to the three lattice beams. The coloured bands denote the carriers with frequencies ν_a, ν_b and ν_c which originate from the same laser but which are shifted by the use of AOMs. Each beam passes through an EOM as well, resulting in sidebands at frequency difference ν_α, ν_β and ν_γ. The frequencies are chosen such that each carrier is resonant with exactly one side band, i.e., $\nu_\alpha = \nu_c - \nu_b$, $\nu_\beta = \nu_b - \nu_a$ and $\nu_\gamma = \nu_c - \nu_a$. The exact choice of frequencies is $\nu_a = \nu_0 + 105.005\,\text{MHz}$, $\nu_b = \nu_0 + 112.775\,\text{MHz}$, $\nu_c = \nu_0 + 114.995\,\text{MHz}$, $\nu_\alpha = 2.22\,\text{MHz}$, $\nu_\beta = 7.77\,\text{MHz}$ and $\nu_\gamma = 9.99\,\text{MHz}$, where ν_0 is the frequency of the lattice laser. Adapted from [57].

The technical implementation is realized by the use of three electro-optical modulators (EOMs) and three acousto-optical modulators (AOMs), one of each for every lattice beam. The lattice beams are detuned via the AOMs in such a way that they have the same frequency as exactly one sideband from one other lattice beam leading to only pairwise interference. Fig. 2.4 shows our choices of frequencies which satisfy this condition. Shifting the phase of the RF applied to an EOM results in the desired displacement of the 1D lattice which is created by the corresponding sideband.

In the following we want to illustrate how this technique leads to the desired lattice geometries (Fig. 2.5). The most intuitive configuration is the case where the origins of the three 1D lattices are chosen such that there are points where the potential valleys of all of them coincide (Fig. 2.5a). Consequently, these are the points of minimal potential energy and—as can be seen from the figure—they form a triangular lattice. The second important lattice geometry, the boron-nitride, is not so straightforward. If, starting from the triangular configuration, one 1D lattice is shifted by half a 1D lattice constant, then the 1D lattice valleys form small triangles which have minimal potential energy in their center (Fig. 2.5b). These triangles are arranged in a honeycomb pattern. When going away from the honeycomb configuration by moving again one 1D lattice, then one sublattice gets deeper and the other becomes more shallow resulting in a boron-nitride lattice (2.5c). Moving the 1D lattice even further, no bound state exist any more on the shallow sublattice and we again have a triangular lattice.

The lattice potential can be written as

$$V(\boldsymbol{r}) = \sum_{i<j} V_{ij}(\boldsymbol{r}) = 2 \sum_{i<j} V_{ij,0} \cos\left[(\boldsymbol{k}_i - \boldsymbol{k}_j)\,\boldsymbol{r} + s_{ij}\varphi_{\mathrm{g}}/3\right], \tag{2.8}$$

where we defined the 1D lattice depths $V_{ij,0}$ and the geometry phase φ_{g} and $s_{12} = s_{23} = 1 = -s_{13}$. Global phases are absorbed into the choice of origin. The definitions
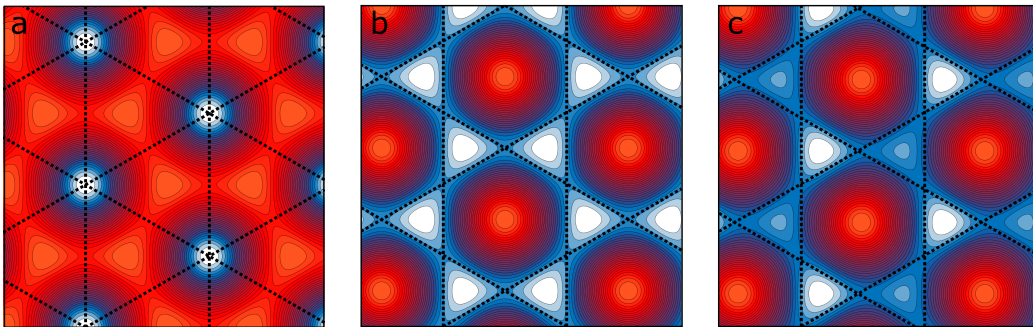
Figure 2.5.: Triangular, honeycomb and boron-nitride lattice using the multi-frequency approach. Shown is the potential landscape of a **(a)** triangular lattice, **(b)** honeycomb lattice and **(c)** boron-nitride lattice. To illustrate how this lattices arise from the summation of three 1D lattices the potential minima of these 1D lattices are shown as black dotted lines.

of the geometry phase φ_g and the signs s_{ij} are such that the sublattices are stationary when changing the geometry phase. This convention is different from the one used for the explanations above, where just one lattice was moving.

For more details on the method we refer the reader to the thesis of Luca Asteria [57].

2.4. Absorption imaging

Our observables in the experiment are atomic column densities that we deduce using absorption imaging. The basic idea of absorption imaging is to compute the column density of the atoms along the line of sight by measuring the attenuation of an imaging laser. To this end an absorption image with the attenuated beam is compared to a reference image with no attenuation, i.e. with no atoms present.

For imaging we use circularly polarized resonant light that drives the $|F = 2, m_F = 2\rangle \leftrightarrow |F' = 3, m'_F = 3\rangle$ transition of the D$_2$ line. For small imaging light intensities the transmission through the atomic cloud can be described by the Beer-Lambert law [58]

$$T(x,y) = e^{-\sigma_0 n(x,y)}, \tag{2.9}$$

with the column density $n(x,y) = \int \mathrm{d}z\, n(\boldsymbol{r})$ and the resonant scattering cross section $\sigma_0 = 3\lambda^2/(2\pi)$. Hence, if we assume the CCD camera counts to be linear in intensity, we can obtain the column density as

$$n(x,y) = \frac{1}{\sigma_0} \ln \frac{1}{T(x,y)} = \frac{1}{\sigma_0} \ln \frac{N_\mathrm{ref}(x,y)}{N_\mathrm{abs}(x,y)} \tag{2.10}$$

from the number of counts $N_\mathrm{abs}(x,y)(N_\mathrm{ref}(x,y))$ on the absorption(reference) image. To obtain a better precision we add correction terms taking into account saturation effects due to finite intensity. The expression used in data analysis is [59]

$$n(x,y) = \frac{1}{\sigma_0} \left[\ln \frac{N_\mathrm{ref}(x,y)}{N_\mathrm{abs}(x,y)} + \frac{(N_\mathrm{ref} - N_\mathrm{abs})C}{I_\mathrm{sat}} \right], \tag{2.11}$$

where we introduced the saturation intensity $I_\mathrm{sat} = 16.69\,\mathrm{W/m^2}$ for our imaging transition [54] and the conversion factor $C = 5.68 \times 10^{-4}\,\mathrm{W/m^2}$ from counts on the camera to intensity (see appendix C for its computation). We save the atom number on each pixel, making it necessary to add a factor of A_pixel/M^2 with magnification $M = 2.02$ (appendix C) and pixel size of the camera $A_\mathrm{pixel} = (13\,\mathrm{\mu m})^2$.

Theoretically, in absorption imaging the beam profile is not relevant since it is the same on the absorption and reference image. In practice there are small fluctuations of the pointing between absorption and reference image even though there is only a small wait time of $34\,\mathrm{ms}$ between the two. As a consequence artefacts in the form of fringes arise in the deduced atomic density. For all the images in this thesis we applied a defringing algorithm which constructs an optimized reference image from a set of reference images such that it minimizes the fringes. See appendix D for details on the algorithm.

3. The quantum gas magnifier

Experimentally driven understanding of nature is always limited by the capability to measure certain observables. Historically, in cold atoms, a meaningful and easily accessible observable is the momentum distribution of the particles under investigation. In particular coherent samples in periodic potentials feature interesting momentum distributions. Yet, there are interesting phenomena that are not visible in the momentum distribution, e.g., Mott-insulator shells of a trapped gas [30, 31]. Single site resolved imaging in real space is nowadays accessible by the use of quantum gas microscopes leading to the observation of a vast number of phenomena [32]. However, these machines also have limitations, such as depth of focus, parity projection, and diffraction limited resolution. There are other techniques which overcome some of these limitations but at the cost of other. For example using an electron microscope [33] solves the mentioned problems but at the cost of reduced detection efficiency which prohibits the measurement of correlations.

So far, progress in real space measurement has been made by maximizing the spatial resolution of the measurement apparatus. Here we present a complementary approach which is the magnification of the sample itself, enlarging length scales to a degree where they can be easily measured using standard imaging. This allows for single shot measurement of the column density of 3D systems with sub-lattice site resolution.

We call this approach quantum gas magnification and introduce it in this chapter. First the working principle will be explained. Then, benchmark experiments will be presented: a characterization of the thermal phase transition from normal gas to superfluid, a measurement of thermalization using RF addressing and a quench dynamics experiment with sub-lattice site resolution. Eventually we present results on the investigation of on-site fluctuations showing that these are preserved in the magnification protocol.

The experiments presented here have been carried out together with my fellow PhD students Luca Asteria and Marcel Kosch and under the supervision of Klaus Sengstock and Christof Weitenberg.

3.1. Working principle

Let us start with a description of the working principle. The quantum gas magnifier protocol consists of a quarter period evolution in a harmonic trap followed by a free expansion time. There are many ways to illustrate how this protocol leads to a
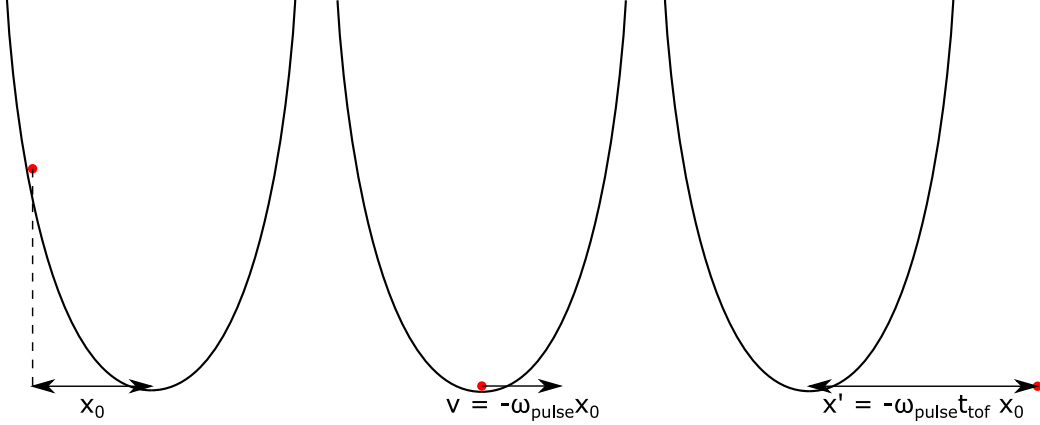
Figure 3.1.: Classical picture of the quantum gas magnifier. A harmonic potential is suddenly switched on while a particle is at rest at a distance x_0 from the trap center (left). After a quarter period evolution the particle reaches the trap center with a velocity $v = -\omega_{\text{pulse}}x_0$ (middle). At this point the harmonic trap is switched off again resulting in a free propagation to position $x' = -\omega_{\text{pulse}}t_{\text{tof}}x_0$ after a time t_{tof} corresponding to a magnification of $x'/x_0 = -\omega_{\text{pulse}}t_{\text{tof}}$.

magnification of the original density distribution. Probably the most intuitive picture is obtained by considering non-interacting classical mass points in 1D (Fig. 3.1). Let us suppose that a particle is at rest at a certain position x_0. Abruptly a harmonic potential centered at the origin is turned on. Consequently the particle is starting to move and after a quarter period it reaches the trap center, having gained a velocity $v = -\omega_{\text{pulse}}x_0$ with ω_{pulse} being the trap frequency of the harmonic trap. At this point in time the harmonic potential is switched off resulting in a free propagation of the particle. After a time t_{tof} of free propagation the particle's position is given by $x' = vt_{\text{tof}} = -\omega_{\text{pulse}}t_{\text{tof}}x_0$. Hence the position of the particle is magnified by a factor $-\omega_{\text{pulse}}t_{\text{tof}}$. Consequently, a density distribution $\rho(x)$ would be magnified to $\rho'(x) = \rho(-x/(\omega t_{\text{tof}}))$ with x being measured with respect to the trap center. The minus sign leads to an inversion of the distribution with respect to the origin.

In a general setting, the particles will not be at rest at the start of the protocol. An initial velocity v_0 maps to a displacement after the quarter period evolution as can be seen, e.g., from the representation of the harmonic oscillator in phase space where a quarter period evolution corresponds to a quarter rotation on the corresponding ellipse [60]. This displacement $\delta x = v_0/\omega_{\text{pulse}}$ can be either made negligible by choosing the expansion time such that $\omega_{\text{pulse}}t_{\text{tof}}x_0 \gg v_0/\omega_{\text{pulse}}$ or can be eliminated by slightly elongating the hold time in the harmonic potential. Explaining the latter possibility is more involved, but it will turn out to be also possible in the quantum case. Hence we want to derive this correction to the evolution time in the harmonic potential here.

For the description we choose Hamlitonian mechanics since in that way the generalization to quantum mechanics will be particularly easy as will be seen later. The

Hamiltonian function of the harmonic oscillator is given by

$$H_{\mathrm{ho}} = \frac{1}{2m}p^2 + \frac{1}{2}m\omega_{\mathrm{pulse}}^2 x^2, \tag{3.1}$$

resulting in the equations of motion

$$\frac{\mathrm{d}}{\mathrm{d}t}x = \frac{1}{m}p \tag{3.2}$$

$$\frac{\mathrm{d}}{\mathrm{d}t}p = -m\omega_{\mathrm{pulse}}^2 x. \tag{3.3}$$

These equations are solved by

$$x(t) = x(0)\cos(\omega_{\mathrm{pulse}}t) + \frac{p(0)}{m\omega_{\mathrm{pulse}}}\sin(\omega_{\mathrm{pulse}}t), \tag{3.4}$$

$$p(t) = p(0)\cos(\omega_{\mathrm{pulse}}t) - m\omega_{\mathrm{pulse}}x(0)\sin(\omega_{\mathrm{pulse}}t). \tag{3.5}$$

After the evolution time t_{ho} in the harmonic potential, the free expansion follows for a time t_{tof} resulting in a final state of

$$x(t_{\mathrm{ho}}, t_{\mathrm{tof}}) = x(0)\cos(\omega_{\mathrm{pulse}}t_{\mathrm{ho}}) + \frac{p(0)}{m\omega_{\mathrm{pulse}}}\sin(\omega_{\mathrm{pulse}}t_{\mathrm{ho}}) + \frac{p(t_{\mathrm{ho}}, t_{\mathrm{tof}}=0)}{m}t_{\mathrm{tof}}, \tag{3.6}$$

$$p(t_{\mathrm{ho}}, t_{\mathrm{tof}}) = p(0)\cos(\omega_{\mathrm{pulse}}t_{\mathrm{ho}}) - m\omega_{\mathrm{pulse}}x(0)\sin(\omega_{\mathrm{pulse}}t_{\mathrm{ho}}). \tag{3.7}$$

Plugging (3.7) into (3.6) leads to

$$\begin{aligned} x(t_{\mathrm{ho}}, t_{\mathrm{tof}}) =\,& x(0)\left[\cos(\omega_{\mathrm{pulse}}t_{\mathrm{ho}}) - \omega_{\mathrm{pulse}}t_{\mathrm{tof}}\sin(\omega_{\mathrm{pulse}}t_{\mathrm{ho}})\right] \\ &+ p(0)\left[\frac{1}{m\omega_{\mathrm{pulse}}}\sin(\omega_{\mathrm{pulse}}t_{\mathrm{ho}}) + \frac{t_{\mathrm{tof}}}{m}\cos(\omega_{\mathrm{pulse}}t_{\mathrm{ho}})\right]. \end{aligned} \tag{3.8}$$

The ideal condition for density magnification is reached when the final position $x(t_{\mathrm{ho}}, t_{\mathrm{tof}})$ does not depend on the initial momentum $p(0)$. This is the case when the coefficient of the initial momentum vanishes which is achieved when the condition

$$\tan\omega_{\mathrm{pulse}}t_{\mathrm{ho}} = -\omega_{\mathrm{pulse}}t_{\mathrm{tof}} \tag{3.9}$$

is met. In this case (3.8) simplifies to

$$x(t_{\mathrm{ho}}, t_{\mathrm{tof}}) = x(0)\sqrt{1 + (\omega_{\mathrm{pulse}}t_{\mathrm{tof}})^2}. \tag{3.10}$$

The magnification derived for this optimized evolution time in the harmonic trap approaches the value found earlier for $\omega_{\mathrm{pulse}}t_{\mathrm{tof}} \gg 1$ which is the case for significant magnification. In Fig. 3.2 this focusing condition is visualized by showing a set of trajectories in phase space all having the same initial position but different initial
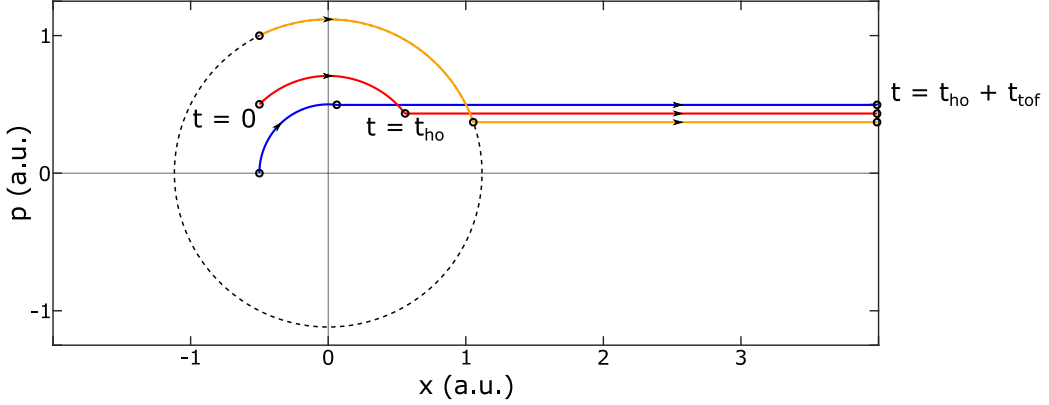
Figure 3.2.: Focusing classical particles. Trajectories of classical particles in phase space for an evolution in a harmonic trap followed by a free expansion with the evolution time in the harmonic trap being chosen as a function of the free expansion time such that the focusing condition (3.9) is met. The circles highlight the initial state at $t = 0$, the state when the harmonic trap is switched off at $t = t_{\mathrm{ho}}$ and the final state at $t = t_{\mathrm{ho}} + t_{\mathrm{tof}}$. It can be seen that indeed all three trajectories terminate at the same x-position despite largely different initial momenta.

momenta. Due to the optimal choice of the evolution time in the harmonic trap all trajectories reach the same position after the expansion time.

Now where we demonstrated the density magnification for classical particles we want to proceed with the consideration of quantum particles. Here we want to adopt the Heisenberg picture because it is basically identical to the Hamiltonian mechanics approach as we will see below. The Hamiltonian of the harmonic oscillator is given by

$$\hat{H}_{\mathrm{ho}} = \frac{1}{2m}\hat{p}^2 + \frac{1}{2}m\omega_{\mathrm{pulse}}^2\hat{x}^2. \tag{3.11}$$

resulting in the equations of motion

$$\frac{\mathrm{d}}{\mathrm{d}t}\hat{x} = \frac{i}{\hbar}\left[\hat{H}, \hat{x}\right] = \frac{1}{m}\hat{p} \tag{3.12}$$

$$\frac{\mathrm{d}}{\mathrm{d}t}\hat{p} = \frac{i}{\hbar}\left[\hat{H}, \hat{p}\right] = -m\omega_{\mathrm{pulse}}^2\hat{x}, \tag{3.13}$$

It can be seen that these are actually the same equations as those for the classical variables (3.2-3.3) and therefore the solution has the same form except for the variables being promoted to operators. Since at no point in the derivation for the classical focusing condition we made use of the fact that we are dealing with classical variables all results are still valid in the quantum case. Only for the visualization of the focusing condition we need to take a slightly different perspective. Since position and momentum are not a number any more we cannot make a plot showing the trajectory $(\hat{x}(t), \hat{p}(t))$. Instead what we can do is to decompose the position operator
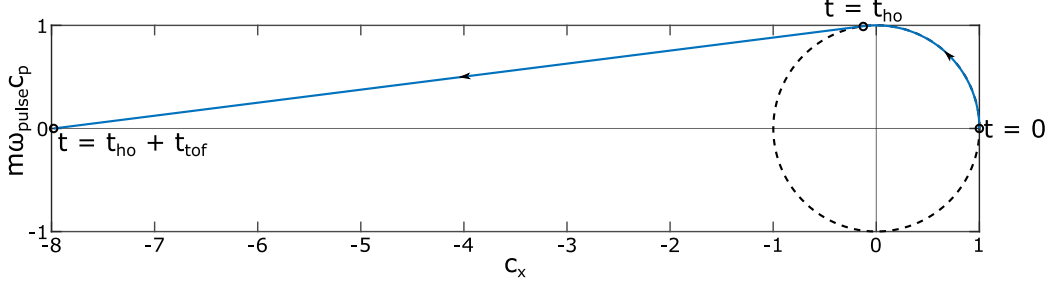
Figure 3.3.: Focusing quantum particles. The plot shows the evolution of the decomposition of the position operator into initial position and momentum operators $\hat{x} = c_x(t)\hat{x}(0) + c_p(t)\hat{p}(0)$ as a function of time. The circles highlight the initial operator at $t = 0$, the operator when the harmonic trap is switched off at $t = t_{\text{ho}}$ and the final operator at $t = t_{\text{ho}} + t_{\text{tof}}$. It can be seen that the position operator returns to a multiple of itself, in particular, with no contribution from the momentum operator demonstrating independence of the final density from the initial momentum distribution.

as $\hat{x}(t) = c_x(t)\hat{x}(0) + c_p(t)\hat{p}(0)$ and plot the trajectory $(c_x(t), c_p(t))$. We can read off these coefficients for the evolution in the harmonic trap, i.e. for $t \leq t_{\text{ho}}$, from (3.4) to be

$$c_x(t) = \cos(\omega_{\text{pulse}}t), \tag{3.14}$$

$$c_p(t) = \frac{1}{m\omega_{\text{pulse}}} \sin(\omega_{\text{pulse}}t), \tag{3.15}$$

and for the free expansion including focusing condition we replace t_{tof} by t in (3.6) and plug in the focusing condition (3.9) to obtain

$$c_x(t) = -\frac{1 + \omega_{\text{pulse}}^2 t t_{\text{tof}}}{\sqrt{1 + (\omega_{\text{pulse}}t_{\text{tof}})^2}}, \tag{3.16}$$

$$c_p(t) = -\frac{1}{m} \frac{t - t_{\text{tof}}}{\sqrt{1 + (\omega_{\text{pulse}}t_{\text{tof}})^2}}, \tag{3.17}$$

for $t > t_{\text{ho}}$ and choosing $\pi/2 < \omega_{\text{pulse}}t_{\text{ho}} < \pi$ for the inversion of the focusing condition. The corresponding trajectory is plotted in Fig. 3.3. When looking for the comparison to the classical case, several trajectories would be possible if visualizing the expectation values $\langle \hat{x}(t) \rangle$, $\langle \hat{p}(t) \rangle$ for different states, which would then look like the classical trajectories with initial state $x = \langle \hat{x}(0) \rangle$ and $p = \langle \hat{p}(0) \rangle$. However since the position and momentum are in general not sharp the consideration of the position operator is the only way to conveniently visualize the complete information. In Fig. 3.3 the focusing for the quantum case is expressed by the fact that the admixture of the momentum operator to the position operator c_p vanishes at the end of the magnification protocol.

All these considerations apply for a non-interacting system. The quantum gas magnifier can also be used for interacting systems by switching off the interactions for the duration of the matter wave dynamics. This can be achieved in several ways. For our experiments we remove the effects of interactions during magnification by two measures. First, we start the evolution in the harmonic trap by switching off the lattice which leads to a quick reduction of the density. Coherent systems however will form sharp interference patterns increasing the density again. Therefore we remove the coherence while preserving the on-site populations by a hold time in a deep lattice. However, even though the on-site populations are unaffected by this, the density is disturbed and therefore, if we want to obtain the full density information, we can only image incoherent systems. Alternatively a stronger transverse confinement could be used resulting in a fast transverse expansion when it is switched off. If working with a dipole trap and atoms with a Feshbach resonance, the best solution would be to switch off the interactions during the matter wave magnification using a magnetic field corresponding to vanishing interactions.

More details can be found in the thesis of my colleague Luca Asteria [57] or reference [22].

3.2. Resolution of the quantum gas magnifier

In a first set of experiments we characterize the resolution of the quantum gas magnifier for different magnifications. To this end we load a BEC into a deep triangular lattice (chapter 2), eliminating the need to suppress coherence later and we can thus record the full density information. Using different trapping frequencies allows the investigation of different magnifications. From the images that we obtain we extract cuts that can be fitted by a grid of Gaussians to obtain a $1/\sqrt{e}$ width σ_{site} of the sites (Fig. 3.4). The resulting widths are plotted as a function of magnification for different particle numbers in Fig. 3.4g. The observed width can be fitted by a model assuming a magnified size of the wave function σ_{wf} convoluted with an optical resolution of the absorption imaging σ_{opt}, i.e.,

$$\sigma_{\text{site}}(M) = \sqrt{\sigma_{\text{opt}}^2 + (M\sigma_{\text{wf}})^2}. \tag{3.18}$$

A fit to all datapoints irrespective of atom number (brown solid line in Fig. 3.4b) yields $\sigma_{\text{opt}} = 5.2(2)\,\mu\text{m}$ and $\sigma_{\text{wf}} = 118(3)\,\text{nm}$. According to the Rayleigh criterion single lattice sites can be resolved if $a_{\text{lat}} > 0.35\sigma_{\text{site}}$, where 0.35 is the width of a Gaussian fitted to an airy disk of unit resolution. The criterion is depicted as the blue solid line in Fig. 3.4g. Hence, according to the fit already a magnification of ~ 23 is enough to obtain single site resolution which is easily achieved.
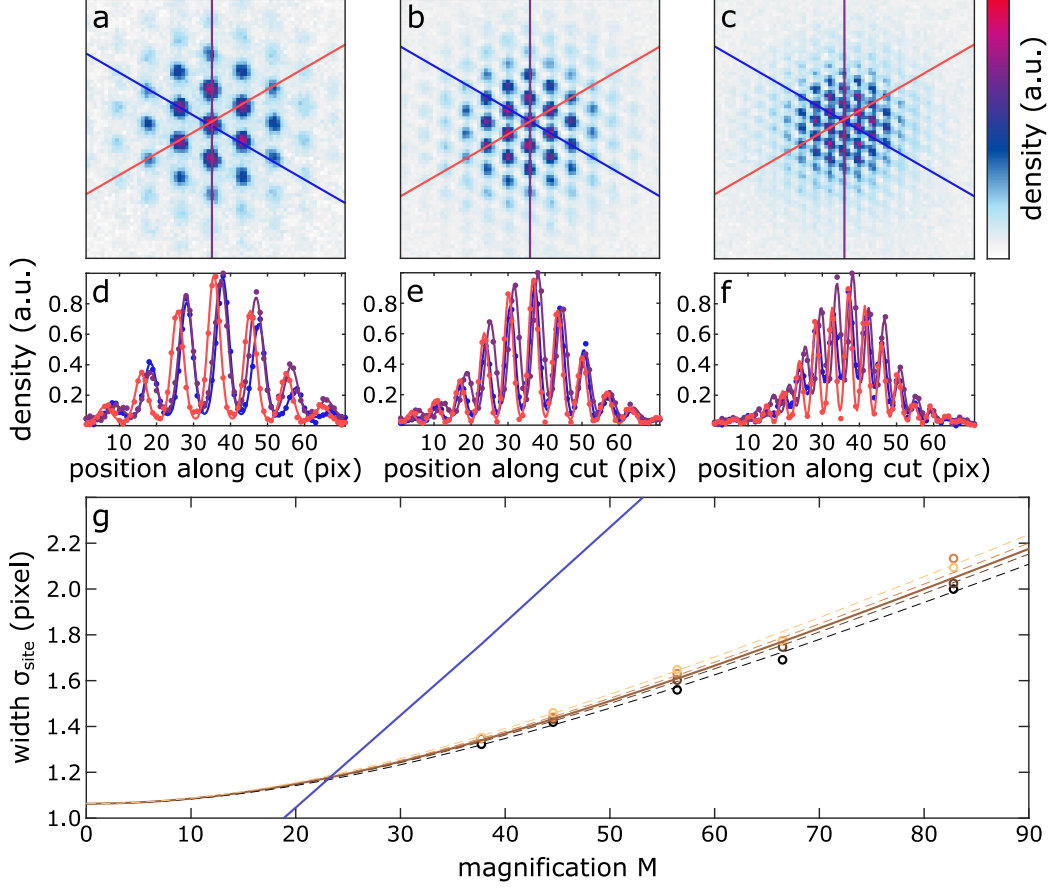
Figure 3.4.: Resolution of the quantum gas magnifier. **(a-c)**, example images obtained using the quantum gas magnifier with magnifications of (a) 83(1), (b) 56(1), and (c) 38(1). **(d-f)**, cuts through the images in (a-c) parallel to primitive vectors of the lattice (circles) fitted with a grid of Gaussians (lines). The color of the symbols and lines indicate the direction of the cut as shown in (a-c). **(g)**, Gaussian width of the on-site density distribution as a function of magnification (circles) color coded according to total particle number in the cloud. The particle numbers are $45(2) \times 10^3$, $54(3) \times 10^3$, $64(3) \times 10^3$, $72(2) \times 10^3$, from black to ochre. The data is fitted using a convolution of the actual size of the wave function and the resolution of the imaging system (3.18). The brown solid line corresponds to a fit of all data points whereas the dashed lines correspond to a fit only taking points with the same atom number into account. The blue line shows the maximal width allowed to be able to resolve single sites. Adapted from [22].

3.3. High precision thermometry

With the single site resolution verified we can move on with the first benchmark
experiment: a study of the thermal phase transition from a normal gas to a BEC in
a triangular lattice with harmonic external confinement. Measuring the temperature
of such a system can be very involved if only the momentum space distribution is
accessible [61–63]. Using the real-space density it is much easier as shown below.

We prepare the atoms in the magnetic trap as explained in chapter 2. We vary the
final evaporation frequency and add a hold time at the final evaporation frequency
in order to obtain atomic clouds of different particle numbers and temperatures.
Afterwards we ramp down the currents of the magnetic trap to have a trapping
frequency of $\omega_{\mathrm{sys}} = 2\pi \times 305\,\mathrm{Hz}$. We then ramp up the triangular lattice exponentially
within $400\,\mathrm{ms}$ to a lattice depth of $V_{\mathrm{lat}} = 1E_{\mathrm{r}}$ with the recoil energy $E_{\mathrm{r}} = h^2/(2m\lambda^2)$
where $m = 87\,\mathrm{u}$ is the mass of $^{87}\mathrm{Rb}$ and $\lambda = 1064\,\mathrm{nm}$ is the wavelength of the lattice
laser. This depth corresponds to a width of the lowest band of $k_{\mathrm{B}} \times 5.4\,\mathrm{nK}$ and a gap
between first and second band of $k_{\mathrm{B}} \times 290\,\mathrm{nK}$. Details on the lattice depth convention
and band structure simulation can be found in appendix B. After the loading we
image the resulting on-site populations. As explained earlier, to avoid interference
induced high densities during the matter-wave dynamics, we quench to a deep lattice
of $V_{\mathrm{lat}} = 6E_{\mathrm{r}}$ corresponding to a tunneling energy of $J/h \sim 1\,\mathrm{mHz}$. The on-site
populations are hence frozen and the coherence is removed by a hold time of $15\,\mathrm{ms}$
in the deep lattice. Eventually we switch off the lattice to initiate the quantum gas
magnifier protocol.

We extract the on-site populations by integration over the Wigner-Seitz cells (ap-
pendix D). Depending on the two experimental control parameters of final evaporation
frequency and hold time in the magnetic trap we observe different density distribu-
tions that correspond to a thermal, broad profile, or a bimodal profile of a broad
distribution with a narrow one on top (Fig. 3.5).

In a next step we need to extract the fraction of atoms in the BEC f_0 and the
temperature of the cloud T_0 in order to make quantitative statements about the
phase transition. To this end a model, and due to the high densities in the BEC a
model including interactions, is required. Let us start with the condensed part. It
can be shown that a coarse-grained density of a BEC in a lattice can be described
by a model without lattice with a renormalized interaction strength [64]. Here we
are interested in the on-site populations which is a special case of a coarse-grained
density and therefore the same reasoning applies. A BEC wave function $\psi(\boldsymbol{r})$ can be
described by the Gross-Pitaevskii equation [65]

$$-\frac{\hbar^2}{2m}\Delta\psi(\boldsymbol{r}) + V(\boldsymbol{r})\psi(\boldsymbol{r}) + g_{\mathrm{eff}}\left|\psi(\boldsymbol{r})\right|^2\psi(\boldsymbol{r}) = \mu\psi(\boldsymbol{r}). \qquad (3.19)$$

m is the mass of the particles, μ is the chemical potential and g_{eff} is the effective
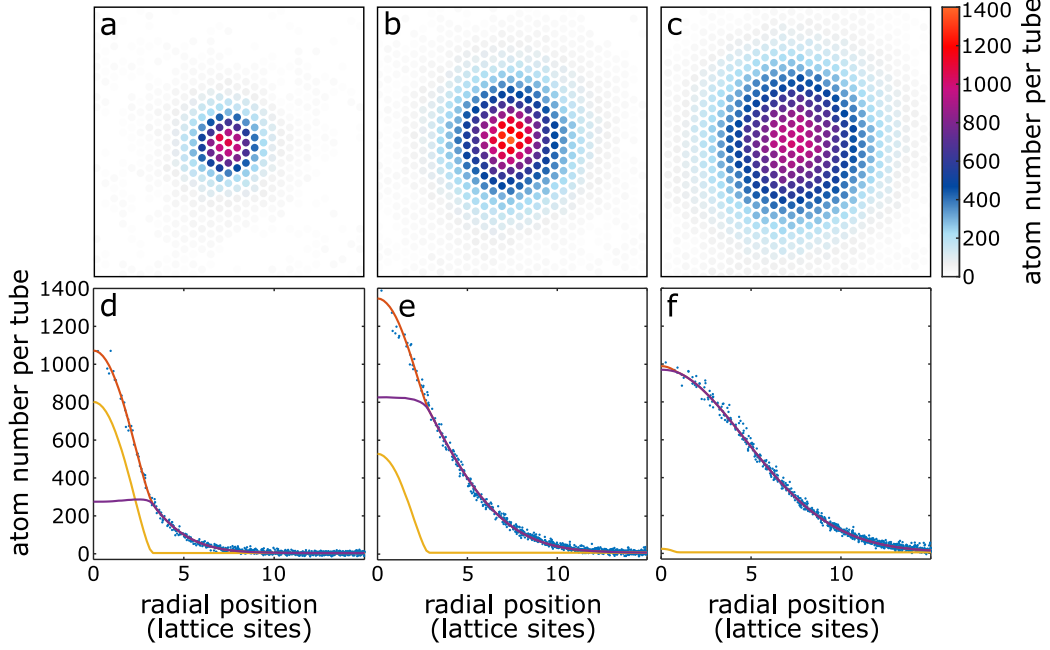
Figure 3.5.: Normal gas to superfluid transition in real space. **(a-c)**, example on-site populations of samples with (a) a high condensed fraction, (b) an intermediate one and (c) a normal gas. **(d-f)**, on-site populations of (a-c) as a function of radial position (circles). The plots always correspond to the image above them. The lines show a fit with the bimodal model explained in the main text. The orange line shows the full model, the yellow curve shows only the condensed part and the purple line represents the normal gas. (a,d) correspond to a temperature of $T = 171(1)\,\mathrm{nK}$ and an atom number of $N = 37.0(4) \times 10^3$, (b,e) to $T = 310(1)\,\mathrm{nK}$ and $N = 106.0(6) \times 10^3$, (c,f) to $T = 484(2)\,\mathrm{nK}$ and $N = 167.6(6) \times 10^3$. The errors correspond to the 68% confidence interval of the fit.

interaction strength. It is given by

$$\frac{g_{\mathrm{eff}}}{g} = A_{\mathrm{WS}} \int |w(x,y)|^4 \,\mathrm{d}x\mathrm{d}y, \tag{3.20}$$

where $g = 4\pi\hbar^2 a_{\mathrm{sc}}/m$ is the interaction strength derived from the s-wave scattering length a_{sc}, A_{WS} is the area of the Wigner-Seitz cell, and $w(x,y)$ is the Wannier function on a lattice site. We make an ansatz of a Gaussian Wannier function

$$w(x,y) = \frac{1}{2\pi a_{\mathrm{ho,site}}^2} e^{-\frac{x^2+y^2}{2a_{\mathrm{ho,site}}^2}} \tag{3.21}$$

with the on-site oscillator length $a_{\mathrm{ho,site}}$ (appendix B) and obtain

$$\frac{g_{\mathrm{eff}}}{g} = \frac{A_{\mathrm{WS}}}{2\pi a_{\mathrm{ho,site}}^2} = \frac{\sqrt{3}}{4\pi} \frac{a_{\mathrm{latt}}^2}{a_{\mathrm{ho,site}}^2}. \tag{3.22}$$

Here, $a_{\mathrm{lat}} = 2\lambda/3 = 709\,\mathrm{nm}$ is the lattice constant of the triangular optical lattice.

Let us now proceed with the solution of the Gross-Pitaevskii equation (3.19). For our parameters we are in the typical situation that the interaction term is very strong as can be seen from $Na_{\mathrm{sc}} \gg \bar{a}_{\mathrm{ho}}$ where we introduced the geometric mean $\bar{a}_{\mathrm{ho}} = (a_{\mathrm{ho},x}a_{\mathrm{ho},y}a_{\mathrm{ho},z})^{1/3}$ of the harmonic oscillator lengths $a_{\mathrm{ho},x_i} = \sqrt{\hbar/(m\omega_{\mathrm{sys},x_i})}$ of the external potential. The interactions induce a strong delocalization compared to the non-interacting ground state. Thus the kinetic energy term can be neglected which is known as Thomas-Fermi approximation [65]. As a result the equation is not differential any more and can be readily solved. The density is given by

$$|\psi(\boldsymbol{r})|^2 = \max\left[\frac{\mu - V(\boldsymbol{r})}{g_{\mathrm{eff}}}, 0\right], \qquad (3.23)$$

i.e., it consists of an inverted parabola for our case of a harmonic potential $V(\boldsymbol{r}) = m[\omega_{\mathrm{sys}}^2(x^2+y^2)+\omega_z^2 z^2]/2$. $\omega_z = 2\pi \times 29\,\mathrm{Hz}$ is the trapping frequency in z-direction, see appendix B for its computation. To be able to directly fit the experimental data we have to integrate over the z-direction and we have to do some change of parameters. With standard identities for the Thomas-Fermi approximation [65] we obtain the expression

$$n_{\mathrm{BEC}}(x,y) = \int \mathrm{d}z\, n_{\mathrm{BEC}}(x,y,z) = \int \mathrm{d}z \frac{15}{8\pi} \frac{N_{\mathrm{BEC}}}{R_\rho^2 R_z} \max\left[1 - \frac{x^2+y^2}{R_\rho^2} - \frac{z^2}{R_z^2}, 0\right], \quad (3.24)$$

where we introduced the total atom number in the BEC N_{BEC} and the Thomas-Fermi radii R_ρ and R_z.

For the thermal part of the cloud we take a so-called semi-ideal approach, i.e. we take into account the interaction that the BEC exerts onto the thermal atoms but neglect the one exerted by the thermal atoms onto the BEC or other thermal atoms. This is justified by the low density of the thermal atoms. Consequently the thermal atoms experience a potential that is given by

$$V_{\mathrm{th}}(\boldsymbol{r}) = V(\boldsymbol{r}) + 2g_{\mathrm{eff}}n_{\mathrm{BEC}}(\boldsymbol{r}). \qquad (3.25)$$

To obtain their resulting density distribution we treat the thermal gas in semi-classical approximation which assumes that the potential varies slowly on the length scale of the DeBroglie wavelength. This is fullfilled for the excited states and hence instead of using the exact eigenstates, the system can be thought of a collection of homogeneous boxes having eigenstates of sharp momentum and localized position. Thus the spectrum is $E_{\boldsymbol{p}}(\boldsymbol{r}) \approx \boldsymbol{p}^2/(2m) + V_{\mathrm{th}}(\boldsymbol{r})$ with the momentum $\boldsymbol{p}$ and the center of the box $\boldsymbol{r}$. Plugging this into the Bose-Einstein distribution and integrating over the momentum leads to a density distribution of

$$n_{\mathrm{th}}(\boldsymbol{r}) = \frac{1}{\lambda_T^3} g_{3/2}\left(e^{-\beta(V_{\mathrm{th}}(\boldsymbol{r})-\mu)}\right), \qquad (3.26)$$
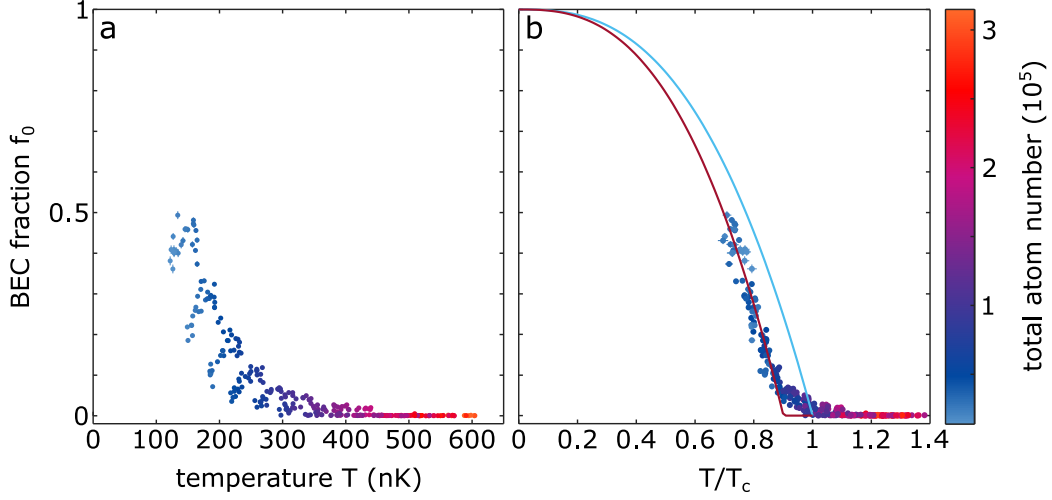
Figure 3.6.: BEC fraction as a function of temperature and atom number. **(a)**, fraction of condensed atoms as a function of temperature as obtained from the model described in the main text. The color encodes the total atom number of the sample. **(b)**, fraction of condensed atoms as a function of temperature normalized to the critical temperature of a non-interacting system T_c^0 (circles) also color-coded according to total atom number. The blue line shows a theoretic model without interactions based on a power-law density of states as explained in the main text. The red line is a fit to the data with the same model but allowing for a critical temperature that is scaled by a factor. Adapted from [22].

with $g_n(\boldsymbol{r}) = \sum_{m>0} x^m/m^n$ and $\lambda_T = \hbar\sqrt{2\pi/(mk_\mathrm{B}T)}$. Of course this expression also needs to be integrated along z to be comparable to our experimental images.

Eventually, to form the fit function we add the two parts n_BEC and n_th. As fit parameters we allow for a shift of the origin and we fit the temperature, the chemical potential, the number of particles in the BEC and the in-plane Thomas-Fermi radius R_ρ. The transverse Thomas-Fermi radius R_z is computed from R_ρ using the aspect ratio of the trap as $R_z = R_\rho\omega_\mathrm{sys}/\omega_z$. Additionally we allow for a small offset. In fact only for the lowest evaporation frequency the Thomas-Fermi radius and the number of particles in the BEC are treated as independent parameters. From theory a dependence of the type $R_\rho = \gamma N_\mathrm{BEC}^{1/5}$ is expected. The proportionality constant γ is determined from the fits at lowest evaporation frequency to be $\gamma = 0.354\,\mu\mathrm{m}$. Actually this value is extremely close to the one expected theoretically which is

$$\gamma_\mathrm{theo} = \frac{R_\rho}{N_\mathrm{BEC}^{1/5}} = 15^{1/5}\sqrt{\frac{\hbar\bar{\omega}}{m\omega_\mathrm{sys}^2}}\left(\frac{g_\mathrm{eff}}{g}\frac{a_\mathrm{sc}}{\bar{a}}\right)^{1/5} = 0.352\,\mu\mathrm{m}. \qquad (3.27)$$

Here we introduced the geometric mean of the trapping frequencies $\bar{\omega} = (\omega_\mathrm{sys}^2\omega_z)^{1/3}$.

The fit results provide a datapoint $f_0(T, N)$ for every image where N is the total atom number. These datapoints are plotted in Fig. 3.6a. In this representation, as expected, a clear dependence on both N and T can be seen.

For a non-interacting condensate, a critical temperature which depends on the particle number can be computed. If the temperature is measured in units of the critical temperature the explicit particle number dependence of the condensate fraction vanishes. Since the critical temperature depends to a large degree on the excited level structure—which is much less sensitive to interactions than the ground state—it makes sense to renormalize the temperature of our interacting system by the critical temperature of a non-interacting system. The computation of the critical temperature is based on determining the maximal number of atoms the excited states can accommodate for a given temperature.

Thus we compute the critical temperature T_c^0 for our system neglecting interactions (see Appendix B) and renormalize the temperature axis in the plot accordingly (Fig. 3.6b). We observe that in this representation all data points collapse onto a single curve. We can model this curve by the behaviour of a non-interacting system with a scaled critical temperature. Approximating the non-interacting density of states as a powerlaw $g(E) = C_\alpha E^{\alpha-1}$ (appendix B) results in a fit function $f_0 = 1 - (T/T_c)^\alpha$. The fit to all points with $f_0 > 0.1$ is shown in Fig. 3.6b as a red line and results in $T_c/T_c^0 = 0.901(4)$, where the error is the 68% confidence interval of the fit. Additionally we estimate a systematic error of 3% in the atom number determination which propagates to a 1% systematic error on the critical temperature.

Such a shift was already observed in the early BEC experiments [66]. There are several factors that can shift the critical temperature of a system. First of all the ground state energy is increased with interactions leading to a shift of [65, 67]

$$\frac{\Delta T_c}{T_c} \approx -1.33 \frac{g_{\text{eff}}}{g} \frac{a_{\text{sc}}}{\bar{a}} N^{1/6} \approx -0.24. \tag{3.28}$$

Here we used a typical value of $N = 5 \times 10^4$. This shift is larger than the one observed. However, for large shifts, this mean-field expression is expected to overestimate the correction [68]. Another effect is the finite particle number. The less particles are in the system the lower the critical temperature and the more relevant become the details of the level structure close to the ground state making the continuous density of state approximation less accurate. Sticking with the discrete density of states or using a more precise modelling of the continuous density of states results in a shift of [69]

$$\frac{\Delta T_c}{T_c} \approx -0.73 \frac{\omega_m}{\bar{\omega}} N^{-1/3} \approx -0.03, \tag{3.29}$$

where $\omega_m(\bar{\omega})$ is the arithmetic(geometric) mean of the trapping frequencies and where we used again $N = 5 \times 10^4$. The smoothing of the transition might also be connected to this effect. However, apart from the approximation as a coarse grained density, there is no established theory for the condensation in a 2D lattice with weak confinement in the third direction, making a precise theoretical prediction of the shift difficult.

3.4. Selective addressing and thermalization dynamics

Besides the ability to observe fine details it is also very desirable to have the ability to locally address the atomic sample in order to prepare interesting states. This has been achieved, e.g., by depletion via an electron beam [70], via a focused beam combined with a spin flip and optical push out [71], or by using a digital mirror device and deconfinement [72]. In our system we are able to locally address the lattice site populations using magnetic resonance techniques [73] which were also proposed for continuous wave function engineering [74]. Due to the magnetic trap, the energy separation between different m_F-levels has a spatial dependence (Fig. 3.7b). Therefore this transition can be locally addressed. Atoms that change their state to the $|F = 2, m_F = 1\rangle$ state are still trapped but they can decay collisionally to the $F = 1$ manifold [75] (Fig. 3.7c). When atoms reach the $m_F \leq 0$ levels via several transitions these are also lost since these states are not trapped or even anti-trapped. Hence we can locally deplete the lattice sites.

3.4.1. Pattern preparation

As described above, if we shine in RF-radiation atoms that fulfill the resonance condition will be lost from the trap. In practice, it requires a few 100 milliseconds to completely empty a lattice site and therefore the populations need to be frozen in a deep lattice for the duration of the RF preparation. The basic patterns available for this preparation are given by the shape of the iso-magnetic field surfaces. For our magnetic trap setup these are ellipsoids which are extremely elongated along line of sight, with aspect ratio that can reach 60 depending on the currents in the magnetic trap coils. Conveniently the optical lattice dominates the trapping frequency perpendicular to the plane making the aspect ratio of the atomic cloud in the lattice about three times smaller than the one given by the magnetic fields. Consequently the depletion happens for atoms at a fixed distance from the long trap axis without much dependence on the position along the same axis (Fig. 3.7a). Hence the resulting pattern in the image is a depleted circle (Fig. 3.7d). The radius of this circle can be shrunk to a single lattice site by applying a frequency very close to the central resonance condition (Fig. 3.7e). Using frequency sweeps, not only a single circle can be depleted but a whole annulus (Fig.3.7f). Due to the atoms being frozen in a deep lattice during the process, the magnetic trap and consequently the patterns can be shifted with respect to the atoms. This is realized by switching offset fields. This allows to move the iso-magnetic field surfaces so far off center such that only a single line of atoms is depleted (Fig. 3.7g). Here as well, sweeps can be implemented in order to remove half the system or to prepare a single line (Fig. 3.7h,i).

In principle the combination of the ability to have a single lattice site as a pattern and of the possibility to displace the pattern allows for arbitrary pattern preparation. Yet, in practice, the time required to empty a lattice site is too high to be able to write large patterns with such an approach. One possible solution to this could be
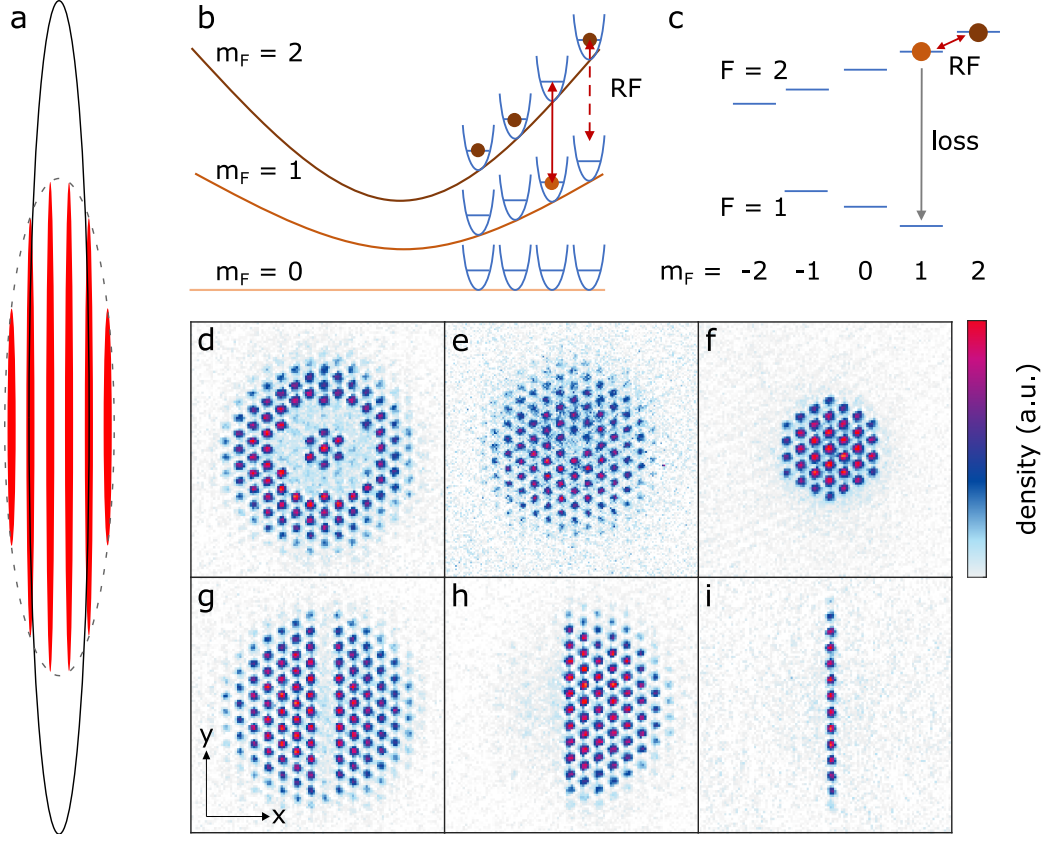
Figure 3.7.: State preparation via magnetic resonance. **(a)**, cut through the lattice of tubes perpendicular to the lattice plane. One iso-magnetic field surface (solid black ellipse) and one iso-potential surface (dashed gray ellipse) are shown. The aspect ratio of the iso-magnetic field surface exceeds the one of the iso-potential surface by three. Consequently, only two tubes intersect the iso-magnetic field surface in this cut. **(b)**, potential of the magnetic trap for the different m_F-levels. For a given RF frequency the transition between the m_F-levels is only resonant for atoms at a certain distance from the trap center. **(c)**, level scheme of the states $|F = 1, m_F = 0, \pm 1\rangle$ and $|F = 2, m_F = 0, \pm 1, \pm 2\rangle$ at finite magnetic field. Atoms in the $|F = 2, m_F = 1\rangle$ state can decay collisionally to the $|F = 1, m_F = 1\rangle$ state resulting in loosing them from the trap because they gain the energy corresponding to the hyperfine splitting. Due to angular momentum conservation such a channel does not exist for the stretched state $|F = 2, m_F = 2\rangle$. **(d-i)**, example images of prepared patterns. The resonance frequency at the trap center is $\omega_c/(2\pi) = 67\,\text{kHz}$ for (e) and $108\,\text{kHz}$ for the other images. The trap frequency during the addressing is $\omega_{\text{add}}/(2\pi) = 658\,\text{Hz}$ for (e) and $543\,\text{Hz}$ for the other images. (d-f) are obtained without shifting the trap. For (d) the RF frequency was $108.5\,\text{kHz}$, for (e) $67.2\,\text{kHz}$ and for (f) a sweep from 150 to $110\,\text{kHz}$ was used. (g-i) are obtained via a shift of $\sim 15\,\mu\text{m}$. The RF frequency was $360\,\text{kHz}$ for (g), a sweep from 360 to $290\,\text{kHz}$ was used in (h) and two sweeps, one from 494 to $540\,\text{kHz}$ and one from 420 to $486\,\text{kHz}$, were used in (i). Adapted from [22].

the use of a Raman transition to the other hyperfine ground state in combination with an optical push out of this state instead of the RF transition.

3.4.2. Relaxation dynamics of a triangular lattice of tubes

As an application of the state preparation via magnetic resonance we want to consider relaxation dynamics of a BEC in a triangular lattice with weak transverse confinement. Even though cold atom samples are isolated from the environment and therefore evolve according to unitary dynamics, this unitary dynamics typically evolves into a state that is indiscernible from a thermal state when only taking local observables into account [76]. This kind of behaviour is expected for generic interacting systems. But besides integrable systems, there is another class of systems that do not thermalize despite the presence of interactions. This phenomenon is called many-body localization and was observed experimentally in the regime of few atoms per site [77, 78]. Here we experimentally address the question of thermalization for an interacting system with large bosonic fillings which is initiated in a non-equilibrium state.

The initial state that we consider is a state with half of the system being depleted as shown in Fig. 3.7h. As can be seen in Fig. 3.8a the asymmetric density distribution decays smoothly to a symmetric one over a time which is of the order of seconds. We quantify the degree of asymmetry by the imbalance

$$\mathcal{I} = \frac{N_\mathrm{R} - N_\mathrm{L}}{N_\mathrm{R} + N_\mathrm{L}}, \tag{3.30}$$

where $N_\mathrm{R}(N_\mathrm{L})$ is the number of atoms in the right(left) half of the cloud. This quantity is plotted as a function of the hold time after the preparation for different initial temperatures in Fig. 3.8b. The temperature is extracted by fitting a sum of a Gaussian and an inverse parabola to half of the system (blue curve in Fig. 3.8c). The interaction between condensate and thermal part does not need to be taken into account here since it mainly affects the fitted BEC fraction which is not of importance for this experiment. The wings which define the temperature are barely affected for our experimental temperatures. We compute $T = m\omega_\mathrm{sys}^2\sigma^2/k_\mathrm{B}$, where σ is the width of the Gaussian fit. We observe that for low temperatures of up to $\sim 500\,\mathrm{nK}$ the imbalance does decay but does not reach zero within the observation time of more than $3\,\mathrm{s}$. The decay is faster the higher the initial temperature and for the curves with $T \geq 600\,\mathrm{nK}$ we observe the imbalance going to zero. We verify that the states with no imbalance are indeed thermal by fitting not only one half but the full system (red curve in Fig. 3.8c). We obtain very good agreement with negligible contribution from the inverted parabola showing that the density relaxed indeed to the one of a thermal state.

For every initial temperature we can fit an exponential curve $\mathcal{I}(t) = \mathcal{I}_0 \exp(-\Gamma t)$ with the initial imbalance $\mathcal{I}_0$ and the thermalization rate Γ as fit parameters. The thermalization rate as a function of temperature is shown in Fig. 3.8d. We model the
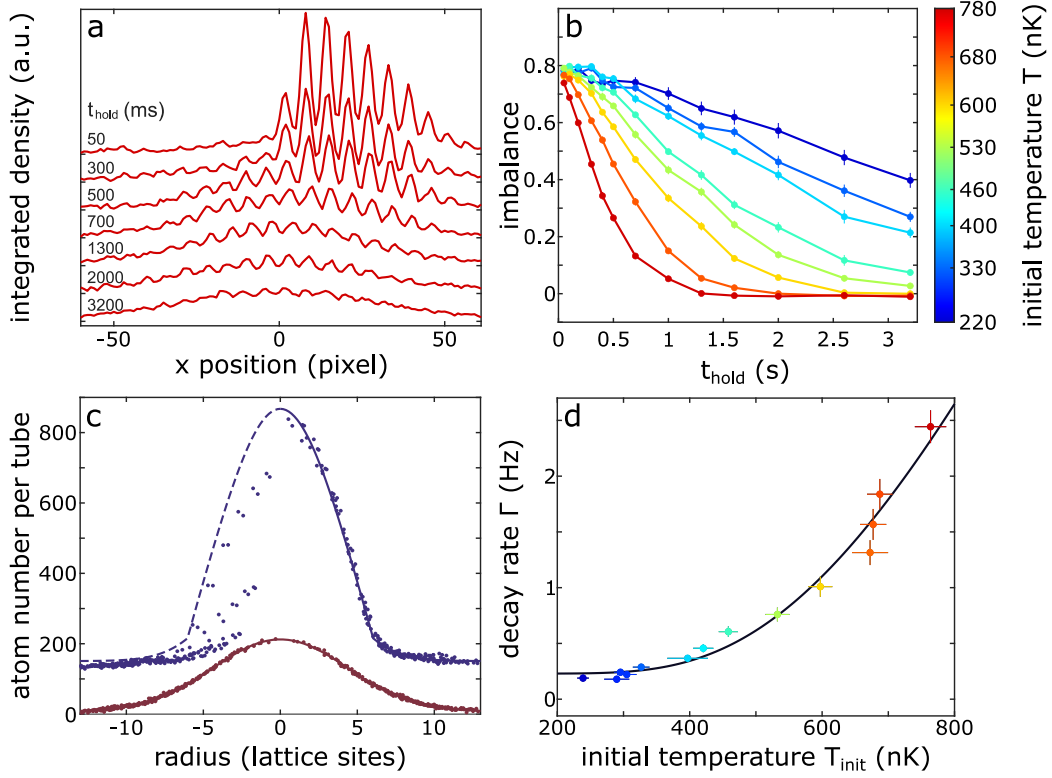
Figure 3.8.: Relaxation dynamics. **(a)**, cut through the cloud for different hold times as denoted in the figure. Different hold times are vertically displaced for clarity. **(b)**, imbalance $\mathcal{I}$ as defined in the main text, as a function of hold time after the preparation for different initial temperatures, which are color-coded. The precise values are given by the ticks of the colorbar. **(c)**, average on-site populations as a function of radial distance after 50 ms of hold time and after 3.2 ms of hold time. The lines are bimodal fits to the data where for the early time only the right half of the sample is taken into account resulting in an initial temperature of 680(50) nK and a final temperature of 1.25(4) μK. **(d)**, Decay rate of the imbalance Γ as a function of the initial temperature, color-coded also according to initial temperature. The line corresponds to a fit with an Arrhenius law as described in the main text. Adapted from [22].

temperature dependence of the rate by Arrhenius law [79] which can be used to model processes that occur due to thermal activation. Here these processes correspond to the excitation to states which are not trapped in the lattice but only by the magnetic trap resulting in long-range hopping. The law assumes an attempt rate Γ_a of trying

to escape the lattice well and a barrier height V_B. The hopping rate is then given by

$$\Gamma_h \approx \Gamma_a P(E > V_B) \tag{3.31}$$

$$= \Gamma_a \times \frac{1}{k_B T} \int_{V_B}^{\infty} e^{-\frac{E}{k_B T}} \, dE \tag{3.32}$$

$$= \Gamma_a e^{-\frac{V_B}{k_B T}}, \tag{3.33}$$

where $P(E > V_B)$ is the probability to have an energy larger than the barrier. Since this thermal hopping is long ranged it is not necessary to treat the atoms with different distance to the other half in a particular way. We assume the hopping rate Γ_h to be equal to the decay rate of the imbalance Γ because on the one hand a redistributed particle only has a probability of only $1/2$ to change halfs but on the other hand if it does change it is removed from one half and added to the other, which doubles the impact on the imbalance of this process. We add an offset rate Γ_0 to the model which might be due to quantum tunneling in higher bands. The fit of the data in Fig. 3.8d results in $V_B = k_B \times 2.4(6)\,\mu K$, $\Gamma_0 = 0.23(8)\,Hz$ and $\Gamma_a = 52(44)\,Hz$. From the lattice depth calibration we obtain a value of $V_{lat} = 3E_r$ which corresponds to a barrier height of $V_B = k_B \times 2.6\,\mu K$ in the triangular lattice consistent with the fit result.

In conclusion we can confirm that indeed a non-equilibrium state in a lattice with large fillings of interacting bosons does decay to a thermal state. However for low temperatures the relaxation is so slow that equilibrium is not reached within experimental time scales. Equilibrium can only be observed for higher temperatures where thermal hopping is significant.

3.5. Sub-lattice site dynamics

So far we only considered on-site populations, i.e., the continuous density was integrated over the area of the Wigner-Seitz cell to obtain a discrete density. However, with the quantum gas magnifier we can also resolve the density distribution on the lattice sites themselves. As explained earlier, to have access to this kind of information, we need to refrain from freezing the density during the experimental protocol since even though the on-site populations are unaffected by this step, the continuous density gets modified. There are also other techniques capable of resolving features below the lattice constant such as scanning electron microscopy [33] and super-resolution microscopy [35, 36]. An advantage of the quantum gas magnifier over these scanning techniques is that it obtains the density of a sample in a single shot. Furthermore, like the scanning electron microscopy [33], the quantum gas magnifier can image the density on every lattice site independently whereas super-resolution microscopy [35, 36] averages the profiles on all lattice sites.

As a demonstration of the sub-lattice site resolution we perform a quench experiment: we load a deep boron-nitride lattice, thus populating only one sublattice initially (Fig. 3.9b). Then we quench two lattice beams to half of their intensity which
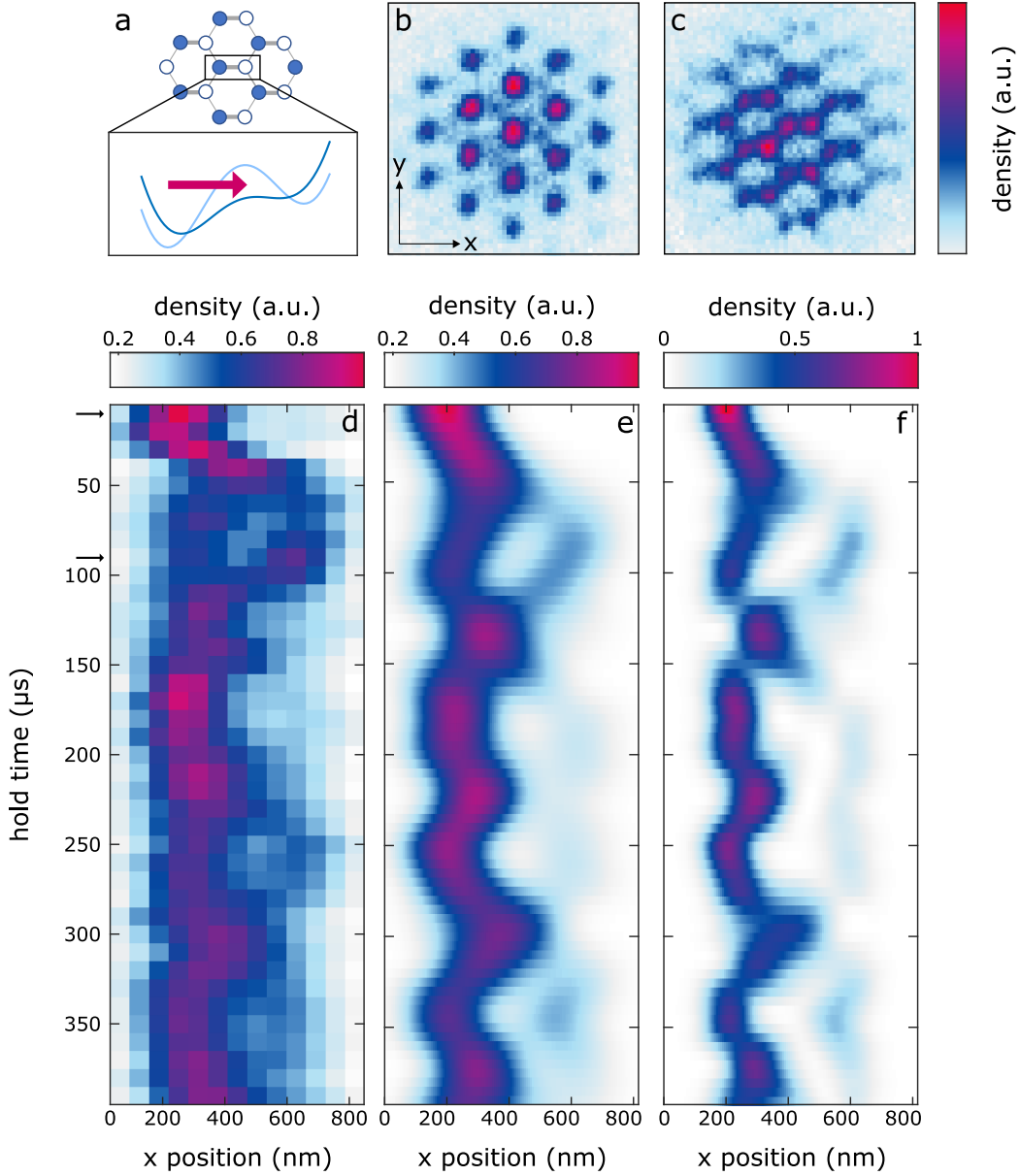
Figure 3.9.: Nanoscale dynamics. **(a)**, schematic of the dimerized boron-nitride lattice. In the box the potential before (light blue line) and after the quench (blue line) is shown. **(b,c)**, example images for (b) $10\,\mu s$ and (c) $90\,\mu s$ after the quench. **(d)**, average density along a cut through the dimers that have at least 50% of the population of the most populated dimer as a function of x and time after the quench. The arrows indicate the hold times of (b,c). **(e)**, the same density as resulting from the numerical band structure calculation including an offset and a convolution with a Gauss filter as explained in the main text. **(f)**, the same numerical results but without offset and filter.

results in the potential landscape suddenly changing to a dimerized boron-nitride lattice with much larger tunnel coupling within the dimers compared to before the quench. Additionally the potential minima move closer to each other (Fig. 3.9a). Thus, dynamics between the dimer sites but also within the dimer sites is induced. We track the dynamics by reducing each dimer to a 1D representation by reading out a centered horizontal cut through the dimers. Subsequently we average over all cuts corresponding to dimers that have at least half the population of the most populated dimer. These averaged cuts are plotted in Fig. 3.9d for different hold times after the quench. Indeed we observe both dynamics on the individual wells as well as population transfer between the wells. In this experiment we used strong confinement resulting in a measured magnification of 93(1).

For the theoretical modelling we use a numerical non-interacting band structure simulation. The neglection of interactions is justified given the short evolution time in the experiment. We assume the initial state to be the Bloch wave of zero quasi-momentum of the lowest band. After the quench we compute the instantaneous eigenstates using the voltages from our intensity control photodiodes of the lattice beams, decompose the initial state accordingly and evolve it using the instantaneous eigenvalues. We find good agreement with the experiment for an initial lattice depth of $V_{\text{lat}} = 32E_{\text{r}}$. Due to the finite resolution of our imaging system we need to apply a Gauss filter of $76\,\text{nm} \approx 0.2a_{\text{AB}}$ width when comparing to the experimental data, as well as including an offset (Fig. 3.9e,f). Here a_{AB} is the distance between the sites in the dimers. For details concerning the simulation see appendix B or the thesis of Luca Asteria [57]. With the good agreement between theory and experiment we demonstrated the capability to observe sub-lattive site dynamics using quantum gas magnification.

3.6. Fluctuation analysis

The quantum gas magnification protocol rescales the atomic density preserving its fluctuations. In this section we want to show analyses of the on-site fluctuations of bosons in an optical lattice for different regimes: thermal, superfluid, and Mott-insulator. We find good agreement of the thermal fluctuations of a normal gas with a model of a grand-canonical ensemble on each lattice site for small to intermediate tube populations. For a superfluid sample we observe fluctuations that are close to Poissonian statistics whereas for Mott-insulating sample we observe number squeezing, eventually leading to subpoissonian statistics.

3.6.1. Thermal fluctuations

As a first analysis we want to consider thermal fluctuations, i.e., the on-site fluctuations of a thermal gas. One possibility to model the fluctuations of such a system is by assuming that each lattice site is described by a grand-canonical ensemble with the

other lattice sites constituting the thermal bath and particle reservoir. In the grand-canonical ensemble the particle number fluctuations are given by the variance [80]

$$\Delta N^2 = k_{\mathrm{B}} T \frac{\partial \langle N \rangle (\mu, T, V)}{\partial \mu}, \tag{3.34}$$

where T is the temperature of the bath, μ is the chemical potential of the reservoir and V is the volume of the system. The particle number can be computed according to

$$\langle N \rangle = k_{\mathrm{B}} T \frac{\partial \ln \Xi (\mu, T, V)}{\partial \mu}, \tag{3.35}$$

where

$$\Xi = \sum_{N \geq 0} \frac{1}{h_{\mathrm{cl}}^{3N} N!} \int \mathrm{d}^{3N} q \int \mathrm{d}^{3N} q \, e^{-\frac{1}{k_{\mathrm{B}} T} (H_N(\boldsymbol{q}, \boldsymbol{p}) - \mu N)} \tag{3.36}$$

is the grand-canonical partition function with h_{cl}^3 being the classical elementary volume of phase space and $H_N(\boldsymbol{q}, \boldsymbol{p})$ being the classical Hamiltonian function for N particles with positions $\boldsymbol{q} = (q_x^{(1)}, q_y^{(1)}, q_z^{(1)}, q_x^{(2)}, ..., q_z^{(N)})$ and momenta $\boldsymbol{p} = (p_x^{(1)}, p_y^{(1)}, p_z^{(1)}, p_x^{(2)}, ..., p_z^{(N)})$. The number fluctuations as a function of the mean particle number can be computed with very little assumptions. Actually it suffices to assume that the Hamiltonian can be written as

$$H_N(\boldsymbol{q}, \boldsymbol{p}) = \sum_{i=1}^{N} H_{\mathrm{kin}} \left(\boldsymbol{p}^{(i)} \right) + \sum_{i=1}^{N} H_{\mathrm{pot}} \left(\boldsymbol{q}^{(i)} \right), \tag{3.37}$$

which is possible when neglecting interactions, and if no magnetic fields are present or the particles are neutral. Under this assumption the integrals factorize and the partition function takes the form

$$\Xi = \sum_{N \geq 0} \frac{1}{h_{\mathrm{cl}}^{3N} N!} (I_q I_p)^N e^{\frac{\mu N}{k_{\mathrm{B}} T}}, \tag{3.38}$$

where we defined the abbreviations $I_q = \int \mathrm{d}^3 q \exp(-H_{\mathrm{pot}}(\boldsymbol{q})/(k_{\mathrm{B}} T))$ and $I_p = \int \mathrm{d}^3 p \exp(-H_{\mathrm{kin}}(\boldsymbol{p})/(k_{\mathrm{B}} T))$. The sum in (3.38) is actually an exponential function resulting in

$$\Xi = \exp \left(\frac{I_q I_p}{h_{\mathrm{cl}}^3} e^{\frac{\mu}{k_{\mathrm{B}} T}} \right). \tag{3.39}$$

Thus, $\ln \Xi$ is just an exponential function of μ resulting in

$$\Delta N^2 = k_{\mathrm{B}} T \frac{\partial \langle N \rangle (\mu, T, V)}{\partial \mu} = k_{\mathrm{B}} T \frac{1}{k_{\mathrm{B}} T} \langle N \rangle = \langle N \rangle. \tag{3.40}$$

Hence, counter-intuitively, as long as the temperature is finite, the thermal fluctuations do not explicitly depend on temperature but are just given by the mean atom number.

As a matter of fact, without any further assumptions, the probability distribution can be shown to not only have Poissonian fluctuations but to actually be Poissonian. In the grand-canonical ensemble, the probability to have N particles in the system is given by integrating the microstate probabilities for this particle number over the positions and momenta of the particles

$$w_N(\mu, T, V) = \frac{1}{\Xi} \frac{1}{h_{\mathrm{cl}}^{3N} N!} \int \mathrm{d}^{3N} q \int \mathrm{d}^{3N} q \, e^{-\frac{1}{k_{\mathrm{B}} T}(H_N(\boldsymbol{q}, \boldsymbol{p}) - \mu N)}. \tag{3.41}$$

Using (3.35) and (3.39) the expression simplifies to

$$w_N(\mu, T, V) = \frac{\langle N \rangle^N}{N!} e^{-\langle N \rangle}, \tag{3.42}$$

which is the Poissonian distribution with mean $\langle N \rangle$.

To investigate thermal fluctuations experimentally we can consider the same data as in section 3.3. As outlined in the theory part above we can consider every site as a grand canonical ensemble and the rest of the system as thermal bath and particle reservoir. Every measurement thus provides us with a multitude of realizations of this ensemble. To obtain the desired statistics we need to group similar sites. Similar in this case means that the relevant grand-canonical parameters, i.e., the chemical potential, or equivalently the mean atom number, and the temperature are similar. Since we can model the density profile very precisely as shown in section 3.3, we use this fit to extract these parameters, where only the images with a condensate fraction of less than 10% are kept in order to isolate the thermal fluctuations. The temperature is directly given as a fit parameter and the mean atom number associated to a site is assumed to be the value the fit function takes on this particular site. Subsequently the site populations are binned with bin sizes of $L_N = 20$ atoms and $L_T = 67 \, \mathrm{nK}$ and within these bins the variance is computed. The resulting curves of variance as a function of mean atom number for different temperatures are plotted in Fig. 3.10a. It can be seen that for site populations of up to ~ 500 atoms the fluctuations are in good agreement with (3.40) which corresponds to the straight line. This is consistent with the observation that for these occupations the example histograms for the bins shown in Fig. 3.10b-g can be described by a Poissonian distribution with the same mean value. There is no significant temperature dependence for all site populations measured. Note that a bin of length L_N atoms that has a homogeneous distribution of atom numbers within these boundaries has a variance of $L_N^2/12$ which is small compared to the computed fluctuations.

For larger site populations the fluctuations rise above the theoretical expectation. There can be several explanations for this. The first we want to consider is the shot noise of the imaging laser. We can compute the fluctuations that we expect to occur
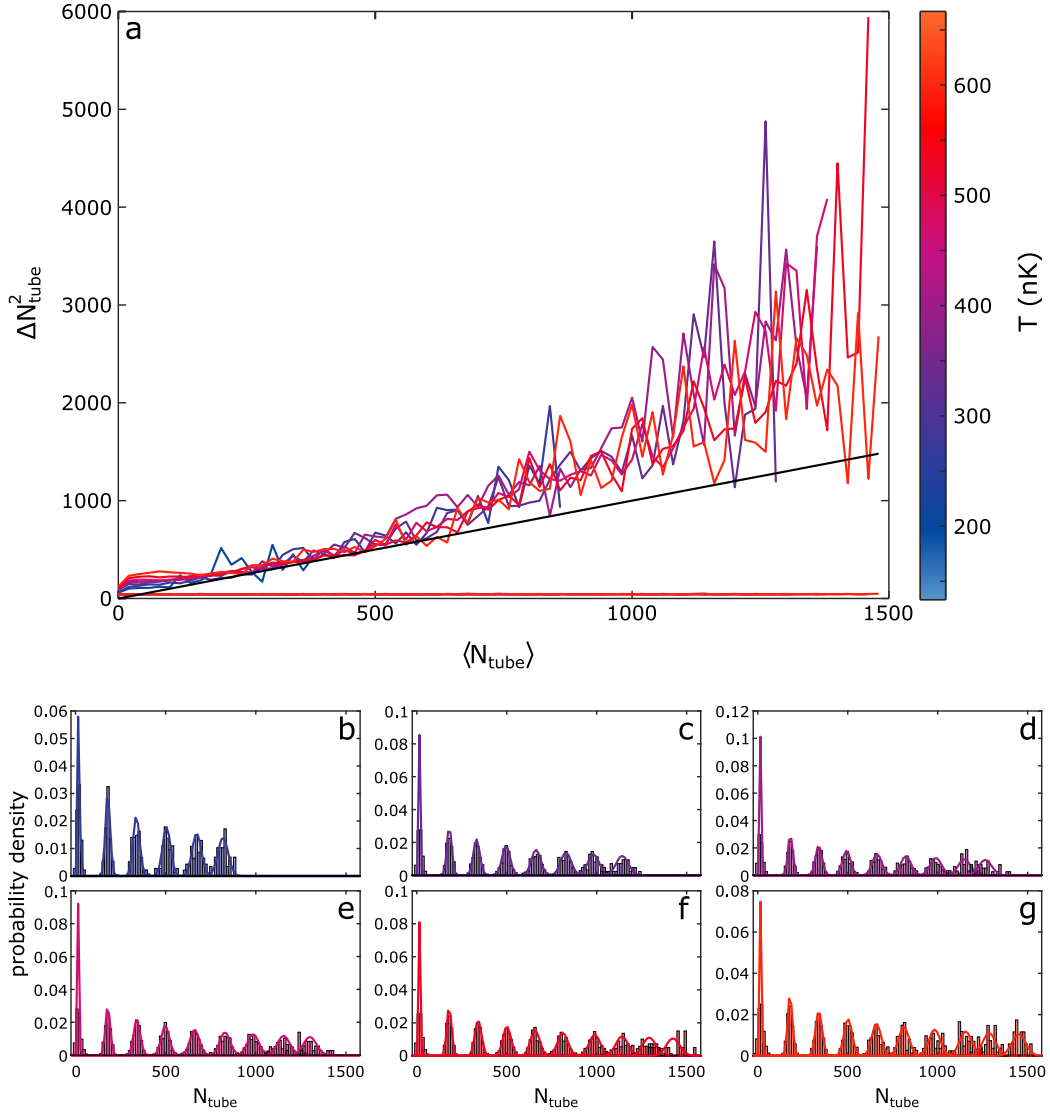
Figure 3.10.: Thermal fluctuations. **(a)**, variance of the site populations as a function of the mean site population. The black line is of unity slope and thus is the expectation for Poissonian statistics, the approximately horizontal lines show the computed variance from shot noise according to the combination of (3.43 - 3.45). Note that these curves are almost independent of mean site population and temperature and therefore appear as essentially one line. The remaining curves correspond to the variance of the measured site populations. The color encodes the temperature of the data. **(b-g)**, several example histograms of certain bins for different temperatures. The bars show the probability density of the site populations within the bins, the lines show Poissonian distributions with the same mean values as the example bins. The subplots correspond to different temperature bins with central temperatures of $(267, 333, 400, 467, 533, 600)\,$nK starting from (b) and ending with (g).

due to this reason via error propagation of (2.11) to obtain

$$\Delta n(x,y)^2 = \frac{1}{\sigma_0^2}\left[\left(1+\frac{CN_\text{abs}}{I_\text{sat}}\right)^2\left(\frac{\Delta N_\text{abs}}{N_\text{abs}}\right)^2 + \left(1+\frac{CN_\text{ref}}{I_\text{sat}}\right)^2\left(\frac{\Delta N_\text{ref}}{N_\text{ref}}\right)^2\right]. \quad (3.43)$$

Assuming the error on the camera counts being given by the shot noise of the photon counts leads to

$$\left(\frac{\Delta N_\text{abs}}{N_\text{abs}}\right)^2 = \frac{1}{C_\gamma N_\text{abs}}, \quad \left(\frac{\Delta N_\text{ref}}{N_\text{ref}}\right)^2 = \frac{1}{C_\gamma N_\text{ref}}, \quad (3.44)$$

where $C_\gamma = 4.6$ (see Appendix C) is the conversion factor from digital counts to the number of photons incident on the pixel. For a single pixel we obtain a typical value of

$$\Delta N^2 = \Delta n^2 \left(\frac{A_\text{pixel}}{M^2}\right)^2 \approx 3.6 \quad (3.45)$$

assuming $N_\text{ref} = 4000$ and $N_\text{abs} = 2000$ which already corresponds to a dense part of the cloud, i.e. a part that suffers more from shot noise. The variance for a lattice site population is computed by adding up the variance from each pixel within the corresponding Wigner-Seitz mask. A lattice site consists of about 12 pixels, hence the shot noise induced variance of the on-site populations is about one order of magnitude higher than the one of a single pixel. This variance is computed for every site and the mean is taken within every bin which is also plotted in Fig. 3.10a. The resulting expected fluctuations are of the same order as the observed y intercept of the fluctuation curves. However the shot noise is almost constant as a function of on-site population since only very few pixels increase in noise due to the reduction of absorption counts as a consequence of high atomic density. Consequently we can exclude shot noise as the reason for the superpoissonian variance of high site populations. A cause for the superpoissonian variance might be the fit being less accurate for the more populated tubes which tend to be in the center of the cloud. Indeed the center of the cloud effectively is weighted less in the fit because the fit has radial symmetry and more data points are located on the iso-density lines in the wings than in the centre.

Still, the observation that the extracted fluctuations hit the Poissonian limit shows that at least for that regime density fluctuations are preserved and can be analyzed using the quantum gas magnifier. This conclusion can be made due to the fact that without quantum mechanical squeezing, which is not expected here, the fluctuations are not expected to be subpoissonian and thus any imperfection in preparation or analysis should produce superpoissonian statistics whereas Poissonian statistics imply that no other sources of fluctuations than the physical ones can be present.

3.6.2. Quantum fluctuations

Thermal fluctuations can only be made visible via a measurement, however the deviation from the mean value is present also before and independently of the measurement.

This is not the case for quantum fluctuations. Here, all possible deviations from the mean are incorporated in the wave function of the system and only the measurement projects the wave-function onto a particular realization of the fluctuation.

We want to investigate quantum fluctuations of superfluid and Mott-insulating states in analogy to experiments performed in 2D systems [30, 31, 81]. The ground state of a weakly interacting lattice Hamiltonian can be rewritten as a product of coherent states on the lattice sites. Therefore the on-site fluctuations are expected to follow a Poissonian distribution in a superfluid lattice phase [82]. When interactions are increased above some critical value, a quantum phase transition to the Mott-insulating state takes place [46]. In this phase it is favourable to have the particles localized on the lattice sites because the interaction energy imposes an energy penalty on delocalization. The localization of the particles reduces the on-site fluctuations, in the limit of infinite interaction strength and zero temperature they even go to zero.

In order to prepare a Mott-insulating state we need to drastically increase the interaction strength among the particles and reduce the number of atoms per lattice site as compared to the previous experiments which we can both realize by the addition of a lattice perpendicular to the in-plane lattice, thus obtaining a 3D-lattice. This additional lattice is realized by retro-reflecting a dipole trap beam. It is derived from a titanium-sapphire laser at 826 nm which is pumped by a diode pumped solid state laser at 532 nm.

In this experiment we use the polarization approach (section 2.3.1) to obtain a boron-nitride lattice and we read out the lattice site populations correspondingly (appendix D). According to band structure simulations (appendix B) we have a ratio of bandgap over bandwidth of at least 70 and we will thus consider the two sublattices of the boron-nitride as independent triangular lattices and we will only analyse the energetically lower sublattice. As for the thermal fluctuation analysis the crucial step is to identify for every on-site population the probability distribution it is drawn from. Here we assume the temperature to be sufficiently low or at least sufficiently stable such that the only varying parameter determining the statistics is the mean atom number integrated along line of sight. A few comments concerning the connection of integrated signal and full 3D system are to be made: the mean atom number per site, which determines the fluctuations, follows from its integral along line of sight in combination with the z-confinement which is spatially homogeneous. Therefore tubes of identical atom number are comparable. Also note that the sum over random variables following a Poissonian distribution will also be described by a Poissonian distribution. The same argument obviously holds for a distribution with no fluctuations, other distributions however will likely be modified, but in a monotonous way, i.e., if all local fluctuations decrease also the absolute fluctuations of the integrated signal will decrease.

In this dataset we have about 200 repetitions for every parameter and we therefore do not need to model the density envelope function by a fit but we can derive it from the data. To associate a mean value to every tube population, where by tube population we mean on-site populations integrated along a line of sight, we compare

every shot to all shots that were taken at the same experimental parameters. This is carried out for every tube population in the following way: First, all other images are rescaled such that the atom number matches the one of the current shot, which is a small correction. Subsequently from all these tube populations those are selected which have coordinates on the camera, i.e., relative to the magnetic trap, which are closest to the tube for which we want to derive the expectation value. In practice the 10 closest ones are selected and averaged. The result is considered the best estimate of the mean tube population. Eventually the tube populations are grouped according to their mean tube population with a bin size of 10 atoms. The variance within these bins is plotted for different lattice depths in Fig 3.11a. One data set originating from a superfluid sample, i.e. with no lattice perpendicular to the 2D lattice, is also included as a dashed line. Furthermore some example distributions within the bins are plotted in Fig. 3.11b-g.

All curves start above the value for poissonian statistics but bend to the right and cross the reference line for Poissonian statistics at some point indicating number squeezing. The reduction of fluctuations with increasing tube population is stronger for deeper lattices as expected for an interaction induced effect. The reason for the dashed line corresponding to the superfluid also going subpossonian might be that very high densities induce number squeezing even without lattice perpendicular to the plane, as for example computed for a 1D lattice of pancakes [83]. As for the thermal fluctuations we also computed the fluctuations expected from shot noise (Fig. 3.11a) which describe well the offset of the curves. The shot noise is stronger in this dataset because the imaging beam intensity was significantly lower.

In order to compare these results to theoretical models, the Hubbard parameters need to be estimated. We perform a band structure calculation (appendix B) and as described above, we approximate the lower band by the dispersion of a triangular lattice [84]

$$E(\boldsymbol{k}) = 8J_{2\mathrm{D}} - 4J_{2\mathrm{D}} \cos\left(\frac{k_x a_{\mathrm{lat}}}{2}\right) \left[\cos\left(\frac{k_x a_{\mathrm{lat}}}{2}\right) + \cos\left(\frac{\sqrt{3}k_y a_{\mathrm{lat}}}{2}\right)\right], \qquad (3.46)$$

where $J_{2\mathrm{D}}$ is the only fit parameter. The tunneling energy in z-direction is obtained via the formula for the tight-binding limit [85]

$$J_z = \frac{4}{\sqrt{\pi}} E_{\mathrm{r},z} \left(\frac{V_{\mathrm{lat},z}^{\mathrm{pp}}}{E_{\mathrm{r},z}}\right)^{3/4} \exp\left(-2\sqrt{\frac{V_{\mathrm{lat},z}^{\mathrm{pp}}}{E_{\mathrm{r},z}}}\right), \qquad (3.47)$$

where $V_{\mathrm{lat},z}^{\mathrm{pp}}$ is the peak to peak potential depth of the lattice in z-direction and $E_{\mathrm{r},z} = h^2/(2m\lambda_z^2)$ is the recoil energy in z-direction with $\lambda_z = 826\,\mathrm{nm}$ being the titanium-sapphire laser wavelength. Since $V_{\mathrm{lat},z}^{\mathrm{pp}}/E_{\mathrm{r},z} > 12$ the use of this approximation is justified. Eventually, the on-site interaction strength is determined by [85]

$$U = g \int \mathrm{d}\boldsymbol{r} \, |w(\boldsymbol{r})|^4, \qquad (3.48)$$
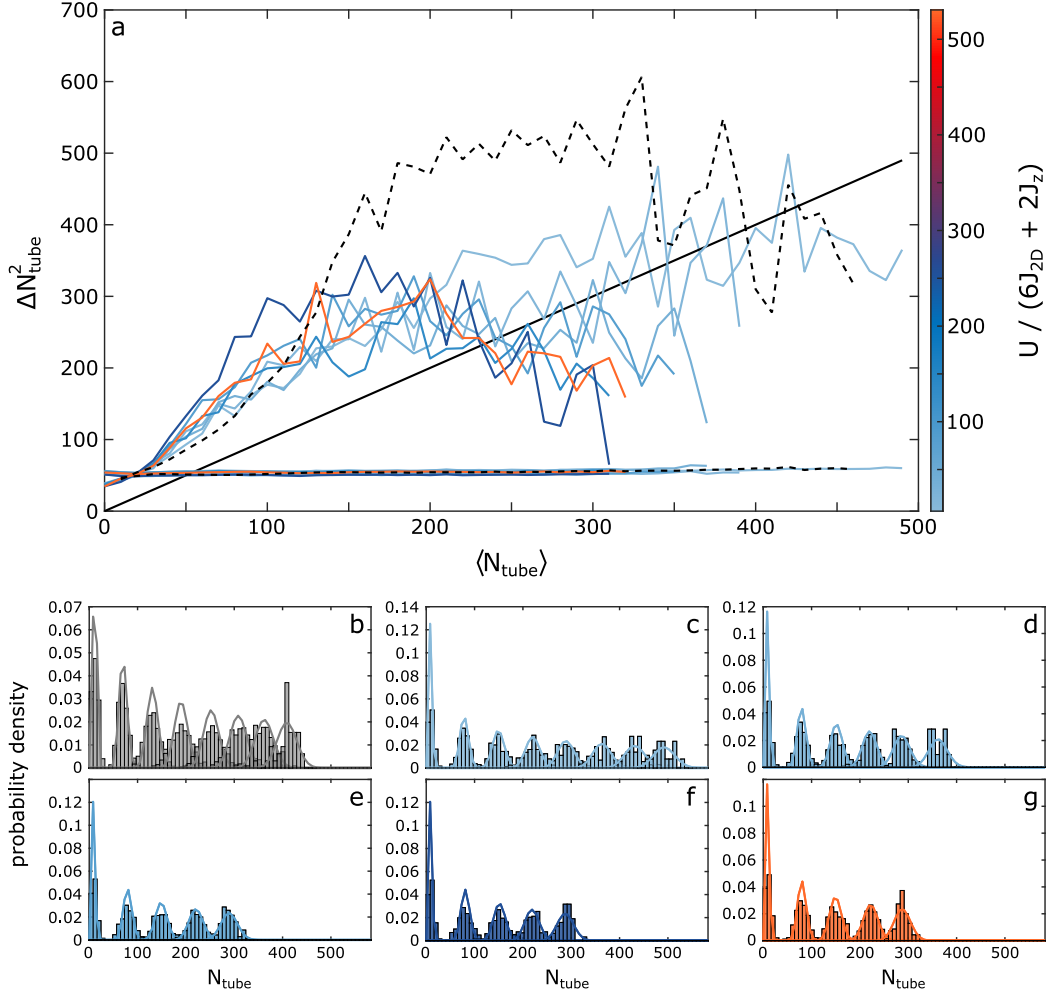
Figure 3.11.: Quantum fluctuations. **(a)**, variance of the site populations as a function of the mean site population. The approximately horizontal lines show the computed variance from shot noise according to the combination of (3.43 - 3.45), the black line is of unity slope and thus is the expectation for Poissonian statistics. The remaining solid lines correspond to the variance of the measured site populations. The color encodes the parameter $U/(6J_{2D}+2J_z)$ of the data. The dashed line corresponds to a system without lattice perpendicular to the 2D lattice with $J_{2D}/h = 43\,\text{Hz}$. For the other curves J_{2D} is in the range from $0.25\,\text{Hz} - 7\,\text{Hz}$. **(b-g)**, example histograms for certain bins. The bars show the probability density of the site populations within the bins, the lines show Poissonian distributions with the same mean values as the example bins. (b) corresponds to the measurement without lattice in the third dimension, the subplots (c-g) correspond to different $U/(6J_{2D} + 2J_z)$ of (6.5, 35, 81, 259, 531) starting from (c) and ending with (g).

with the Wannier function $w(\boldsymbol{r})$. For the Wannier function we make the approximation of a deep lattice, i.e. assuming that it is given by the ground state of a harmonic oscillator with trapping frequencies equal to the on-site trapping frequencies of the lattice sites. This results in

$$U = \frac{g}{(2\pi)^{3/2}a_{\mathrm{ho,2D}}^2 a_{\mathrm{ho},z}},$$
(3.49)

where $a_{\mathrm{ho,2D}}$ denotes the on-site oscillator length in the plane and $a_{\mathrm{ho},z}$ the on-site oscillator length in z-direction. To determine the on-site trapping frequency in the plane we perform a parabolic fit close to a minimum of the in-plane potential and compute the oscillator length from it. The z oscillator length is analytically computed as $a_{\mathrm{ho},z} = \lambda_z/(2\pi) \times (V_{\mathrm{lat},z}^{\mathrm{pp}}/E_{\mathrm{r},z})^{-1/4}$.

The phase boundary between Mott-insulator and superfluid is expected to be at [86]

$$\left(\frac{U}{zJ}\right)_{\mathrm{c}} = 2n + 1 + \sqrt{(2n+1)^2 - 1}$$
(3.50)

for a Mott-insulator with n particles per lattice site and a lattice with coordination number z. The right hand side equals 5.83 for $n = 1$. We generalize the expression to our anisotropic lattice by replacing zJ by $6J_{\mathrm{2D}} + 2J_z$. We obtain values for $U/(6J_{2D} + 2J_z)$ that start from slightly above the $n = 1$ transition value and go up to almost 100 times this value. Therefore we can expect that also higher n Mott-insulators can form resulting in a 3D version of the prominent wedding cake profile of a trapped 2D system. Since we integrate along the z direction this profile could hardly be observed because the sharp features wash out upon integration [87]. Furthermore superfluid or thermal shells would explain why the fluctuations do not drop to the background level for the strongest interactions.

Thus we have demonstrated that the quantum gas magnifier allows for the measurement of density fluctuations – thermal and quantum. In our particular setup we encounter the technical difficulty of not having a phase lock for the lattice beams. Consequently, measurements for the same experimental parameters cannot be directly compared but a density envelope has to be constructed or fitted to identify the measurements which are drawn from the same probability distribution. Thus a phase lock for the lattice beams would be beneficial when fluctuations are to be analysed because in this case different shots can be directly compared without the need of envelope reconstruction. Another possibility would be a change to a box trap which would make the density envelope trivial. The capability to measure fluctuations and correlations is a major motivation for extending the quantum gas magnifier to the single atom sensitive regime via fluorescence imaging [22].

3.7. Conclusion

In conclusion we have explained the working principle of the quantum gas magnifier and have presented several experiments to benchmark and to demonstrate the capa-

bilities of the technique. We showed that 3D systems can be imaged, that flexible state preparation is possible, that features below a lattice constant can be resolved and that fluctuations can be analysed using the method. As such quantum gas magnification is a valuable new tool in the tool box of quantum simulation.

4. Formation of spontaneous density-wave patterns in DC driven lattices

As explained previously, the quantum gas magnifier is able to image 3D systems with 2D single site resolution, while not being a scanning technique. This advantage will be crucial in the following chapter: here we report on the observation of spontaneous pattern formation in a tilted triangular lattice with large bosonic filling and weak confinement perpendicular to the lattice making the system 3D. Since spontaneousness implies probabilism the pattern can only be observed in single shots, because it washes out when averaging over several experimental runs, as it would be the case for a scanning technique. In this chapter the experimental observation will be described and a theoretical modelling will be presented. The project is a collaboration with the theory group of Ludwig Mathey with Ludwig Mathey, Vijay Singh and Lukas Freystatzky being involved. The experiments have been carried out together with my fellow PhD students Marcel Kosch and Luca Asteria under the supervision of Klaus Sengstock and Christof Weitenberg.

Spontaneous symmetry breaking is a very fundamental and important concept in physics. It describes the phenomenon of a system probabilistically realizing one possible symmetry broken state among several equivalent ones. Symmetry broken means that the state is not invariant under a symmetry transformation commuting with the underlying Hamiltonian. Equivalent means that the possible states are connected via such a symmetry transformation and thus are degenerate. One example would be the ground state of a ferromagnet: All spins are aligned but they spontaneously choose in which direction all of them are pointing, breaking the global SU(2) symmetry of the Hamiltonian. At the same time all possible ground states are connected via such a global spin rotation. The most prominent example of spontaneous symmetry breaking probably is the one connected to the Higgs field [1, 2].

The examples described above are concerning spontaneous breaking of continuous symmetries. Yet, the phenomenon appears in the context of discrete symmetries as well. An example is the antiferromagnetic Ising spin chain. One can consider the Néel state which consists of all neighbouring spins being anti-aligned. This state breaks the discrete translational symmetry of the chain and has two possible realizations: A state with spin up on even sites and a state with spin up on odd sites.

Ultracold atom experiments have observed spontaneous symmetry breaking both

in continuous systems [15, 16] and lattice systems [11, 13, 14]. Using the quantum gas magnifier we can extend the observation of spontaneous symmetry breaking to real space pattern formation on the length scale of a lattice constant for systems with high bosonic filling.

4.1. Experimental protocol and observation

Let us first describe the experimental protocol that led to the observation of pattern formation. We start out by loading a BEC into the triangular lattice as described in chapter 2. The final lattice depth is $V_{\mathrm{lat}} = 1E_{\mathrm{r}}$ corresponding to a tunneling energy of $J = h \times 13\,\mathrm{Hz}$. The magnetic trap is ramped to a trapping frequency of $\omega_{\mathrm{sys}} = 2\pi \times 135\,\mathrm{Hz}$ characterized by dipole oscillations. The trapping frequency in z-direction is dominated by the lattice and is computed to be $\omega_z = 2\pi \times 30\,\mathrm{Hz}$ (appendix B). After the loading, the magnetic trap is suddenly shifted in x-direction, i.e., perpendicular to a primitive vector, by typically $d = 15\,\mathrm{\mu m} = 21a_{\mathrm{lat}}$ by switching off a magnetic offset field. The shift happens on a time scale of few tens of microseconds and the atoms therefore do not show any dynamics during the shift. Around their final position the potential can be approximated as a tilted lattice with a tilt of typically $F = h \times 2.3\,\mathrm{kHz/\mu m}$. After the quench we wait for different hold times. As expected for a strongly tilted system the atoms are localized on the slope [88, 89]. In addition
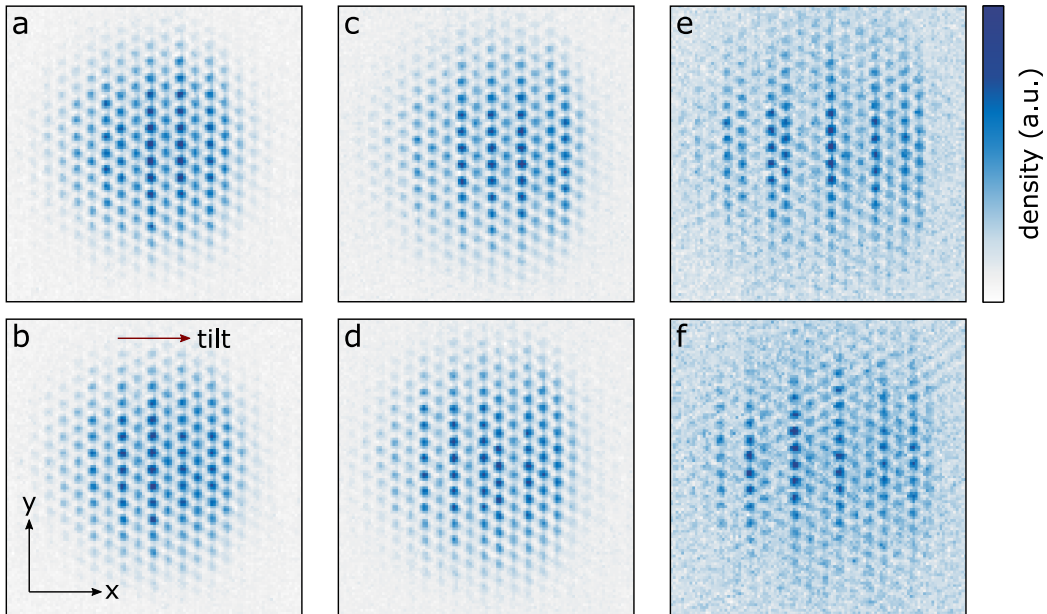
Figure 4.1.: Observation of spontaneous density-wave formation. Atomic density for a hold time after the quench of **(a,b)** 30 ms, **(c,d)** 60 ms and **(e,f)** 600 ms. All plots are obtained with a tilt corresponding to an energy offset of $\Delta = h \times 1.4\,\mathrm{kHz}$ between neighbouring columns. The colorscale is renormalized for each image individually.

a pattern slowly builds up as a function of hold time (Fig. 4.1). Initially, it consists predominantly of a density-wave with wavelength of two columns and wave-vector parallel to the tilt. Sometimes a wavelength of three columns occurs as well (Fig. 4.1a-d). For longer hold times the period of the pattern gets longer and approaches a value of ~ 3 (Fig. 4.1e,f). Additionally a slight movement of the center of mass towards the trap center can be detected. In the following we will discuss the pattern formations in more detail.

4.2. Theoretical description

As mentioned beforehand this project led to a collaboration with the theory group of Ludwig Mathey which implemented the models in this section. There are two approaches: One is starting from the Bose-Hubbard model with tilt and approximating it with an effective Hamiltonian for large tilt, the other is to do a numerical simulation of the full system using a c-field approximation which will be explained later in this section.

4.2.1. Effective model

First we want to present the analytical approach of a description via an effective model. We depart from the tilted Bose-Hubbard model (Fig. 4.2a)

$$\hat{H}_0 = -J \sum_{\langle jk \rangle} \left(\hat{b}_j^\dagger \hat{b}_k + \hat{b}_k^\dagger \hat{b}_j \right) + \frac{U}{2} \sum_j \hat{n}_j (\hat{n}_j - 1) + F \sum_j x_j \hat{n}_j, \qquad (4.1)$$

with the tunneling energy J, the interaction strength U and the tilt F. $\hat{b}_j^\dagger(\hat{b}_j)$ is the bosonic creation(annihilation) operator on site j, $\hat{n}_j = \hat{b}_j^\dagger \hat{b}_j$ is the particle number operator at site j, and x_j is the x-position of site j. $\sum_{\langle jk \rangle}$ indicates summation over nearest neighbours only. For the experimental parameters the energy offset between neighbouring columns $\Delta = F\Delta x = F\sqrt{3}/2a_{\mathrm{lat}}$, where Δx is the distance between two neighbouring columns, is the largest energy in the bare model. Here, a column is a chain of sites in y-direction. Thus the effective description should model the case of large tilt. To this end it will turn out beneficial to transform the Hamiltonian $\hat{H}_0$ to the interaction picture with respect to $\hat{H}_F = F \sum_j x_j \hat{n}_j$ resulting in

$$\begin{aligned}
\hat{H}_{\mathrm{I}} &= e^{i\frac{\hat{H}_F t}{\hbar}} \hat{H}_0 e^{-i\frac{\hat{H}_F t}{\hbar}} \\
&= -J \sum_{\langle jk \rangle_y} \left(\hat{b}_j^\dagger \hat{b}_k + \hat{b}_k^\dagger \hat{b}_j \right) - J \sum_{\langle jk \rangle_{x+}} \hat{b}_j^\dagger \hat{b}_k e^{-i\frac{\Delta t}{\hbar}} - J \sum_{\langle jk \rangle_{x-}} \hat{b}_j^\dagger \hat{b}_k e^{i\frac{\Delta t}{\hbar}} + \frac{U}{2} \sum_j \hat{n}_j (\hat{n}_j - 1).
\end{aligned}$$
$$(4.2)$$

Here, $\sum_{\langle jk \rangle_y}$ denotes summation over the nearest neighbours in y-direction, $\sum_{\langle jk \rangle_{x+}}$ summation over the nearest neighbours in x-direction with site k having higher po-
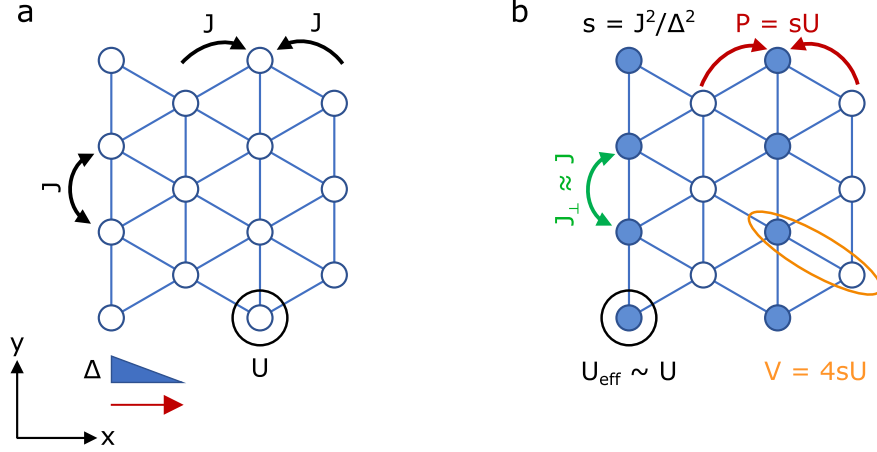
Figure 4.2.: Bose-Hubbard model and effective model. **(a)**, sketch of the Bose-Hubbard model on the triangular lattice with tilt in x-direction. It is characterized by single particle tunneling J, on-site interaction U and an energy offset Δ between neighbouring columns resulting from the tilt. **(b)**, sketch of the emergent effective Hamiltonian for $\Delta/J \gg 1$. The model contains correlated pair tunneling P where one particle hops up the tilt and another hops down, and a nearest neighbour interaction V as new terms. Single particle tunneling in x-direction does not exist in the effective description, the single particle tunneling along the y-direction $J_\perp$ and the on-site interaction U_{eff} are only slightly modified. Adapted from [90].

tential energy, $\sum_{\langle jk \rangle_{x-}}$ in x-direction with site k having lower potential energy. Conveniently, this Hamiltonian is time periodic with a fast frequency equal to Δ/h and therefore a special form of the Magnus expansion can be applied [91–93] resulting in the desired effective description. We separate the effective Hamiltonian into three parts that will be explained below:

$$\hat{H}_{\text{eff}} = \hat{H}_P + \hat{H}_{J_\perp} + \hat{H}_{U,\text{eff}}, \tag{4.3}$$

with

$$\hat{H}_P = -sU \sum_{\langle jkl \rangle_\times} \left(\hat{b}_j^\dagger \hat{b}_j^\dagger \hat{b}_k \hat{b}_l + \hat{b}_l^\dagger \hat{b}_k^\dagger \hat{b}_j \hat{b}_j \right), \tag{4.4}$$

$$\hat{H}_{J_\perp} = -\sum_{\langle jk \rangle_y} \left(J\hat{b}_j^\dagger \hat{b}_k + sU\hat{b}_j^\dagger \hat{n}_j \hat{b}_k + sU\hat{b}_j^\dagger \hat{n}_k \hat{b}_k + \text{h.c.} \right)$$
$$+ 2sU \sum_{\langle jkl \rangle_\triangle} \left(\hat{b}_j^\dagger \hat{n}_l \hat{b}_k + \hat{b}_k^\dagger \hat{n}_l \hat{b}_j \right), \tag{4.5}$$

$$\hat{H}_{U,\text{eff}} = \left(\frac{U}{2} - 4sU \right) \sum_j \hat{n}_j(\hat{n}_j - 1) + 4sU \sum_{\langle jk \rangle_x} \hat{n}_j \hat{n}_k, \tag{4.6}$$

where $s = J^2/\Delta^2$. $\sum_{\langle jkl \rangle_\times}$ denotes summation over all pairs of bonds sharing a site and with one bond up and one down the tilt, and $\sum_{\langle jkl \rangle_\triangle}$ denotes summation over triangular plaquettes such that j and k are nearest neighbors in y-direction.
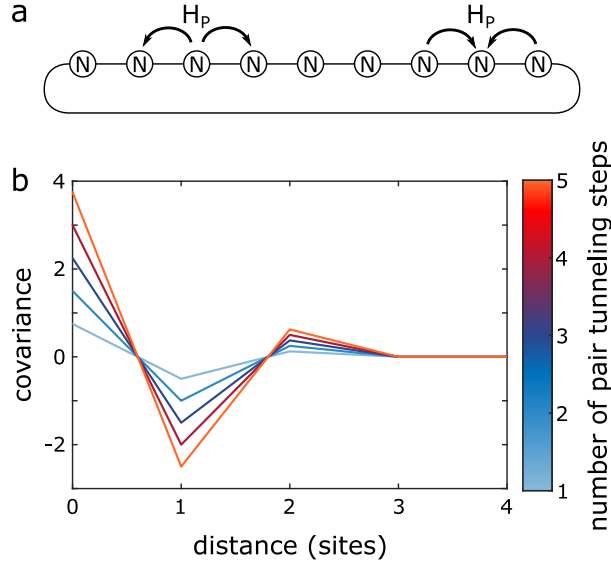
Figure 4.3.: States coupled by pair tunneling. **(a)**, sketch of the model. The initial state consists of a chain of 9 sites with equal and large filling N. All states that are accessible via a certain number of pair hopping processes are considered. The two elementary pair tunneling processes are illustrated at exemplary sites. **(b)**, mean covariance of the accessible states as a function of distance between the sites color-coded for different numbers of pair tunneling steps. Adapted from [90].

This effective Hamiltonian has a very interesting form (Fig. 4.2b): First of all, there is no single particle tunneling in the tilt direction any more. The only tunneling term in this direction is the correlated pair tunneling term $\hat{H}_P$ which simultaneously moves two particles from or to a single site: one particle moves one lattice site up the tilt and one other particle one lattice site down the tilt such that the potential energy and center of mass are conserved by this process. Note that this process is only possible due to interactions since these shift the intermediate states of the process. Without this shift the two processes of moving one or the other particle first would cancel which is reflected in the proportionality to U. Another new term, a nearest neighbour interaction, given by the second term in $\hat{H}_{U,\text{eff}}$ emerges as well as a result of the expansion. Finally there are also two terms that are only slightly changed from the tilted Bose-Hubbard Hamiltonian. For the tunneling perpendicular to the tilt $\hat{H}_{J_\perp}$ only small corrections proportional to $s \ll 1$ arise. The same argument holds for the on-site interaction represented by the first term of $\hat{H}_{U,\text{eff}}$ which changes only slightly as well compared to the bare on-site interaction. Due to the long-range interaction and the correlated hopping the effective Hamiltonian belongs to the family of extended Hubbard models [94]. These models exhibit exotic ground states such as charge density waves or supersolids. Note however that we do not prepare the ground state in the experiment but consider quench dynamics.

For the density wave formation it is particularly interesting to consider the dynam-

ical term, the pair tunneling $\hat{H}_P$. It couples an initially homogeneously populated state to states with patterns. To illustrate this we analyse the states that are coupled to a homogeneous initial state via repeated application of the pair tunneling operator $\hat{H}_P$ as described in the following. As a toy model, we consider an initial Fock state on a 1D chain of $N_{\text{sites}} = 9$ lattice sites each populated with N atoms using periodic boundary conditions (Fig. 4.3a). We apply the pair tunneling operator to this state once considering all possible outcomes, i.e., we obtain the state where two particles leave the first site, the state where two particles hop to the first site, the state where two particles leave the second site and so on, resulting in a number of accessible states which is double the number of sites. For each of these states the procedure can be repeated leading to a huge tree of coupled states. For every state we can compute the covariance of the deviations from the initial homogeneous filling δN_i as

$$\text{cov}(d) = \frac{1}{N_{\text{sites}} - 1} \sum_{i=1}^{N_{\text{sites}}} \delta N_i \delta N_{i+d}, \qquad (4.7)$$

with periodic boundary conditions, i.e., $\delta N_{i+N_{\text{sites}}} = \delta N_i$. As long as N is large compared to δN_i the couplings have almost the same value. We can approximate them to be equal allowing for averaging the covariances of all states corresponding to the same number of pair tunneling events. This average is plotted in Fig. 4.3b and shows finite-range staggered correlations that grow with the number of pair tunneling events. This is in qualitative agreement with the period two pattern with domain walls observed in the experiment and therefore motivates why pair tunneling can create such a pattern. More elaborate theoretical treatment will be given in the sections below.

4.2.2. Perturbative expansion

Another analytical approach that is similar to the effective model is a perturbative expansion of the density-density correlations. Here as well we consider a 1D system simplifying the Hamiltonian in the interaction picture (4.2) to

$$\hat{H}_{\text{I}} = -J \sum_j \left(\hat{b}_j^\dagger \hat{b}_{j+1} e^{-i\frac{\Delta}{\hbar}t} + \hat{b}_{j+1}^\dagger \hat{b}_j e^{i\frac{\Delta}{\hbar}t} \right) + \frac{U}{2} \sum_j \hat{n}_j (\hat{n}_j - 1). \qquad (4.8)$$

The density-density correlation operator $\hat{n}_i \hat{n}_j$ expanded to second order is given by

$$(\hat{n}_i \hat{n}_j)(t) = \hat{n}_i \hat{n}_j + \frac{i}{\hbar} \int_0^t \text{d}t_1 [\hat{H}_{\text{I}}(t_1), \hat{n}_i \hat{n}_j] - \frac{1}{\hbar^2} \int_0^t \text{d}t_1 \int_0^{t_1} \text{d}t_2 [\hat{H}_{\text{I}}(t_2), [\hat{H}_{\text{I}}(t_1), \hat{n}_i \hat{n}_j]].$$
$$(4.9)$$

The density-density correlations are obtained as the expectation value of the above expression. We are particularly interested in the spectrum of these correlations which

can be computed to be

$$\langle \hat{\rho}_k \hat{\rho}_k \rangle = \frac{1}{N_{\text{sites}}} \sum_{i,R} \exp(ikR) \overline{\langle \hat{n}_i \hat{n}_{i+R} \rangle} \tag{4.10}$$

$$= 4 s n_0^2 \left(1 - \cos(k a_{\text{lat}}) \right) \left(2 - e^{-\frac{2a}{r_0}} - e^{-\frac{4a}{r_0}} \right). \tag{4.11}$$

The averaging denoted by overline is a temporal average which vanishes for expressions oscillating with Δ/h or multiples of it. In the computation the approximation

$$\langle \hat{b}_i^\dagger \hat{b}_{i'} \hat{b}_j^\dagger \hat{b}_{j'} \rangle \approx \frac{g(|i-i'|)g(|j-j'|)g(|i-j'|)g(|i'-j|)}{g(|i-j|)g(|i'-j'|)}, \tag{4.12}$$

was used, where $g(i) = \langle \hat{b}_0^\dagger \hat{b}_i \rangle \approx n_0 \exp(-|i|/r_0)$. n_0 is the equilibrium particle number and r_0 is the phase correlation length.

The correlations predicted by the perturbative expansion are of period two since the spectrum is peaked at $k a_{\text{lat}}/(2\pi) = 1/2$ and of finite range since the cosine shaped peak has a finite width. This is in agreement with the experimental observation.

4.2.3. c-field simulations

A complementary approach to the analytic modelling of the system is a so-called classical field (c-field) simulation [95]. Here we also start from the Bose-Hubbard model, but we explicitly consider the third dimension and instead of a homogeneous tilt we include the full harmonic trap:

$$\hat{H} = -\sum_{\langle jk \rangle} J_{jk} \left(\hat{b}_j^\dagger \hat{b}_k + \hat{b}_k^\dagger \hat{b}_j \right) + \frac{\tilde{U}}{2} \sum_j \hat{n}_j (\hat{n}_j - 1) + \sum_j V_j \hat{n}_j. \tag{4.13}$$

Here, $V_j = m[\omega_{\text{sys}}^2(x_j^2 + y_j^2) + \omega_z z_j^2]/2$ is the external potential at site j. Note that for the purpose of the simulation we discretized the z-direction as well using a discretization length of $l_z = 0.4\,\mu\text{m}$ resulting in a coupling in z-direction of $J_z = h^2/(8\pi^2 m l_z^2) = 27.9 J$. Hence the tunneling energy J_{jk} equals J for tunneling in plane and the much larger value J_z for tunneling in z-direction, supporting the continuum limit in z-direction. The discretized z-direction also changes the way interactions are taken into account. Instead of considering the total number of atoms per tube to compute the interaction energy in the same tube, we now take the 3D approach and compute the interaction energy for each discretization volume by the number of particles in the same small volume. The interaction strength is given by $\tilde{U} = g/(2\pi a_{\text{ho}}^2 l_z) = 17.6 J$ where a_{ho} is the on-site oscillator length deduced from the experimental lattice depth (appendix B).

The approximation of the c-field method consists of replacing the operators $\hat{b}_j (\hat{b}_j^\dagger)$ by complex numbers $\psi_j (\bar{\psi}_j)$ which is justified by assuming large occupations implying small relative fluctuations. A finite but low temperature can be incorporated as long
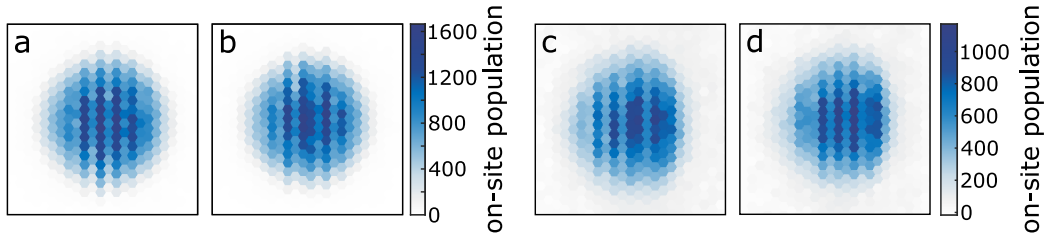
Figure 4.4.: Example results of c-field simulations and comparison to experimental results. **(a,b)**, on-site populations resulting from c-field simulations with the same parameters as in Fig. 4.1c,d. The temperature is $T = 30J/k_B$. **(c,d)**, images Fig. 4.1c,d in on-site population representation. Due to the probabilistic nature of the pattern formation only qualitative agreement between experiment and theory is expected on the level of single shots.

as the mode population stays high. To do so, an initial state is drawn from a thermal ensemble having the desired temperature. This initial state is then propagated in time according to the discrete non-linear Schrödinger equation

$$i\hbar \frac{\partial}{\partial t} \psi_j = - \sum_{\langle jk \rangle} J_{jk} \psi_k + \frac{\tilde{U}}{2} |\psi_j|^2 \psi_j + V_j \psi_j. \tag{4.14}$$

The c-field approach is very close to the actual experimental conditions and reproduces the pattern formation in the experiment as can be seen, e.g., in Fig. 4.4. In particular it also allows for dynamics in the direction perpendicular to the lattice such as loss of phase coherence. This is not possible to model in the effective Hamiltonian approach which does not take excitations in this direction into account. The disadvantage of the c-field however is that, as for all numerical methods, it is harder to extract the underlying mechanisms that drive the dynamics. It is therefore complementary to the analytical approach which is able to identify an effective description including pair tunneling terms.

4.3. Spontaneous symmetry breaking and domain formation

After having introduced the theoretical framework we want to take a step back and investigate the experimentally observed pattern in more detail. In particular we want to demonstrate the spontaneous nature of the symmetry breaking. For a discrete pattern of period two there are two possible positions. If the symmetry breaking is spontaneous, both should occur with equal probability. In this framework the local occurrence of period three can be interpreted as domain walls between the two possible realizations of the period two pattern. The different positions can be made visible by element-wise multiplication with a reference pattern as will be explained

in this section. We perform the analysis for a hold time after the quench of $60\,\mathrm{ms}$ and a shift of $d = 15\,\mu\mathrm{m}$ leading to an energy offset of $\Delta = h \times 1.4\,\mathrm{kHz}$ between neighbouring columns.

4.3.1. Domain identification and statistics

The question which position of the pattern is realized is essentially equivalent to the analysis of domains since the domains are defined by attributing the lattice sites to one of the two possible realizations of density-wave position. The domains of the pattern can be made visible in the following way (Fig. 4.5a): first the residues, i.e., the deviation from the density envelope, need to be computed for the image under consideration. To obtain the envelope all images corresponding to the same parameters are averaged washing out the density-wave. From this mean image on-site populations are computed assuming lattice sites at the same position as in the image for which the residues should be calculated. The on-site populations corresponding to the mean image are then subtracted from the ones corresponding to the single image. In the residues the pattern is visible as an oscillation around zero. This oscillation can be rectified by element-wise multiplication with a reference pattern of perfectly alternating sign. We call the result staggered residues. The staggered residues have the same sign for domains of the same density-wave position and opposite sign for domains of different position.

In Fig. 4.5b-i a few example shots in domain representation are shown. It can be seen that most of the time the pattern consists of one or two domains. In particular we observe that the pattern formation is probabilistic because we obtain a different result for every shot even though the experimental parameters are identical. Since the position of the lattice relative to the magnetic trap changes for different runs (appendix C) we post-selected the images in order to have an identical origin along the tilt direction, ensuring that the change in pattern is not caused by this.

In a further analysis we can quantify to which extent both density-wave positions are equivalent. To this end we define a region of interest of radius three sites around the center (Fig. 4.5b) and draw a histogram of all staggered residues within this region (Fig. 4.5j). We obtain a symmetric, double peaked distribution which again confirms the spontaneous nature of the symmetry breaking and also shows that both realizations of density wave have the same probability of occurrence. Here as well a post-selection with respect to the x-coordinate of the lattice origin is possible (Fig.4.5k). The individual histograms are more noisy, having only about 1/5 of the data but still all of them show a double peak structure.

The same analysis can be performed on results from a c-field simulation with the experimental parameters, and a temperature of $T = 250J/k_\mathrm{B}$ which is not known for the experiment. The histogram based on the theoretical images—depicted by the dashed line in Fig. 4.5j—is in good agreement with the one based on the experimental images.
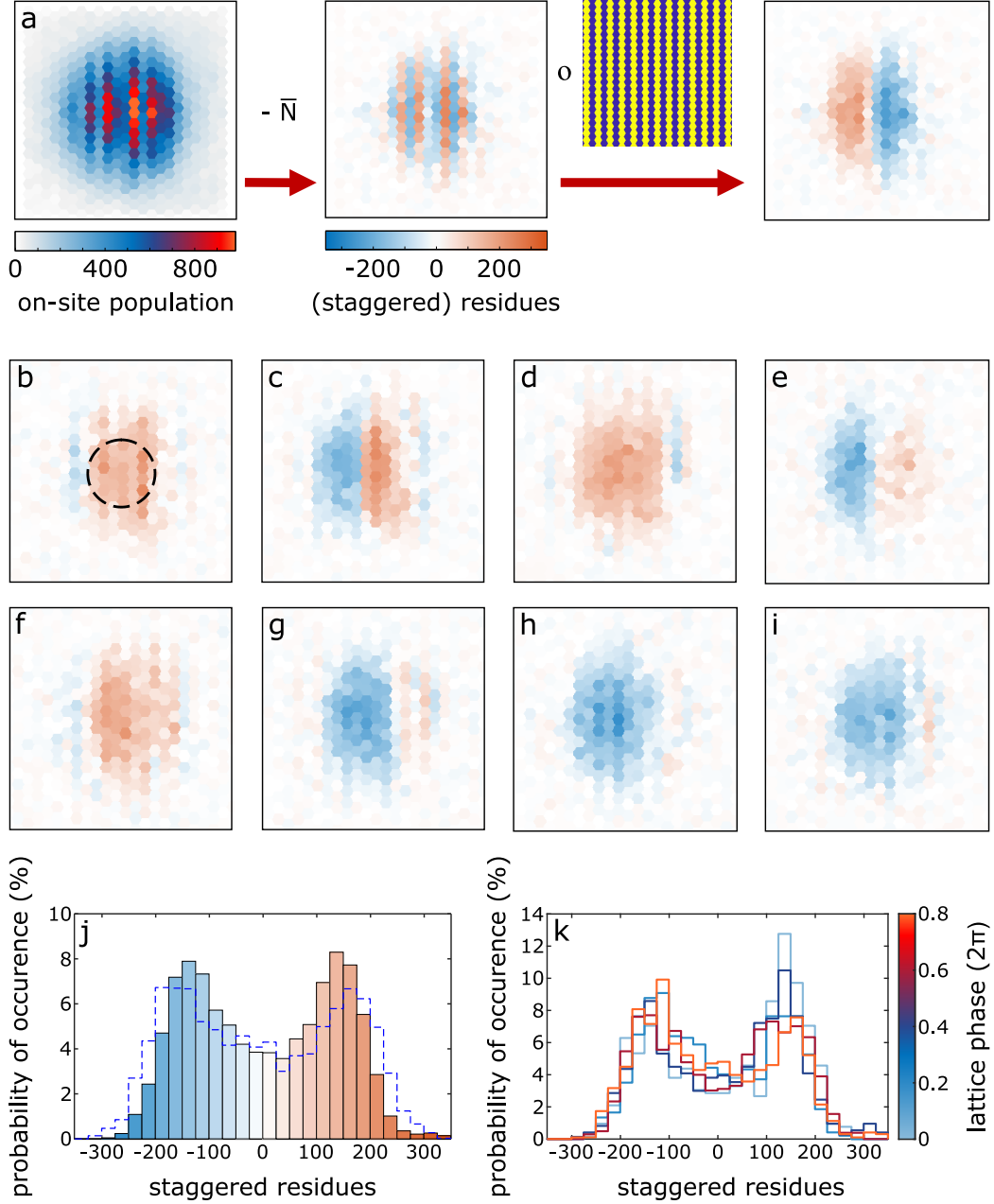
Figure 4.5.: Domain analysis. **(a)**, Illustration of the procedure to quantify the domains. First the mean population is subtracted. The residues are then multiplied by a reference pattern of fixed position resulting in staggered residues which are positive when in phase with the reference and negative when out of phase. **(b-i)**, example shots obtained for an energy offset of $\Delta = h \times 1.4\,\text{kHz}$ and a hold time of $60\,\text{ms}$. The images result from a post selection of the x-component of the origin. **(j)**, histogram of the staggered residues of the sites within the region of interest shown in (b) for about 130 experimental runs. The dashed line corresponds to the analysis of c-field simulation results with the same analysis as for the experimental data. The temperature used in the numerics is $T = 250J/k_\text{B}$. **(k)**, statistics of the same data as in (j) but now with post-selection on the x-position of the lattice. The color corresponds to the different positions. Adapted from [90].

4.3.2. Location of domain walls

With the identification of the domains we can also locate the domain walls between them. This distribution is also very interesting in the context of spontaneous symmetry breaking since in this case there should be no preferred position for the domain walls. We identify a domain wall by a sign change in the staggered residues. As can be seen in Fig. 4.5b-i, these sign changes almost exclusively occur in x-direction. We can therefore sum the staggered residues in y-direction without losing information. In this 1D object it is straightforward to locate sign changes for every shot, see Fig. 4.6a-c for an example. After identifying the domain walls in the single shots we average the occurrences for the same parameters including post selection on the lattice origin in x-direction to obtain the probability of encountering a domain wall as a function of position (Fig. 4.6d).

It can be seen that in the central region the probability to have a domain wall is $\sim 10\% - 20\%$. In the direction towards the trap center there is a slight increase which might be connected to the pinning of the density-wave which will be presented later. Outside of the region featuring a pattern (see gray profile in Fig. 4.6b for reference)
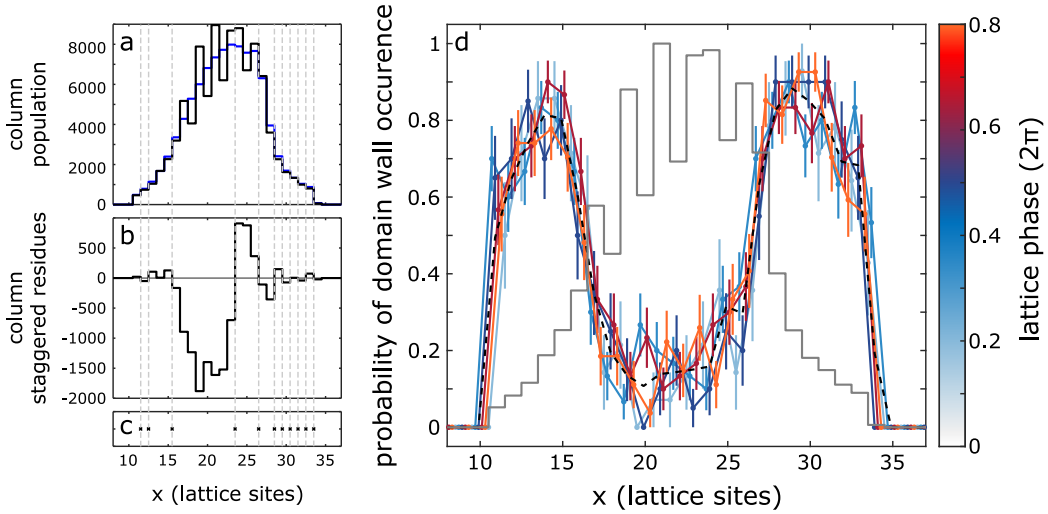
Figure 4.6.: Domain wall locations. **(a-c)**, illustration of the computation of the domain wall location. (a), example column populations, i.e., on-site populations integrated along y (black line) and the corresponding average populations (blue line). (b), column staggered residues for the same experimental run. (c), identified domain wall locations. Crosses mark a domain wall at the respective position. For every cross there is a dashed gray line indicating where the domain wall is located in the other plots. The locations are identified by the sign changes in (b). **(d)**, probability of domain wall occurence as a function of x (circles). The error bars denote the standard deviation of the mean, the color encodes the x-position of the lattice relative to the magnetic trap. The dashed line is the mean over all lattice positions. (a) is repeated in the background for reference.

the probability of finding a sign change is extremely high since the staggered residues are close to zero here. Actually, due to imperfections in the envelope calculation it even rises above the value of 1/2 expected for uncorrelated noise. This can be seen in Fig. 4.6b as well: at the edge of the cloud the staggered residues change sign every site instead of randomly. This happens when the envelope is slightly above or below the single shot profile because the staggering maps this to an alternating pattern. Eventually the domain wall probability drops to zero corresponding to sites that are outside the image and therefore zero by definition making sign changes impossible. The approximately homogeneous spatial distribution of the domain walls in the region where the pattern is observed confirms the spontaneous nature of the symmetry breaking.

4.4. Dynamical evolution

So far we have discussed the patterns that can be observed after 60 ms of hold time, but, of course, the pattern formation is a dynamical process. In this section we want to investigate the dynamical evolution of the density-wave.

First we look at the spatial spectral properties of the patterns, or, more precise, of their sum perpendicular to the density-wave vector $n_x(x) = \sum_y n(x,y)$ since the patterns are almost always invariant perpendicular to the tilt. As a measure, we consider the power spectral density (PSD) normalized to the total atom number

$$|n_k|^2 = \frac{|\mathcal{F}\left(n_x(x)\right)(k)|^2}{N_{\text{tot}}} \tag{4.15}$$

which captures the spectrum of the density-density correlations. It is plotted for different hold times in Fig. 4.7a. It can be seen that for the early times considered in the previous section the PSD is peaked at $k\tilde{a}/(2\pi) = \pm 1/2$ with $\tilde{a} = \sqrt{3}/2a_{\text{lat}}$ being the separation between two columns. This corresponds to a pattern of period two. For longer hold times the peak moves to smaller wave vectors and saturates at $k\tilde{a}/(2\pi) \sim \pm 1/3$ corresponding to a pattern of period three. The peak always has a finite width indicating that the periodicity of the pattern is not perfect in every shot, corresponding to the presence of domain walls.

In order to compare to the results of the c-field simulation, we define a measure that is independent of the precise spectral properties of the pattern. We name this measure density-wave contrast c and define it as

$$c = \frac{\int_{1/5}^{1/2} |n_k|^2 \, \mathrm{d}\tilde{k}}{\int_0^{1/2} |n_k|^2 \, \mathrm{d}\tilde{k}}, \tag{4.16}$$

with $\tilde{k} = k\tilde{a}/(2\pi)$. The density-wave contrast is plotted in Fig. 4.7h,i for different tilt strengths. It grows within the first ~ 200 ms and then decays only very slowly. Actually, at the longest observation time of 1.6 s it is still on a comparable value to
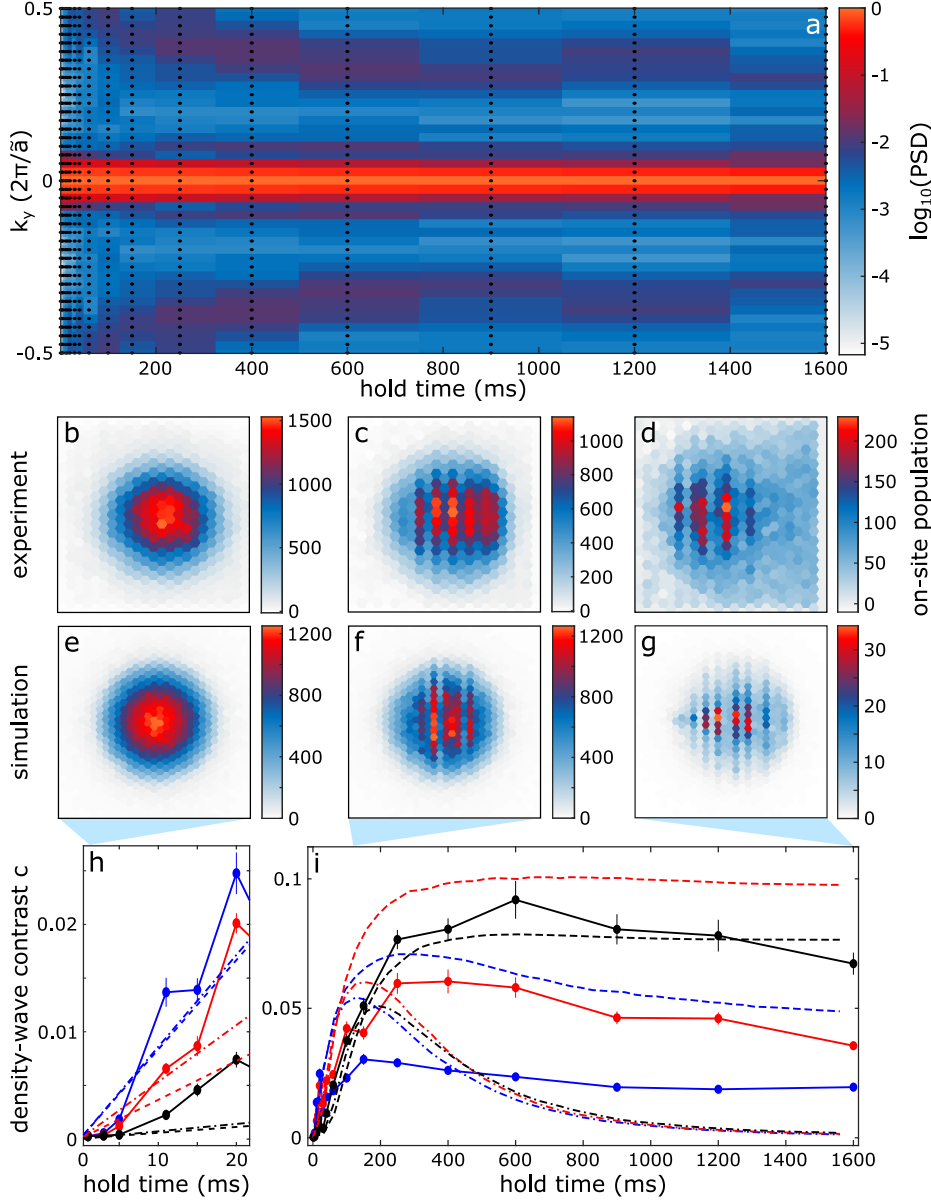
Figure 4.7.: Formation and decay of the density-wave. **(a)**, power spectral density as a function of hold time and wave vector, normalized to the total atom number as defined in the main text. The circles indicate the parameters where data was taken. The dashed line corresponds to $k_y \tilde{a}/(2\pi) = 1/5$ which is the minimal wave vector taken into account for the computation of the density-wave contrast defined in the main text. **(b-d)**, experimental example images of on-site populations for an energy offset $\Delta = h \times 1.4\,\text{kHz}$ and hold times of (b) $1\,\text{ms}$, (c) $60\,\text{ms}$ and (d) $1600\,\text{ms}$. **(e-g)**, example on-site populations resulting from a c-field simulation with the same parameters and a temperature of $T = 100 J/k_\text{B}$. **(h,i)**, density-wave contrast as a function of hold time for different tilts. The energy offset is color-coded as $\Delta = 1.1\,\text{kHz}$ (blue), $1.4\,\text{kHz}$ (red), $1.7\,\text{kHz}$ (black). The circles correspond to experimental data with errorbars showing the standard deviation of the mean. The dotted-dashed lines correspond to a c-field simulation without atom loss, the dashed lines to a simulation with atom loss. (h) is a zoom into (i). Adapted from [90].
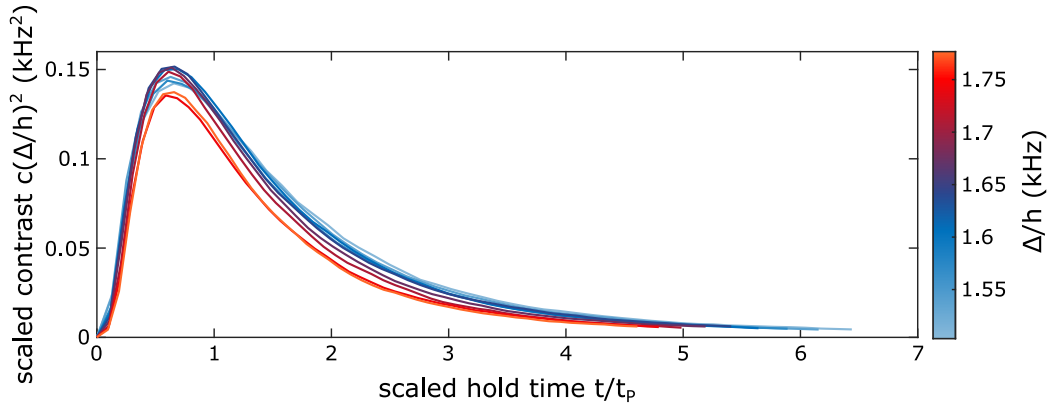
Figure 4.8.: Scaling of the c-field dynamics. Scaled density-wave contrast $c(\Delta/h)^2$ as a function of the rescaled time t/t_P for different tilt strengths as indicated by the color. Adapted from [90].

the maximum value and it is not clear if it would actually decay to zero for longer hold times. Note that this observation of long lifetime is different from those of recent experiments in tilted lattices [96, 97] where the lifetime of a prepared pattern was investigated instead of the lifetime of an emerging pattern as done here.

The rise time of the density wave contrast can be motivated by the effective Hamiltonian (4.3-4.6): in a Rabi-oscillation paradigm, the dynamical term, the pair tunneling term (4.4), defines a time scale $t_P = h/(4\Omega_P)$ for reaching the maximum with pair tunnel coupling $\Omega_P = 4NsU$ where the factor 4 was added for the 4 possible pairs of bonds sharing a site and the factor of peak on-site population N takes into account bosonic enhancement of the process. Using $N = 1500$ and $U = 2.3\,\text{Hz}$ (appendix B) we obtain $\sim 200\,\text{ms}$. The time scale t_P is also confirmed by a rescaling of c-field simulations for different tilts with t_P in combination with the amplitude rescaling expected from (4.11) (Fig. 4.8). Note that we believe for the experiment and know for the simulation that excitations in the z-direction happen after the quench. This reduces the bosonic enhancement and hence t_P should be interpreted as a lower bound on the time scale.

The long lifetime can be understood with the help of the c-field simulations as well. The dotted-dashed lines in Fig. 4.7h,i show the results of a simulation with conserved atom number for different tilts. The initial build up of the density-wave is captured but after reaching the maximum contrast the density-wave decays again. However, as can be seen from the example experimental shots in Fig. 4.7b-d, the atom number in the experiment decays. This is mainly due to the metastability of the atoms at the slope of the magnetic trap. For long hold times atoms decay back to the trap center, possibly due to Landau-Zener transitions into higher bands. If we model this by single particle loss in the simulations the density-wave turns out to be long lived as well as can be seen from the dashed lines in Fig. 4.7h,i. This is due to the density dependence of the pair tunneling term in the effective Hamiltonian. If
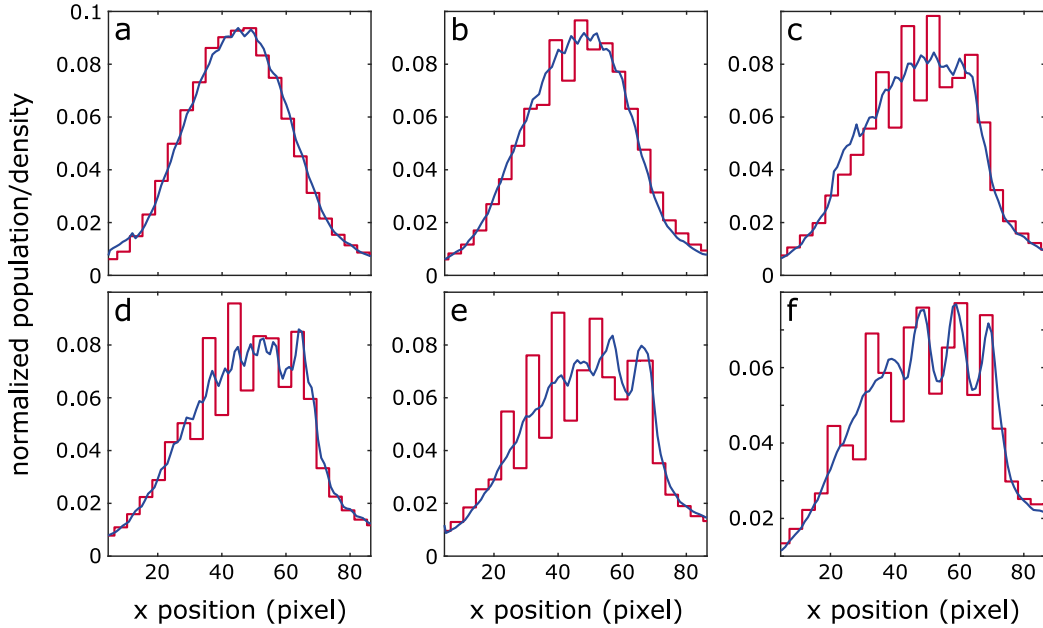
Figure 4.9.: Transition from spontaneous to pinned patterns. **(a-f)**, normalized mean density (blue lines) and normalized column populations (red lines) for hold times after the quench of (a) 5 ms, (b) 20 ms, (c) 60 ms, (d) 100 ms, (e) 150 ms, (f) 400 ms. Adapted from [90].

the density decreases the pair tunneling gets weaker and the dynamics therefore gets frozen. Besides the interaction dependence of the pair tunneling term, this is another way of seeing that the observed dynamics is interaction driven.

When investigating the dynamics of the column populations in detail there is an interesting observation to be made. Up to a hold time of ~ 60 ms the average density is a featureless profile (blue lines in Fig. 4.9) whereas single realizations (red lines in Fig. 4.9) show a pattern, reflecting the spontaneous nature of the pattern formation. Surprisingly for hold times of ~ 100 ms and longer the average density shows a pattern as well, implying an evolution from a spontaneous pattern to a pinned pattern. This might be due to an interplay between the slow single particle tunneling and the terms of the effective Hamiltonian. The single particle tunneling is able to move the center of mass of the system. However, for particles at the energetically lower end of the cloud hopping is strongly off-resonant due to the interaction energy loss when tunneling against the slope of the density leading to an accumulation of particles at this end. This phenomenon is known as self-trapping and was observed for atoms in a 1D lattice after release of the confinement [21]. The fact that the atoms do not only accumulate at the lower end but form a number of maxima increasing with time could be due to the exotic terms of the effective Hamiltonian. The precise explanation of the pinning dynamics is left for future work.

4.5. Influence of transverse tunneling

In another set of experiments we investigate the role of transverse tunneling, i.e. tunneling perpendicular to the tilt. To do so we change the direction of the shift by 90° hence shifting parallel to a primitive vector of the lattice. For easier discussion we rotate the images afterwards in order to have the tilt pointing to the right as for the shift direction discussed so far. At first glance the tight binding model for the two situations is very different but a closer look reveals that essentially only the transverse tunneling is suppressed. This can be seen from Fig. 4.10a,b and will be explained in the following. There are two directions marked in the figure: the direction along the dashed line and the direction along the dotted line. The tunneling exactly parallel to the tilt in Fig. 4.10b can be neglected because its energy offset is twice the one along the dashed line making it four times weaker. For the direction along the dashed line the energy offset Δ per bond decreases when just rotating the shift direction but leaving its magnitude unchanged. We therefore increase the shift distance in order to compensate this which ensures the same energy offset among neighbouring columns in both situations. The direction along the dotted line is along resonant bonds in the original orientation and hence there is strong coupling within the columns. For the rotated situation there are no bonds along the dotted line and therefore all coupling in this direction must come from second order or long range tunneling. Thus, indeed, the tight binding model of the original and the rotated experiment mainly differ in the strength of transverse tunneling when adjusting the tilt F in such a way to obtain the same energy offset Δ between neighbouring columns.

Note that a density-wave with wave vector parallel to the tilt—as illustrated by the blue and grey stripes in Fig. 4.10a,b—gives the visual impression of a density-wave with wave vector perpendicular to the tilt due to the distance between next nearest neighboured columns being smaller than the distance between two neighbouring sites within a column. This impression is reinforced when using the standard representation for the on-site populations by colored hexagons because these touch the next nearest column but not the nearest neighbour within the column.

Fig. 4.10d shows two example images without transverse tunneling. Clearly, the patterns are much more irregular than in the case with transverse tunneling. We quantify this by computing the density-density correlations of the patterns (Fig. 4.10e,f). To this end we compute the residues as in section 4.3 and subsequently evaluate their covariance

$$\text{cov}_{jk} = \frac{1}{N-1} \sum_{i=1}^{N} \delta N_j^{(i)} \delta N_k^{(i)}. \tag{4.17}$$

$\delta N_j^{(i)}$ is the residue at site j for shot i and N is the number of shots with the same parameters. In a next step the covariances of pairs having the same or exactly opposite distance vector are averaged. Only pairs with both sites within 3 sites of the center of the cloud are taken into account. In this way a covariance as a function of
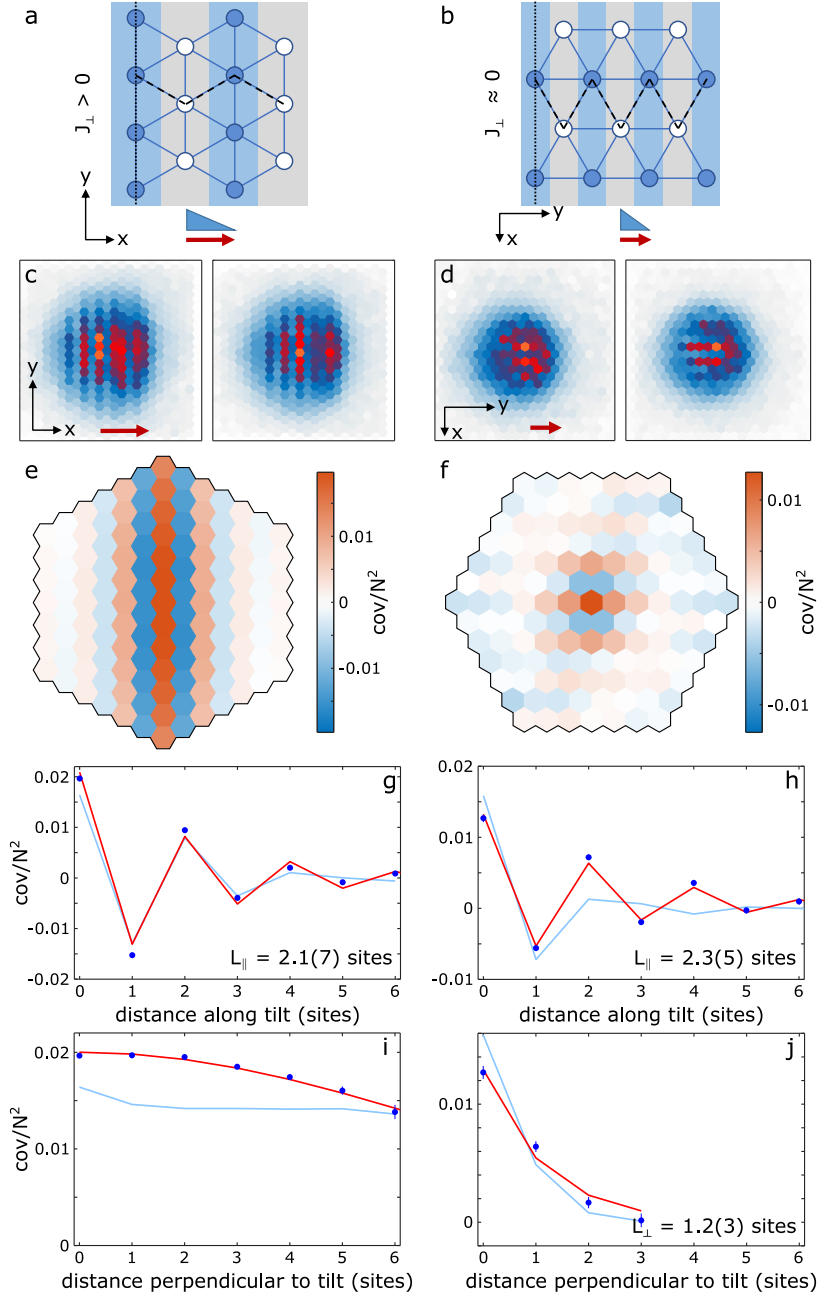
Figure 4.10.: Influence of transverse tunneling. **(a,b)**, sketches for the two experimental situations. In both a direction perpendicular to the tilt (dotted lines) and parallel to the tilt (dashed lines) are defined. The triangle and the red arrow stand for the tilt strength which is adapted such that the energy offset between neighbouring columns is equal in both cases. The gray and blue rectangles as well as the color of the sites illustrate how a period two density-wave with wave vector parallel to the tilt would appear. **(c,d)**, example images for experiments (c) with strong transverse tunneling, (d) with weak transverse tunneling. **(e,f)**, density-density correlations (e) for the situation with strong transverse tunneling, (f) with weak tunneling. **(g)**, cut through (e) along the dashed direction in (a) and through the origin. **(h)**, cut through (f) along the dashed direction in (b) and through the origin. **(i)**, cut through (e) along the dotted direction in (a) and through the origin. **(j)**, cut through (f) along the dotted direction in (b) and through the origin. Symbols show the cuts, red lines the fits described in the main text, blue lines the result from c-field simulation. Adapted from [90].

distance vector is obtained. Finally the covariance is normalized to the mean instantaneous maximal on-site population squared to obtain the quantity which is plotted in Fig. 4.10e-j. For the computation of the uncertainty of the covariance see appendix D. Clearly, the correlations are more pronounced in the case with transverse tunneling but also clearly there are correlations in the patterns emerging without transverse tunneling. In fact, when plotting the correlations along the direction of the dashed line the result is very similar (blue circles in Fig. 4.10g,h) whereas in the direction of the dotted line the difference is striking (blue circles in Fig. 4.10i,j). The same analysis can be performed on the results from the c-field simulation, yielding good agreement (light blue lines in Fig. 4.10g-j).

In order to associate a length scale to the correlation functions we introduce heuristic fit functions. The alternating correlations in direction of the tilt are fitted using a staggered exponential decay

$$c_i = c_0(-1)^i e^{-\frac{i}{L_\parallel}}. \tag{4.18}$$

For the case of weak transverse tunneling we added a small background Gaussian in order to account for artefacts originating from small displacements of the trap between shots. The correlations perpendicular to the tilt in the case with strong transverse tunneling are fitted using a Gaussian

$$c_i = c_0 e^{-\frac{i^2}{L_\perp^2}}, \tag{4.19}$$

and the correlations perpendicular to the tilt in the case of weak transverse tunneling are fitted using an exponential decay

$$c_i = c_0 e^{-\frac{i}{L_\perp}}. \tag{4.20}$$

i denotes the distance measured in sites and c_0, $L_\parallel$ and $L_\perp$ are the fit parameters. The fits result in $L_\parallel = 2.1(7)(L_\parallel = 2.3(5))$ sites parallel to the tilt and long range order ($L_\perp = 1.2(3)$ sites) perpendicular to the tilt for the case with strong(weak) transverse tunneling.

This demonstrates that transverse tunneling is essential for the correlations perpendicular to the tilt, i.e., it is required to obtain patterns consisting of long stripes. The antiferromagnetic correlations in direction of the tilt on the other hand seem to be independent of the tunneling in the perpendicular direction. Thus the transverse tunneling seems to lock the choice of realization of the different zig-zag lines in the sample resulting in long stripes perpendicular to the tilt. Reducing the transverse tunneling leads to the zig-zag lines being more independent, destroying the stripes, but leaving the physics within individual zig-zag lines unaltered.

4.6. Connection to coherence

So far we considered the atomic real space density as our observable. In our setup we can also measure in momentum space via standard free expansion, i.e., without a

hold time in a harmonic trap. In particular, this gives access to the phase coherence between the lattice sites. There are two questions to be answered concerning the role of coherence in the pattern formation: is coherence necessary for the emergence of the pattern on the one hand, and on the other hand, how does the coherence evolve during the pattern formation?

4.6.1. Role of initial coherence

We investigate the importance of the coherence of the initial state by deliberately reducing it by a variable hold time in the lattice before the quench of the magnetic trap. For every set of experimental parameters we take an image after standard time-of-flight free expansion in order to obtain the visibility of the momentum distribution Bragg peaks. For these calibration images we do not quench the position of the magnetic trap because we are interested in the initial state. Additionally, for the same preparation parameters, we take a quantum gas magnifier image after a hold time of 100 ms after the quench and measure the density-wave contrast. In Fig. 4.11a-h, such images are shown for 4 different heating times in the lattice. It can be clearly seen that with decreasing visibility—i.e., coherence—in the initial state the pattern gets less pronounced as well. The visibility is defined as

$$\mathcal{V} = \frac{N_{\text{peak}} - N_{\text{nopeak}}}{N_{\text{peak}} + N_{\text{nopeak}}}, \tag{4.21}$$

where $N_{\text{peak}}(N_{\text{nopeak}})$ is the atom number within a circular region around the Bragg peaks(around positions rotated by 30° with respect to the Bragg peaks) as shown in the inset of Fig. 4.11i. The radius of the circles is determined from an inverted parabola fit to the Bragg peaks. The density-wave contrast as a function of the visibility of the initial state is plotted in Fig. 4.11i. We obtain a rather smooth increase of the density-wave contrast with increasing visibility. Still the data shows that there seems to be the need for a minimal coherence in the initial state corresponding to a visibility of $\sim 0.2 - 0.3$ for the density-wave to be detectable.

We can also address the question of the role of the coherence of the initial state in the framework of the c-field simulation. It is difficult to obtain a visibility from the simulations for direct comparison. The temperature, however, is an input parameter of the simulation and therefore known. Thus we plot the theoretical density-wave contrast as a function of $1 - T/T_{\text{c}}^0$ where T_{c}^0 is the critical temperature of a non-interacting system (Fig. 4.11j). The resulting density-wave contrast is higher for lower temperatures. Even though experiment and theory use different x-axis here, the two x-axis are a monotone function of each other and we can therefore deduce qualitative agreement between experiment and theory.

It is not obvious why the coherence of the initial state should play a role for the pattern formation. In fact, when approximating the propagator as an exponential decay as in section 4.2.2 the correlations are predicted to decrease with increasing phase coherence length as can be seen from (4.11). However for very long coherence
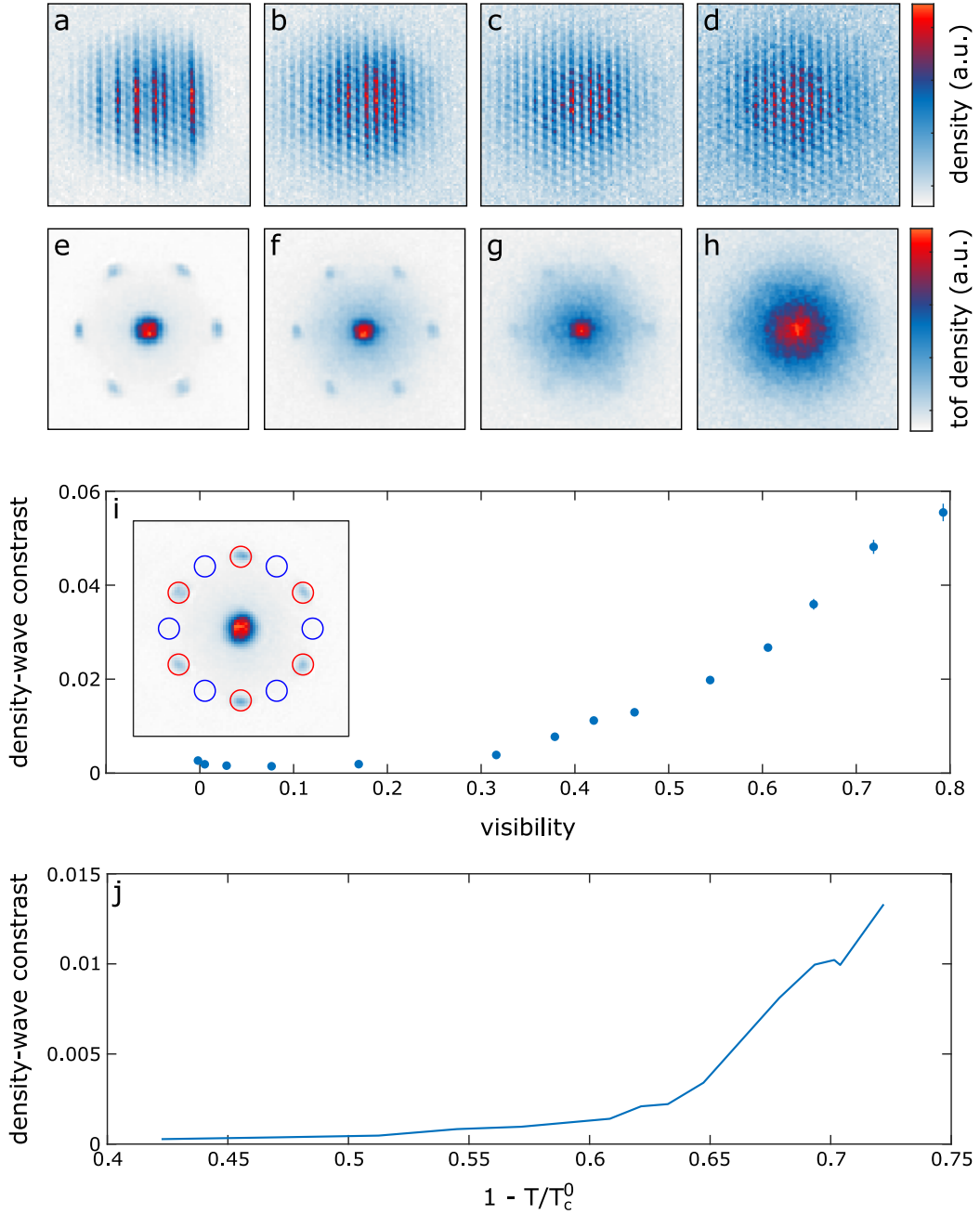
Figure 4.11.: Dependence on initial coherence. **(a-d)**, experimental real space images for 100 ms hold time after the quench and different initial temperatures. **(e-h)**, momentum space images taken without any quench, thus characterizing the coherence of the initial state. The temperature is controlled via a hold time in the lattice of (a,e) 0.1 ms, (b,f) 750 ms, (c,g) 1200 ms, (d,h) 1800 ms. The resulting visibilities are (e) 0.79, (f) 0.42, (g) 0.17, (h) 0.006. **(i)**, density-wave contrast after 100 ms after the quench as obtained from the experimental images as a function of visibility before the quench. The errorbars denote the standard deviation of the mean. The inset shows the masks used for the determination of the visibility. **(j)**, density-wave contrast as obtained from the c-field simulation results as a function $1 - T/T_{\mathrm{c}}^0$ where T_{c}^0 is the critical temperature of a non-interacting gas. Adapted from [90].

range this result might not be valid because the used approximation for the propagator becomes inaccurate. One explanation for the decrease in density-wave contrast might be that thermal excitations reduce the bosonic enhancement of the pair tunneling, thus making the pattern formation too slow to be observed. Another explanation could be that thermal fluctuations might seed the density-wave formation and that there are too many possible seeds for higher temperatures which eventually cancel each other.

4.6.2. Fate of coherence after the quench

After having described the influence of the coherence of the initial state, we now want to proceed with investigations of the coherence during the pattern formation. Fig. 4.12a-d shows momentum space images for different hold times after the quench in a stroboscopic timing with respect to the Bloch oscillation period of about 1 ms. The visibility is swiftly reduced, only a slight asymmetry remains with a slight elongation along the tilt direction. This shows that the quantum gas magnifier is essential for the observation of the pattern formation since with the loss of coherence there is no possibility to observe the density-wave in momentum space.

The c-field simulation comes to a similar conclusion. Here the coherence is esti-
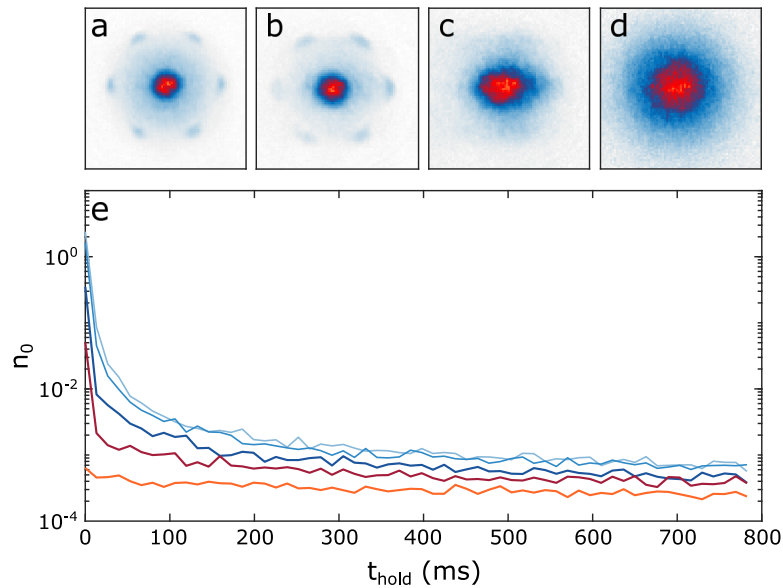
Figure 4.12.: Coherence after the quench. **(a-d)**, experimental momentum distribution of the atoms after (a) 0.1 ms, (b) 1.1 ms, (c) 2.1 ms, and (d) 1200 ms after the quench. **(e)**, coherence measure n_0 of the c-field simulation as explained in the main text as a function of hold time after the quench for different initial temperatures of $T/T_c = 0.28$, 0.32, 0.39, 0.45 and 0.53 from top to bottom. Adapted from [90].

mated by the parameter

$$n_0 = \left\langle \left| \frac{1}{N_{\mathrm{roi}}} \sum_i \psi_i \right|^2 \right\rangle_{\mathrm{ensemble}}, \tag{4.22}$$

i.e., the ensemble expectation value of the absolute value of the average complex field ψ_i in a region of interest. The region of interest is circular with a radius of 6 sites. n_0 is plotted as a function of hold time for different initial temperatures in Fig. 4.12e. Here as well, the coherence drops steeply (note the logarithmic scale).

4.7. Dependence on atom number

The freezing of the dynamics due to atom loss is already a strong indicator that the pattern formation is an interaction induced effect. As such it is almost mandatory to analyse the dependence of the phenomenon on density, i.e., atom number per tube.
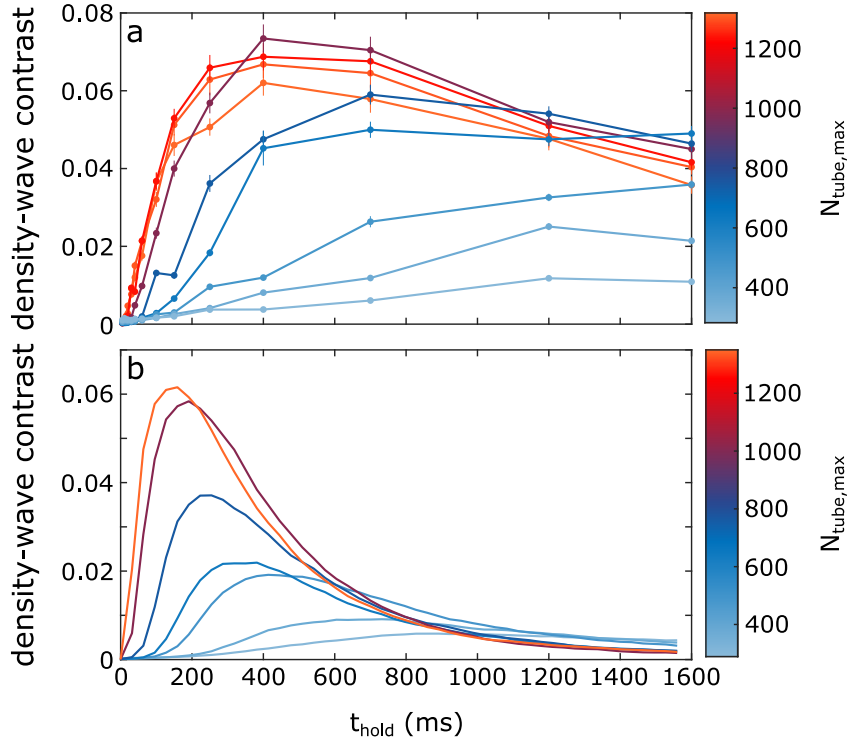
Figure 4.13.: Density dependence of the pattern formation. **(a)**, density-wave contrast as a function of hold time after the quench measured experimentally for different atomic densities. The color encodes the initial peak atom number per tube. The errorbars show the standard deviation of the mean. **(b)**, density-wave contrast in c-field simulations as a function of hold time for different densities, color-coded by peak on-site population as well. Adapted from [90].

The lack of a Feshbach resonance for ^{87}Rb as well as the use of magnetic trapping prohibits a scan as a function of scattering length. We vary the atom number by a hold time in the magnetic trap while applying RF radiation on the final evaporation frequency during preparation in order to lose atoms without heating. Experimentally we observe that for the most part higher peak atom numbers lead to faster dynamics and larger maximal value of the density-wave contrast (Fig. 4.13a). For the highest densities a saturation in the time scale and a slight decrease in the maximal value is measured.

We can simulate the same situation using a c-field simulation without atom loss. The phenomenology is the same, however, the maximum density wave contrast is a monotone function of the peak atom number while still saturating.

These findings reassure the interaction driven nature of the pattern formation. The slight decrease in maximal contrast for the highest densities in the experiment remains to be explained.
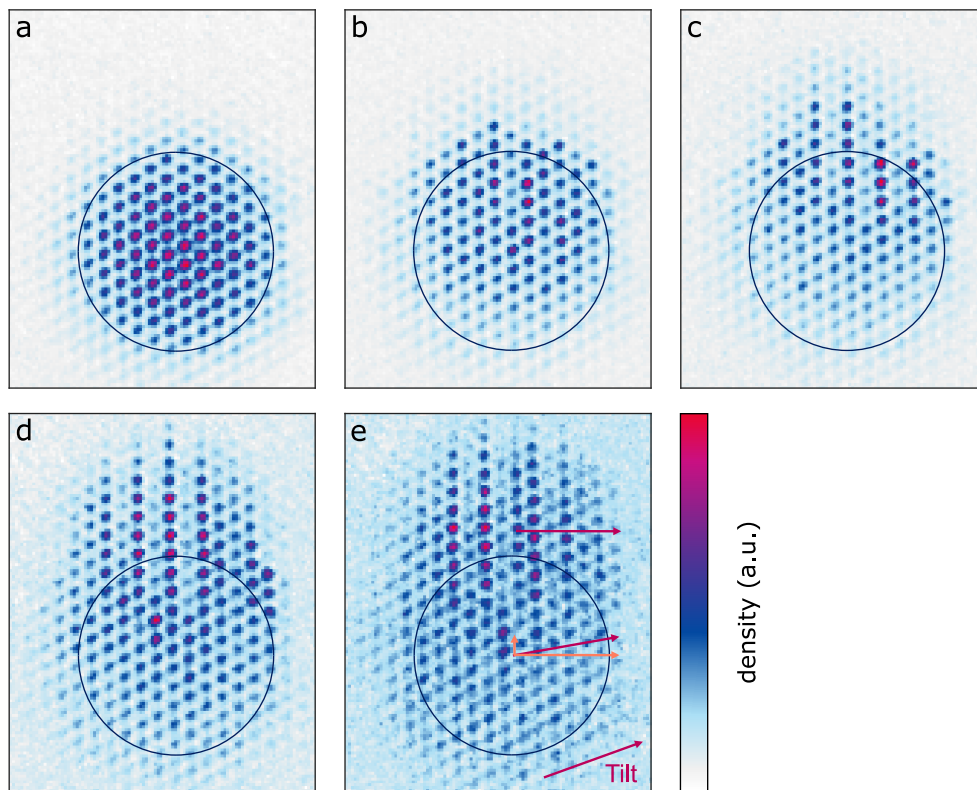
Figure 4.14.: Dynamics for incommensurate tilt direction. **(a-e)**, atomic real-space density after a hold time of (a) 1 ms, (b) 100 ms, (c) 300 ms, (d) 600 ms, (e) 1200 ms after the quench. The circle illustrates the initial position of the cloud. In (e) the local tilt is shown by red arrows. For the initial position of the cloud the tilt projection perpendicular and parallel to the columns of the lattice is drawn in orange. Adapted from [90].

4.8. Incommensurate tilt direction

So far we only considered the tilt direction to be perpendicular or parallel to a primitive vector. In another set of experiments we choose the tilt direction to be a bit off from being perpendicular to a primitive vector (Fig. 4.14e). Consequently, when decomposing the force into a component perpendicular to the columns of the lattice and a component parallel to it, neither vanishes. This is in contrast to the situation when tilting perpendicularly or parallel to a primitive vector where the projection along the columns is zero. Interestingly we observe that only a fraction of the atoms follow the force along the columns, reminiscent of a sample with both normal and superfluid part at the slope of a trap [98]. The moving fraction stops as soon as its center is at a position where the component of the force along the columns vanishes. At the same time this displaced part of the cloud shows density-wave formation. Since we know that coherence is necessary for the pattern formation (section 4.6) the fact that only the moving part exhibits a pattern is another hint that the moving part is the initial BEC part of the cloud. As such, future work could try to exploit this in order to prepare a perfectly condensed sample.

4.9. Conclusion

To conclude, we reported spontaneous symmetry breaking in the quench dynamics of a BEC in a triangular lattice after a sudden tilt. The spontaneous nature could be identified by a domain analysis of the resulting pattern. The phenomenon can be understood via an effective Hamiltonian and a c-field simulation, both confirming interactions as necessary ingredient for the dynamics. In particular, as such, particle loss is slowing down and almost freezing the dynamics leading to the pattern being very long-lived. Tunneling transverse to the tilt could be identified as necessary for strong correlations in the density along this direction whereas the anti-ferromagnetic correlations in tilt direction were found to be independent of this tunneling. The pattern formation is a first example of a phenomenon that could be observed only due to the development of the quantum gas magnifier to the best of our knowledge.

5. Conclusion and outlook

In conclusion, we introduced matter wave magnification as a tool for single shot imaging of 3D systems with 2D sub-lattice site resolution, making regimes accessible that were not accessible in real space beforehand, in particular systems of lattices of tubes. We benchmarked the technique by high precision thermometry of the normal gas to superfluid phase transition, demonstrated the capability to prepare various patterns as initial state, performed experiments with sub-lattice site resolution and analyzed thermal and quantum on-site fluctuations. In a next step we made use of the combined advantages of the quantum gas magnifier to observe spontaneous symmetry breaking in a BEC in a tilted triangular lattice with weak transverse confinement. This phenomenon was not experimentally accessible and not theoretically predicted to the best of our knowledge. In collaboration with the theory group of Ludwig Mathey, the dynamics could be understood in terms of an effective Hamiltonian originating from a Magnus expansion for strong tilt and the pattern formation was observed in c-field simulations as well.

The quantum gas magnifier puts much less constraints on experimental design than other high resolution techniques such as, e.g., quantum gas microscopes which rely on a high numerical aperture objective and fluorescence imaging in a pinning lattice. As such, quantum gas magnification can bring excellent real space resolution to atomic or molecular species where deep lattices are not available. Additionally, the absence of parity projection due to light assisted collisions allows for the measurement of higher fillings. When combining the magnification protocol with free space fluorescence imaging [22, 99, 100] also single-atom sensitivity can be reached, giving access to highly correlated states. The sub-lattice site resolution could be used to observe exotic on-site density distributions such as vortices in the case of a chiral superfluid [101].

Furthermore, the technique is suitable for the investigation of coherence phenomena [22, 57]. For example, the Talbot effect can be used to extract the coherence length of the system [57, 102]. In fact, the spatial resolution of the quantum gas magnifier would allow to analyze these properties also locally. It would be particularly interesting to observe the Talbot interference of a sample with a non-trivial phase pattern such as a twisted superfluid [103], or a sample with finite quasimomentum or a vortex [57]. For a BEC subject to an artificial gauge field, domain formation could be imaged [104–106]. Another proposal to access phase information is to imprint phase masks in the Fourier plane, i.e., after the evolution in the harmonic trap [29].

The effective Hamiltonian description of the density-wave formation shows that Floquet systems based on DC driving are promising for the engineering of extended Hubbard models [94, 107]. In the future it would be interesting to engineer stronger

non-standard Hubbard terms such that pattern formation and spontaneous symmetry breaking could be observed also in the ground state. Another route would be the combination of DC drive and AC drive, where the DC drive provides non-linear terms and the AC drive can make the system topologically non-trivial, potentially enabling the observation of phenomena like topological bandgap solitons [108]. The same combination, this time used for time translation symmetry and protection against run-away heating could lead to the observation of stark time crystals [109]. Eventually, AC drive combined with the engineering of a topological interface in the system points a way to the observation of chiral edge states, also in interacting topological matter [110].

Appendix A.

Details on the experimental setup

The experiment requires a lot of different laser beams of well-controlled frequency and sufficient power being directed onto the atoms. Therefore, the setup is divided into three optical tables: One table to provide the MOT, molasses, pushing, pumping and imaging light, one table to provide the high power beams for the optical lattice and a dipole trap and finally the experiment optical table which is connected to the other two via optical fibres. On the experiment table the vacuum chamber and the glass cells for the atoms are located. The experiment was mainly set up by earlier generations of PhD students. The main improvement in the course of this thesis consists of the implementation of the multi-frequency lattice (section 2.3.2). Yet, there is no detailed documentation of the current status of the setup in other theses which I will therefore provide here.

A.1. The MOT laser table

The MOT laser table provides all the frequencies needed for the MOT, molasses, pumping and imaging. Most of these beams are derived from the laser in the lower right of Fig. A.1 which is a TOPTICA DL PRO operated at 780 nm. The beam of this laser is divided for three major purposes. One part of the beam is sent through a saturated absorption spectroscopy setup for locking, one part is amplified to serve as cooling light for the MOT and molasses, and one part is used for pushing, optical pumping, and detection.

Let us start with the explanation of the spectroscopy beam path. This beam is transmitted through the first polarizing beam splitter (PBS). Subsequently the beam propagates through an EOM, adding the sidebands required for the spectroscopy, a double pass AOM for frequency tuning, a glass cell containing both ^{85}Rb and ^{87}Rb and finally it hits a photodiode for the detection of the locking signal. Using a TOPTICA DigiLock, the laser is locked onto the crossover resonance between the $F = 2 \rightarrow F' = 2$ and the $F = 2 \rightarrow F' = 3$ transitions which is detuned by $\Delta_{\mathrm{cross}} = -133\,\mathrm{MHz}$ from the $F = 2 \rightarrow F' = 3$ cooling transition. The double pass AOM using the minus first order detunes the light by $\Delta_{\mathrm{cool,spec}} = -2 \times 133\,\mathrm{MHz}$. The other beam paths involve AOMs as well in order to arrive at the desired frequencies as will be explained below.
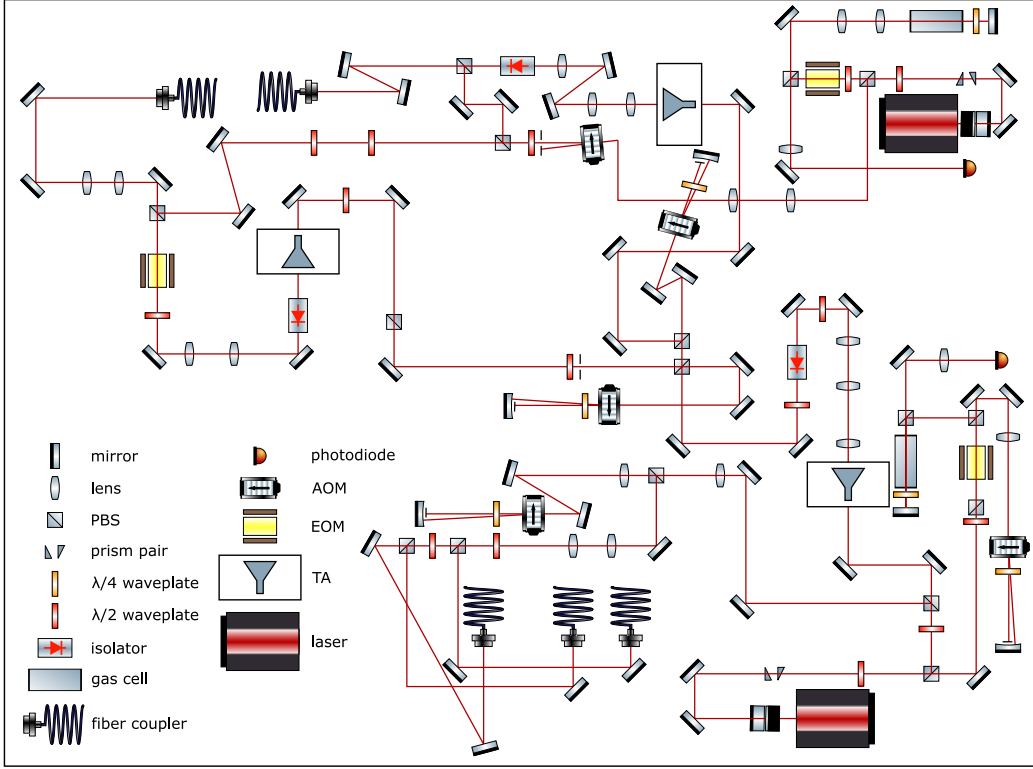
Figure A.1.: MOT laser table. Optical setup used to generate the laser light required for the MOT, molasses, pushing, optical pumping and imaging. A description of the individual beam paths can be found in the text.

Next, let us explain the beam path of the cooling light. The part of the beam used for this purpose is reflected by the first PBS and transmitted through the second. The power is amplified to around 100 mW by a first tapered amplifier (TA). After that the beam is divided into two, one for the 2D MOT and one for the 3D MOT. Each beam propagates through an individual double pass AOM, gets amplified to a few hundreds of mW by a second TA and is then coupled into a fibre connecting to the main experimental table. The double pass for the 3D branch uses the minus first order resulting in a shift of $\Delta_{\mathrm{cool,3D,MOT,2p}} = -2 \times 74\,\mathrm{MHz}$ in the MOT phase and of $\Delta_{\mathrm{cool,3D,mol,2p}} = -2 \times 88\,\mathrm{MHz}$ in the molasses phase. Hence, in total the detuning of the 3D cooling light is $\Delta_{\mathrm{cool,3D,MOT}} = \Delta_{\mathrm{cross}} - \Delta_{\mathrm{cool,spec}} + \Delta_{\mathrm{cool,3D,MOT,2p}} = -15\,\mathrm{MHz}$ during the MOT and $\Delta_{\mathrm{cool,3D,mol}} = \Delta_{\mathrm{cross}} - \Delta_{\mathrm{cool,spec}} + \Delta_{\mathrm{cool,3D,mol,2p}} = -43\,\mathrm{MHz}$ during the molasses. $\Delta_{\mathrm{cool,spec}}$ has an extra minus sign because the frequency shift happens before the propagation through the gas cell used for locking. The natural linewidth of the corresponding transition is $\Gamma = 2\pi \times 6.065(9)\,\mathrm{MHz}$ [54]. The path for the 3D MOT also involves an EOM which can quickly change the polarization of the light. During the MOT and molasses the light gets transmitted through the PBS just behind the EOM but for switch off the polarization is changed such that it gets reflected and dumped.

Eventually, we consider the fraction of the beam that is reflected at the second PBS, which is used for pushing, pumping and detection. The light is also shifted in frequency by a double pass using the minus first order. Subsequently the beam is split up again and coupled into three fibers: One for the push beam of the 2D MOT, one for the imaging perpendicular to the lattice plane and for the optical pumping and one for the imaging in the lattice plane. The AOM frequency is adjusted according to the experimental sequence. During the MOT phase the detuning is $\Delta_{\mathrm{PPI,push,2p}} = -2 \times 60.5\,\mathrm{MHz}$, resulting in $\Delta_{\mathrm{PPI,push}} = \Delta_{\mathrm{cross}} - \Delta_{\mathrm{cool,spec}} + \Delta_{\mathrm{PPI,push,2p}} = +12\,\mathrm{MHz}$ total detuning, during the optical pumping $\Delta_{\mathrm{PPI,pump,2p}} = -2 \times 73.5\,\mathrm{MHz}$, resulting in $\Delta_{\mathrm{PPI,pump}} = \Delta_{\mathrm{cross}} - \Delta_{\mathrm{cool,spec}} + \Delta_{\mathrm{PPI,pump,2p}} = -14\,\mathrm{MHz}$ and during imaging $\Delta_{\mathrm{PPI,imag,2p}} = -2 \times 66.5\,\mathrm{MHz}$, resulting in $\Delta_{\mathrm{PPI,imag}} = \Delta_{\mathrm{cross}} - \Delta_{\mathrm{cool,spec}} + \Delta_{\mathrm{PPI,imag,2p}} = 0\,\mathrm{MHz}$. Note that we rounded to full MHz here and that the value for the imaging AOM frequency used in the experiment is not computed but experimentally determined by maximizing the atomic absorption.

The last bit on the MOT laser table is the repumping laser system. Here as well we use a TOPTICA DL PRO running at 780 nm stabilized by a saturated absorption spectroscopy lock. For this laser we choose the crossover between the $F = 1 \to F' = 1$ and the $F = 1 \to F' = 2$ transitions as the lock point resulting in a detuning of $\Delta_{\mathrm{cross,rep}} = -78.5\,\mathrm{MHz}$ from the repumping transition $F = 1 \to F' = 2$. The beam passes through a single pass AOM at $\Delta_{\mathrm{rep,1p}} = 78\,\mathrm{MHz}$ which brings the repumping on resonance.

There is an analogue setup for ^{40}K in the experiment. However it was not used for the results reported in this thesis and is therefore not described.

A.2. The high power laser table

The second table which supplies the experiment with the desired laser light hosts the high power lasers (Fig. A.2). For the 2D lattice we have a COHERENT 25 W Mephisto MOPA (master oscillator power amplifier) emitting at a wavelength of 1064 nm. After passing through an optical isolator the power is distributed into four beams by the means of $\lambda/2$ waveplates and PBS. The beam which is reflected at the first PBS is not used for this thesis. The remaining three have qualitatively the same optical setup. Each beam first passes through an EOM which is required for the ability to use the multi-frequency lattice approach (section 2.3.2). Subsequently each beam propagates through an AOM which is used for fast switching of the light. In the case of the polarization approach the AOM frequencies need to be chosen equal whereas in the case of the multi-frequency approach they need to be chosen such that every carrier is resonant with exactly one sideband of another beam. As long as these conditions are met the exact frequencies do not matter since the lattice is far-detuned already. Note that the AOMs can also be used to effectively phase modulate the beams allowing for shaking protocols which was used excessively in former works [56]. The zeroth order of the AOMs is picked up by a small mirror and then
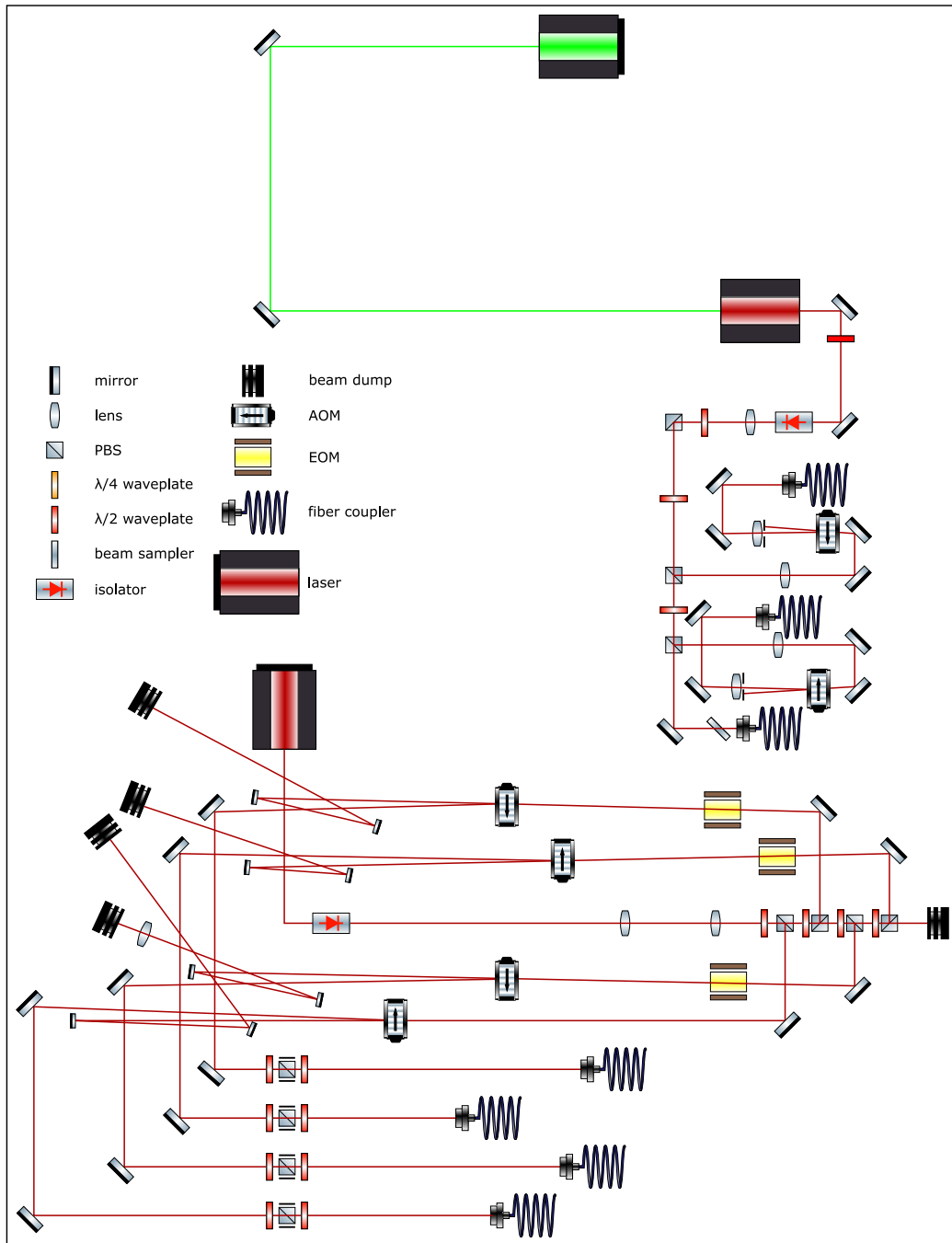
Figure A.2.: High power laser table. This table hosts the laser for the 2D lattice and the laser system for the dipole trap or transverse lattice. See the text for a detailed description.

redirected onto a high power beam dump. Eventually all beams are fiber coupled.

Independently from this setup but on the same table there is a Ti-sapphire laser system COHERENT MBR-110 with its pump laser COHERENT Verdi V18 which provides the power for a dipole trap or lattice perpendicular to the 2D lattice plane. The pump laser operates at 532 nm and is coupled into the Ti-sapph via two mirrors which converts the light to a wavelength of 826 nm. The light passes then through a filter to ensure that all green pump light is eliminated. The beam is subsequently divided into three parts. One is of low power and is fiber coupled to a wavemeter to monitor the frequency of the system. The other two have an identical setup of an AOM followed by a fiber. Here the AOM frequencies are chosen to be 75.5 MHz for one beam and 85 MHz for the other which prevents them from interfering when being used as a crossed dipole trap. At the same time the AOMs can again be used for fast switching. One of the beams can be retroreflected to form a lattice as will be described in the next section.

A.3. The experiment table

Finally we have arrived at the main table. The main table's mechanical design is very different from the other two. Whereas all the optics is mounted in a single plane for the other two tables, on the main table, optics are mounted on different breadboards at different height, from above and from below, and there is even a breadboard which is mounted vertically (Fig. A.3).

We want to explain the setup along the experimental sequence. The first stage of every experiment is the 2D MOT. The breadboard relevant here is breadboard A in
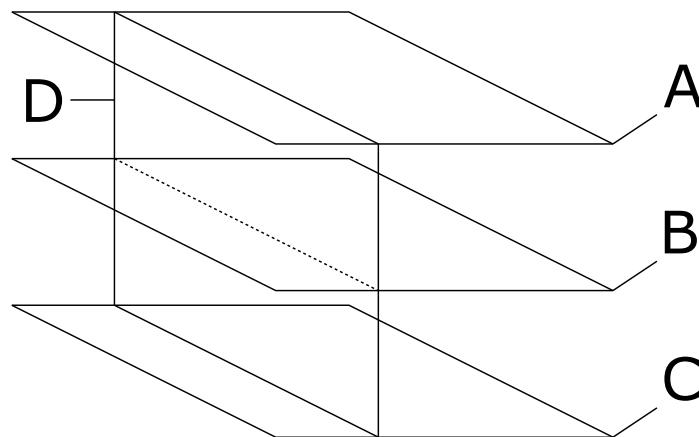
Figure A.3.: Experiment table, spatial arrangement of the breadboards. The setup on the experiment table can be subdivided into four breadboards. Three of them, labelled A,B,C, are mounted horizontally, where C is the optical table itself. One is mounted vertically, labelled D. The optics mounted on the breadboards are detailed in Fig. A.4&A.5.
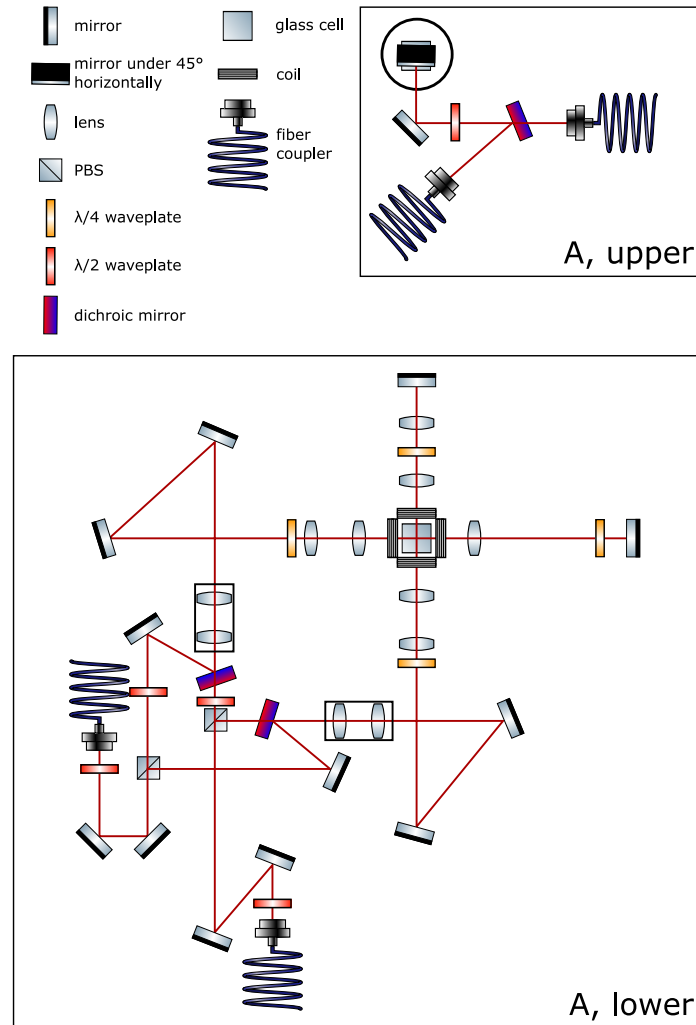
Figure A.4.: Experiment table, 2D MOT. The Optical setup and coils to realize the
2D MOT are displayed. The figure shows the upper side (A, upper) and lower side
(A, lower) of breadboard A mounted as defined in Fig. A.3, the beam paths are
explained in the text.

Fig. A.3 with its optics setup shown in Fig. A.4. It has components from above and
below, we will start with the ones mounted from below. There are two fiber out-
couplers, one for the potassium frequencies—which was not used in this thesis—and
one for the rubidium frequencies, i.e., the cooling and repumping light which were
coupled into this fibre on the MOT laser table. The light is divided onto two axes
which have almost the same setup. First, the beams are expanded symmetrically by
a telescope, then pass a quarter waveplate for circular polarization and are finally
expanded again, but only in the direction of gravity, using a cylinder telescope. The
circularly polarized, elliptical beams pass through the 2D glass cell where the dis-
penser creates a rubidium background pressure. Behind the glass cell the beams are
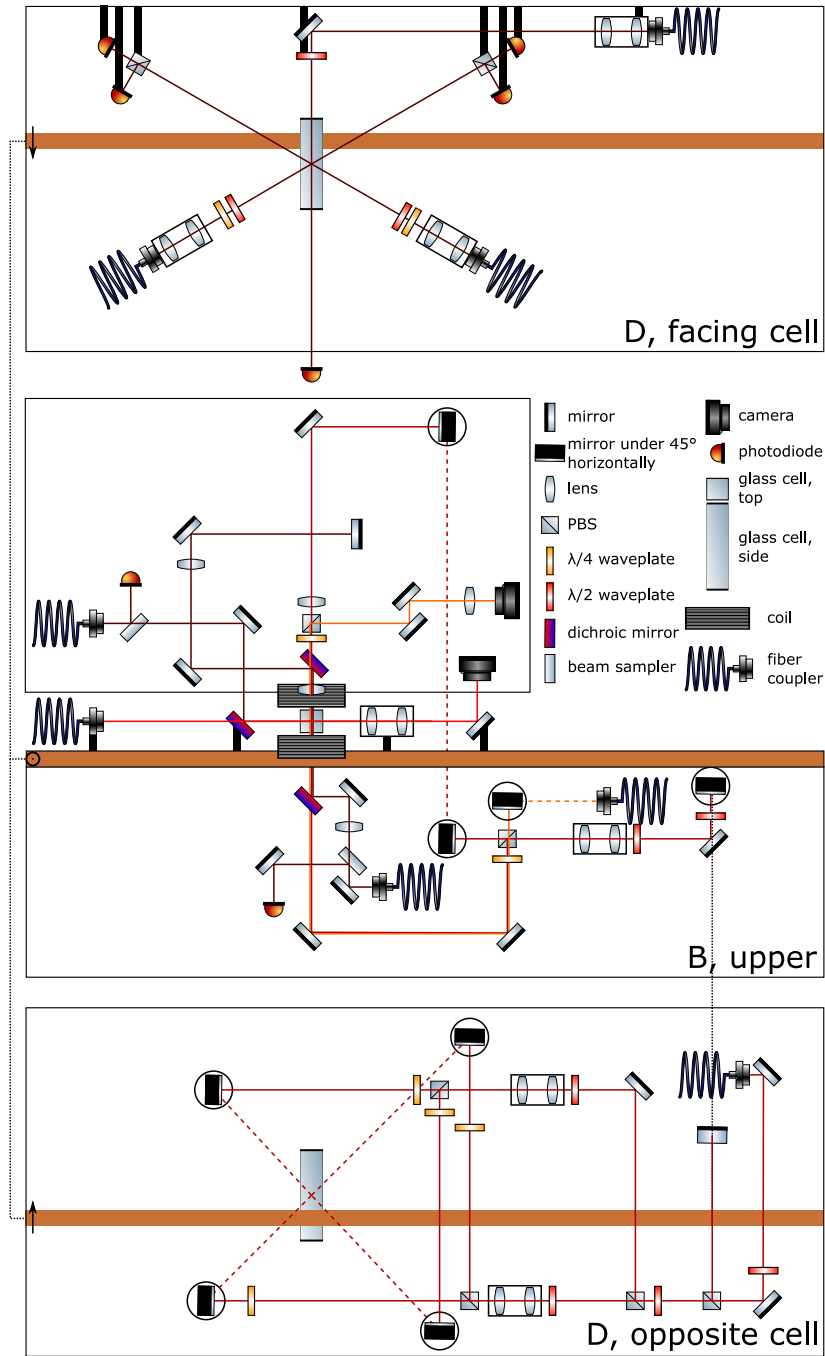
Figure A.5.: Experiment table, setup around glass cell in which experiments take place. The breadboards B and D as defined in Fig. A.3 are shown. The drawings should be put together such that the arrows on the left connected by a dashed line overlap. The circle with dot corresponds to the arrow pointing out of the plane. The dotted line between two mirrors means that these two are identical but drawn from different perspectives. Dashed beams propagate on the other side of the respective breadboard. Black rectangles indicate mounting of optics, in particular many elements on (D, facing cell) are mounted on breadboard C which is the optical table. The beam paths are described in the text.

retroreflected including a quarter waveplate for the appropriate polarization for the 2D MOT. Around each facing of the glass cell there is a coil in order to produce the quadrupole fields needed for the atom trapping.

On the upper side of this breadboard the optics for the push beam are mounted. Here we also have one outcoupler for potassium and one for rubidium where again only the one for rubidium was used in this thesis. The beam is directed along the axis of the 2D MOT pointing to the 3D MOT below.

Next in the experimental sequence we have the 3D MOT. The relevant optics can be found on breadboards B and on breadboard D (Fig. A.3&A.5). The cooling and repumping light are coupled out on breadboard D on the side opposite to the glass cell from a single fiber (dark red beam in Fig. A.5). This light gets divided into three branches which have the same design. In every branch the beam is expanded by a telescope and subsequently again divided into two beams which pass through a quarter waveplate for circular polarization and then impact the atoms from antiparallel directions. There is one pair of beams in the plane of breadboard B and two pairs in the plane of breadboard D, forming an angle of 45°with respect to gravity. These beams are also the ones used for the optical molasses. There is also an outcoupler for the potassium frequencies which is not shown because it was not used in this work. The potassium light gets distributed into three beams before superposition with the rubidium light using dichroic mirrors which is also not shown.

Subsequently the atoms are loaded into the magnetic trap, the coils of which are also shown in Fig. A.5. Before loading into the magnetic trap the atoms need to be pumped into a trappable state. The respective laser comes from a fibre below breadboard B and is overlaid with a MOT beam at a PBS (orange beam in Fig. A.5). It would also be possible to load into a dipole trap after evaporative cooling. Both beams of the crossed dipole trap arrive on breadboard B and first impact a beam sampler which reflects a small portion towards a photo-diode for the purpose of intensity stabilization (brown beams in Fig. A.5 on the upper side of breadboard B). The main part is transmitted and focused onto the atoms. Dichroic mirrors are used to overlay the dipole trap beams with the beams of other wavelengths. In this thesis however the dipole trap was not used.

We postpone the presentation of the lattice beams in order not to change breadboards. Two beams on breadboard B are left unexplained up to now. These are the imaging beams. The one for the imaging perpendicular to the lattice plane actually is the very same beam as the one used for the pumping (orange beam in Fig. A.5). Just the frequency is changed for imaging by means of the double pass AOM on the MOT laser table. Finally there is the imaging beam propagating in the lattice plane (red beam in Fig. A.5). This perspective is needed, e.g., for the lattice depth calibration of the lattice perpendicular to the 2D lattice plane.

The 2D lattice optics is presented on breadboard D (brown beams in Fig. A.5 on the site of breadboard D facing the cell). All beams have a telescope integrated into the fibre outcoupler such that no further lenses are required. Two of the beams have a quarter and a half waveplate, one only has a half waveplate. After propagating

through the glass cell the beams hit a photodiode which is used for intensity stabilization. The beams with two waveplates actually have two photodiodes at the different ports of a PBS which allows to use the setup as a polarimeter which is needed when a particular lattice geometry is to be prepared with the polarization approach (section 2.3). The quarter waveplates are removed when working with the multi-frequency approach, or more precisely the pair of quarter and half waveplate is replaced by a single half waveplate in order to be able to change back to the previous state. In fact only the outcouplers and waveplates above the cell are mounted on breadboard D. As indicated by the black bars in Fig. A.5 the remaining optics is mounted on breadboard C which is the actual optical table. Eventually, the lattice perpendicular to the 2D lattice is obtained by retroreflecting the respective dipole trap beam. The optics needed is mounted on breadboard B.

Appendix B.

Details on theoretical considerations

B.1. Band theory and band structure simulation

Band theory is the main framework for the modelling of systems with periodic potentials such as optical lattices. It is based on Bloch's theorem [111] which states that if a system has a discrete translational symmetry, i.e., the Hamiltonian commutes with the corresponding translation operator, then the eigenstates of the Hamiltonian take the form of Bloch waves

$$\psi_{nk}(x) = u_{nk}(x)e^{ikx}, \tag{B.1}$$

where n is called band index and k is the quasimomentum which is defined up to a reciprocal lattice vector. $u_{nk}(x)$ is a function which has the same periodicity as the lattice potential. We choose 1D for simplicity but higher dimensions are analogue. As a consequence of the periodicity of $u_{nk}(x)$ it can be written as a Fourier series

$$u_{nk}(x) = \sum_j c_{nk,j} e^{i\frac{2\pi}{a}jx}, \tag{B.2}$$

where a is the periodicity of the potential. In the same way the potential $V(x)$ can also be decomposed into Fourier coefficients V_j. Hence using the basis of Bloch functions (B.1) the time independent Schrödinger equation $H\psi_{nk} = E_{nk}\psi_{nk}$ can be mapped onto a system of equations in the Fourier coefficients of $u_{nk}(x)$

$$\frac{(k+jG)^2}{2m}c_{nk,j} + \sum_l V_l c_{nk,j-l} = E_{nk}c_{nk,j}, \tag{B.3}$$

with $G = 2\pi/a$. This kind of eigenvalue problem can be solved with the approximation of a cutoff as a function of j. Here however we want to take a different approach which is the computation and diagonalization of the Hamiltonian matrix in plane wave basis. The code is already presented in detail in the thesis of Nick Fläschner [56] and therefore we will just give the most important steps here.

   A very general approach of mapping the Schrödinger equation from a single equation in Hilbert space $H\psi = E\psi$ onto a (potentially infinite) number of equations of

complex numbers is to choose a basis of Hilbert space and to project the vectorial equation on every basis vector. Here we use the plane wave basis

$$|\boldsymbol{k}\rangle\,(\boldsymbol{r}) = \frac{1}{\sqrt{A}}e^{i\boldsymbol{k}\boldsymbol{r}}, \tag{B.4}$$

assuming an arbitrarily large but finite square area $A = L^2$ for the system in order to be able to normalize the basis. L is the edge length of the square. For periodic boundary conditions this implies $\boldsymbol{k} = 2\pi/L \times \boldsymbol{\nu}$ with integer vector $\boldsymbol{\nu} \in \mathbb{Z}^2$. Conveniently, these states are orthonormal. For every plane wave we can project the Schrödinger equation resulting in

$$\langle\boldsymbol{k}|\,H\,|\psi\rangle = \langle\boldsymbol{k}|\,E\,|\psi\rangle. \tag{B.5}$$

The right hand side is just the energy times the coefficient of the wave function in plane wave basis which we want to define as $c_{\boldsymbol{k}} = \langle\boldsymbol{k}|\psi\rangle$. On the left hand side we insert unity to obtain

$$\langle\boldsymbol{k}|\,H\,|\psi\rangle = \sum_{\boldsymbol{k}'} \langle\boldsymbol{k}|\,H\,|\boldsymbol{k}'\rangle\,\langle\boldsymbol{k}'|\psi\rangle = \sum_{\boldsymbol{k}'} \langle\boldsymbol{k}|\,H\,|\boldsymbol{k}'\rangle\,c_{\boldsymbol{k}'} \tag{B.6}$$

Thus in general an infinite dimensional eigenvalue problem needs to be solved:

$$\sum_{\boldsymbol{k}'} H_{\boldsymbol{k}\boldsymbol{k}'}c_{\boldsymbol{k}'} = Ec_{\boldsymbol{k}}, \tag{B.7}$$

where we defined $H_{\boldsymbol{k}\boldsymbol{k}'} = \langle\boldsymbol{k}|\,H\,|\boldsymbol{k}'\rangle$. In the following it will turn out, reflecting Bloch's theorem, that every plane wave is only coupled to a discrete set of other plane waves given by the reciprocal lattice and not the system size. This is due to the fact that the kinetic energy is diagonal in the plane wave basis and therefore does not couple different momenta at all, and, due to its periodicity, the potential only couples momenta that differ by exactly one reciprocal lattice vector. Therefore it is useful to decompose

$$\boldsymbol{k} = m_1\boldsymbol{b_1} + m_2\boldsymbol{b_2} + \boldsymbol{s} \tag{B.8}$$
$$\boldsymbol{k}' = n_1\boldsymbol{b_1} + n_2\boldsymbol{b_2} + \boldsymbol{q}, \tag{B.9}$$

where $\boldsymbol{b_1} = \boldsymbol{k_1} - \boldsymbol{k_2}$ and $\boldsymbol{b_2} = \boldsymbol{k_2} - \boldsymbol{k_3}$ are reciprocal lattice vectors and $\boldsymbol{q} = \beta_1\boldsymbol{b_1} + \beta_2\boldsymbol{b_2}$ and $\boldsymbol{s} = \gamma_1\boldsymbol{b_1} + \gamma_2\boldsymbol{b_2}$ are continuous momenta in the sense that their discretization is only given by system size. The continuous part is restricted to $0 \leq \beta_1, \beta_2, \gamma_1, \gamma_2 < 1$ and with $n_1, n_2, m_1, m_2 \in \mathbb{Z}$ the decomposition is thus unique. Note that only β_1 and β_2 will appear in the equations since only momenta with $\boldsymbol{q} = \boldsymbol{s}$ are coupled and hence it is always $(\beta_1, \beta_2) = (\gamma_1, \gamma_2)$. The matrix elements for the polarization approach

(section 2.3.1) are given by

$$\langle \boldsymbol{k}| \frac{\hat{p}^2}{2m} |\boldsymbol{k}'\rangle = 3E_{\mathrm{r}} \left((n_1 + \beta_1)^2 + (n_2 + \beta_2)^2 - (n_1 + \beta_1)(n_2 + \beta_2) \right) \delta_{m_1,n_1} \delta_{m_2,n_2} \delta_{\boldsymbol{q},\boldsymbol{s}} \tag{B.10}$$

$$\langle \boldsymbol{k}| \hat{V}_{23} |\boldsymbol{k}'\rangle = \frac{1}{2} \left(\sqrt{V_{2p}V_{3p}} - \sqrt{V_{2s}V_{3s}}e^{-i(\alpha_2-\alpha_3)} \right) e^{-i(\phi_3-\phi_2)} \delta_{m_1,n_1} \delta_{m_2,n_2+1} \delta_{\boldsymbol{q},\boldsymbol{s}}$$
$$+ \frac{1}{2} \left(\sqrt{V_{2p}V_{3p}} - \sqrt{V_{2s}V_{3s}}e^{i(\alpha_2-\alpha_3)} \right) e^{i(\phi_3-\phi_2)} \delta_{m_1,n_1} \delta_{m_2,n_2-1} \delta_{\boldsymbol{q},\boldsymbol{s}} \tag{B.11}$$

$$\langle \boldsymbol{k}| \hat{V}_{12} |\boldsymbol{k}'\rangle = \frac{1}{2} \left(\sqrt{V_{1p}V_{2p}} - \sqrt{V_{1s}V_{2s}}e^{i\alpha_2} \right) e^{-i\phi_2} \delta_{m_1,n_1+1} \delta_{m_2,n_2} \delta_{\boldsymbol{q},\boldsymbol{s}}$$
$$+ \frac{1}{2} \left(\sqrt{V_{1p}V_{2p}} - \sqrt{V_{1s}V_{2s}}e^{-i\alpha_2} \right) e^{i\phi_2} \delta_{m_1,n_1-1} \delta_{m_2,n_2} \delta_{\boldsymbol{q},\boldsymbol{s}} \tag{B.12}$$

$$\langle \boldsymbol{k}| \hat{V}_{13} |\boldsymbol{k}'\rangle = \frac{1}{2} \left(\sqrt{V_{1p}V_{3p}} - \sqrt{V_{1s}V_{3s}}e^{i\alpha_3} \right) e^{-i\phi_3} \delta_{m_1,n_1+1} \delta_{m_2,n_2+1} \delta_{\boldsymbol{q},\boldsymbol{s}}$$
$$+ \frac{1}{2} \left(\sqrt{V_{1p}V_{3p}} - \sqrt{V_{1s}V_{3s}}e^{-i\alpha_3} \right) e^{i\phi_3} \delta_{m_1,n_1-1} \delta_{m_2,n_2-1} \delta_{\boldsymbol{q},\boldsymbol{s}}, \tag{B.13}$$

with

$$V_{ip} = V_i \cos^2(\theta_i) \tag{B.14}$$
$$V_{is} = 2V_i \sin^2(\theta_i). \tag{B.15}$$

For the multi-frequency approach (section 2.3.2), the matrix elements of the kinetic energy are the same as for the polarization approach. The matrix elements of the potential are given by

$$\langle \boldsymbol{k}| \hat{V}_{23} |\boldsymbol{k}'\rangle = V_{23,0}e^{i\frac{\varphi_{\mathrm{g}}}{3}} \delta_{m_1,n_1} \delta_{m_2,n_2+1} \delta_{\boldsymbol{q},\boldsymbol{s}}$$
$$+ V_{23,0}e^{-i\frac{\varphi_{\mathrm{g}}}{3}} \delta_{m_1,n_1} \delta_{m_2,n_2-1} \delta_{\boldsymbol{q},\boldsymbol{s}} \tag{B.16}$$

$$\langle \boldsymbol{k}| \hat{V}_{12} |\boldsymbol{k}'\rangle = V_{12,0}e^{i\frac{\varphi_{\mathrm{g}}}{3}} \delta_{m_1,n_1+1} \delta_{m_2,n_2} \delta_{\boldsymbol{q},\boldsymbol{s}}$$
$$+ V_{12,0}e^{-i\frac{\varphi_{\mathrm{g}}}{3}} \delta_{m_1,n_1-1} \delta_{m_2,n_2} \delta_{\boldsymbol{q},\boldsymbol{s}} \tag{B.17}$$

$$\langle \boldsymbol{k}| \hat{V}_{13} |\boldsymbol{k}'\rangle = V_{13,0}e^{-i\frac{\varphi_{\mathrm{g}}}{3}} \delta_{m_1,n_1+1} \delta_{m_2,n_2+1} \delta_{\boldsymbol{q},\boldsymbol{s}}$$
$$+ V_{13,0}e^{i\frac{\varphi_{\mathrm{g}}}{3}} \delta_{m_1,n_1-1} \delta_{m_2,n_2-1} \delta_{\boldsymbol{q},\boldsymbol{s}}. \tag{B.18}$$

As already mentioned, conveniently, only plane waves that differ by exactly one reciprocal lattice vector $\boldsymbol{b}_1$, $\boldsymbol{b}_2$ or $\boldsymbol{b}_1 - \boldsymbol{b}_2$ are coupled. Thus the problem can be decomposed into several smaller ones, each only considering one central momentum and all momenta that can be reached via reciprocal lattice vectors. Still, these subsets are infinite, so a cutoff needs to be made. It is a good approximation to leave out high momenta since the low energy states in a shallow lattice resemble those of free particles, which are plane waves with no admixture from higher wave vectors of the respective reciprocal lattice. Going to deeper lattices higher momenta become more

relevant and the cutoff needs to be shifted. In the simulations used in this thesis, typically a reciprocal lattice of 17×17 momenta is employed corresponding to the same number of bands.

B.2. Modelling of sub-lattice site quench dynamics

Here we describe the simulation of the beam imbalance quench dynamics of section 3.5. Since the lattice is very deep we assume that the quasimomentum does not play a role as it is only defining the phase between lattice sites which do not interfere in this limit anyways. Thus, without loss of generality, we can choose our initial state to be the eigenstate with zero quasimomentum and use the band structure code from appendix B.1. The dynamics are simulated as follows. The initial state ψ_0 is obtained as the corresponding eigenvector and is therefore in plane wave basis:

$$|\psi_0\rangle = \sum_{\boldsymbol{k}} \langle \boldsymbol{k}|\psi_0\rangle \, |\boldsymbol{k}\rangle =: \sum_{\boldsymbol{k}} c_{\boldsymbol{k}}^{(0)} \, |\boldsymbol{k}\rangle \, . \tag{B.19}$$

Now for every time step n of $\delta t = 5\,\mu s$ a band structure calculation is run to obtain the instantaneous eigenstates

$$|\phi_i^{(n)}\rangle =: \sum_{\boldsymbol{k}} d_{\boldsymbol{k},i}^{(n)} \, |\boldsymbol{k}\rangle \, . \tag{B.20}$$

The need for many time steps stems from the fact that we use the measurements from the intensity control photodiodes instead of assuming a step function for the potential depth. The time evolution is done iteratively by computing the wave function after n time steps based on the wave function at time step $n-1$, assuming that the lattice depth was constant over the interval. Hence the wave function after n steps as a function of the wave function after $n-1$ steps is given by

$$|\psi_n\rangle = \sum_{i} \langle \phi_i^{(n)}|\psi_{n-1}\rangle e^{-i\frac{E_i^{(n)}}{\hbar}\delta t} \, |\phi_i^{(n)}\rangle = \sum_{i\boldsymbol{k}} \bar{d}_{\boldsymbol{k},i}^{(n)} c_{\boldsymbol{k}}^{(n-1)} e^{-i\frac{E_i^{(n)}}{\hbar}\delta t} \, |\phi_i^{(n)}\rangle \, . \tag{B.21}$$

The density from which the cuts in the main text are drawn is then given by

$$n(\boldsymbol{r}) = |\langle \boldsymbol{r}|\psi_n\rangle|^2 = \left| \sum_{\boldsymbol{k}} \langle \boldsymbol{r}|\boldsymbol{k}\rangle \langle \boldsymbol{k}|\psi_n\rangle \right|^2 = \frac{1}{A} \left| \sum_{\boldsymbol{k}} e^{i\boldsymbol{k}\boldsymbol{r}} c_{\boldsymbol{k}}^{(n)} \right|^2 \, . \tag{B.22}$$

Since this simulation considers a single particle, the density has to be scaled to match the experiment. Note the short time scale of the simulation justifying the neglection of interactions.

B.3. Computation of the trapping frequency perpendicular to the 2D lattice

For the correct comparison with theoretical expectations we need to know the trapping frequency in the z-direction since it influences the importance of interactions and defines the quantum of energy for transverse excitation. For this computation we need to take into account the full light intensity, not only the part that is spatially modulated. The full potential is given by

$$-\frac{V}{\kappa} = \frac{1}{T} \int_0^T |\boldsymbol{E}_1 + \boldsymbol{E}_2 + \boldsymbol{E}_3|^2 \, \mathrm{d}t \tag{B.23}$$

$$= \frac{1}{T} \int_0^T \left[|\boldsymbol{E}_1|^2 + |\boldsymbol{E}_2|^2 + |\boldsymbol{E}_3|^2 + 2\Re\left(\bar{\boldsymbol{E}}_1 \boldsymbol{E}_2 + \bar{\boldsymbol{E}}_2 \boldsymbol{E}_3 + \bar{\boldsymbol{E}}_3 \boldsymbol{E}_1 \right) \right] \mathrm{d}t \tag{B.24}$$

$$= |\boldsymbol{E}_1|^2 + |\boldsymbol{E}_2|^2 + |\boldsymbol{E}_3|^2 + \frac{1}{T} \int_0^T 2\Re\left(\bar{\boldsymbol{E}}_1 \boldsymbol{E}_2 + \bar{\boldsymbol{E}}_2 \boldsymbol{E}_3 + \bar{\boldsymbol{E}}_3 \boldsymbol{E}_1 \right) \mathrm{d}t \tag{B.25}$$

where $\boldsymbol{E}_i(\boldsymbol{r}, t)$ is the complex valued E-field, T is an averaging time which should be long compared to the frequencies of the light, κ is a proportionality constant. We restrict ourselves here to the multi-frequency approach because the experiments where we used the z trapping frequency were performed using this approach. Hence every beam has sidebands and every carrier only interferes with one sideband, resulting in, e.g.,

$$\frac{1}{T} \int_0^T 2\Re\left(\bar{\boldsymbol{E}}_1 \boldsymbol{E}_2 \right) \mathrm{d}t = 2\boldsymbol{e}_1 \boldsymbol{e}_2 J_0(\alpha) J_1(\alpha) |\boldsymbol{E}_1| |\boldsymbol{E}_2| \cos\left[(\boldsymbol{k}_1 - \boldsymbol{k}_2) \boldsymbol{r} \right], \tag{B.26}$$

with $J_0(\alpha)$, $J_1(\alpha)$ being Bessel functions corresponding to the strength of carrier and sidebands as a function of modulation index α. We extract the z trapping frequency by looking at the potential on the z-axis. Assuming $|\boldsymbol{E}_1| = |\boldsymbol{E}_2| = |\boldsymbol{E}_3|$ it is given by

$$\frac{V(0,0,z)}{\kappa} = -\left[3 + 6\boldsymbol{e}_1 \boldsymbol{e}_2 J_0(\alpha) J_1(\alpha) \right] |\boldsymbol{E}_{\max}|^2 \, e^{-\frac{2z^2}{w^2}} \tag{B.27}$$

with the peak electric field $|\boldsymbol{E}_{\max}|$ and the lattice beam waist w. A Taylor expansion to second order leads to the trapping frequency

$$\omega_{z,\mathrm{lat}} = \sqrt{\frac{4 \left[3 + 6\boldsymbol{e}_1 \boldsymbol{e}_2 J_0(\alpha) J_1(\alpha) \right] \kappa |\boldsymbol{E}_{\max}|^2}{mw^2}}. \tag{B.28}$$

Using the expression (B.26) we deduce that the 1D peak to peak lattice depth in this representation is given by $V_{1D}^{\mathrm{pp}}/2 = \kappa \times 2\boldsymbol{e}_1 \boldsymbol{e}_2 J_0(\alpha) J_1(\alpha) |\boldsymbol{E}_{\max}|^2$. In appendix C.1 we derive the conversion from peak to peak 1D lattice depth to our lattice depth convention which we can use here to get the final result

$$\omega_{z,\mathrm{lat}} = \sqrt{\frac{V_{ij,0}}{mw^2} \left[12 + \frac{6}{\boldsymbol{e}_1 \boldsymbol{e}_2 J_0(\alpha) J_1(\alpha)} \right]} \tag{B.29}$$

$$= 2\pi \times 19 \,\mathrm{Hz} \times \sqrt{\frac{V_{ij,0}}{E_{\mathrm{r}}}} \tag{B.30}$$

where we plugged in $J_0(\alpha)J_1(\alpha) = 1/3$, $\boldsymbol{e}_1\boldsymbol{e}_2 = 1$, $w = 140\,\mu\mathrm{m}$, $m = 87\,\mathrm{u}$. $V_{ij,0}$ is independent of i, j for a balanced lattice.

This trapping frequency usually is the dominating z-confinement. Yet, there is also a confinement induced by the magnetic trap. This confinement was characterized to be [39]

$$\omega_{z,\mathrm{MT}} = 2\pi \times 11\,\mathrm{Hz} \times \sqrt{\frac{I_{\mathrm{grad}}}{110\,\mathrm{A}}}. \tag{B.31}$$

I_{grad} is the current in the coils producing the quadrupole part of the magnetic trap. For the thermometry experiment in section 3.3 we used $I_{\mathrm{grad}} = 105\,\mathrm{A}$ resulting in $\omega_{z,\mathrm{MT}} = 2\pi \times 11\,\mathrm{Hz}$ (no change when keeping only 2 digits), for the experiments in chapter 4 we used $I_{\mathrm{grad}} = 85\,\mathrm{A}$ resulting in $\omega_{z,\mathrm{MT}} = 2\pi \times 9.7\,\mathrm{Hz}$. The trapping frequencies must be quadratically added to obtain the total trapping frequency making the magnetic trap only a small correction.

B.4. Computation of the on-site trapping frequency of a triangular lattice

When considering interacting particles in a lattice, the on-site trapping frequency is an important quantity since the stronger the confinement the more significant the interactions. Here we want to compute the on-site trapping frequency and oscillator length for the case of a balanced triangular lattice. In this case the lattice potential (2.7) is reduced to

$$V(\boldsymbol{r}) = -2V_{\mathrm{lat}} \sum_{i<j} \cos\left[(\boldsymbol{k}_i - \boldsymbol{k}_j)\,\boldsymbol{r}\right], \tag{B.32}$$

when choosing the origin appropriately. The on-site trapping frequency is proportional to the curvature of the potential

$$\frac{\partial^2 V}{\partial x^2}(0) = \frac{\partial^2 V}{\partial y^2}(0) = 2V_{\mathrm{lat}}\frac{9}{2}\left(\frac{2\pi}{\lambda}\right)^2. \tag{B.33}$$

The trapping frequency is consequently isotropic and given by

$$\omega^2 = \frac{1}{m}\frac{\partial^2 V}{\partial x^2}(0) = \frac{2V_{\mathrm{lat}}}{E_{\mathrm{r}}}\frac{9\hbar^2(2\pi)^4}{4m^2\lambda^4}. \tag{B.34}$$

The harmonic oscillator length is defined as

$$a_{\mathrm{ho,site}}^2 = \frac{\hbar}{m\omega} = \sqrt{\frac{2}{9}\frac{E_r}{V_{\mathrm{lat}}}}\frac{\lambda^2}{(2\pi)^2}. \tag{B.35}$$

For our experimental lattice laser wavelength we obtain

$$a_{\mathrm{ho,site}} = 116\,\mathrm{nm}\left(\frac{E_{\mathrm{r}}}{V_{\mathrm{lat}}}\right)^{\frac{1}{4}}. \tag{B.36}$$

B.5. Computation of the Hubbard on-site interaction strength

For the computation of the Hubbard on-site interaction strength U for the case of the triangular lattice of tubes we start from the expression of the interaction energy in a single tube with N particles in state $\varphi(x, y, z)$

$$E_{\text{int}} = gN^2 \int |\varphi(x, y, z)|^4 \, \mathrm{d}x\mathrm{d}y\mathrm{d}z. \tag{B.37}$$

Since the tubes are highly anisotropic we assume that the interactions do not play a role for the in-plane form of the wave function and that the wave-function factorizes as $\varphi(x, y, z) = \varphi_{\text{2D}}(x, y)\varphi_z(z)$. With the same argument we can compute $\varphi_{\text{2D}}(x, y)$ via non-interacting band structure numerics. In the z-direction we are in the opposite limit. Interactions dominate and therefore a Thomas-Fermi profile is suitable for $\varphi_z(z)$. For the Thomas-Fermi profile we choose an atom number of $N = 1000$ allowing us to obtain

$$U = \frac{2}{N^2} E_{\text{int}} \sim 2.3 \, \text{Hz} \tag{B.38}$$

for a lattice depth of $V_{\text{lat}} = 1E_{\text{r}}$. Note that the description of the system with such a Hubbard approach neglects the change of the Thomas-Fermi profile with particle number and therefore it is only accurate as long as the relative change in N remains small. Also note that the value of U is exclusively used for the computation of the pair tunneling time scale t_P. In particular, the c-field simulation discretizes the z-direction making $\tilde{U} = g/(2\pi a_{\text{ho}}^2 l_z)$ the relevant interaction strength.

B.6. Non-interacting bosons in a lattice with harmonic confinement

In this section we present a theoretical model for the normal to BEC transition in a triangular lattice of tubes with harmonic confinement. The critical temperature of a non-interacting Bose gas is implicitly given by the condition that the number of atoms in the excited states N_{exc} is equal to the total atom number N_{tot} at the critical temperature and vanishing chemical potential, since lowering the temperature further would imply that not all atoms can be accomodated in the excited states and therefore a macroscopic fraction needs to occupy the ground state [65]. This condition can be written as

$$N_{\text{tot}} = N_{\text{exc}}(\mu = 0, T_c^0) = \int \mathrm{d}E \frac{g(E)}{e^{\frac{E}{k_B T_c^0}} - 1}, \tag{B.39}$$

with the density of states $g(E)$. Hence if we know the density of states for our system we can compute $N_{\text{exc}}(T_c^0)$ which then can be numerically inverted to yield $T_c^0(N_{\text{tot}})$.
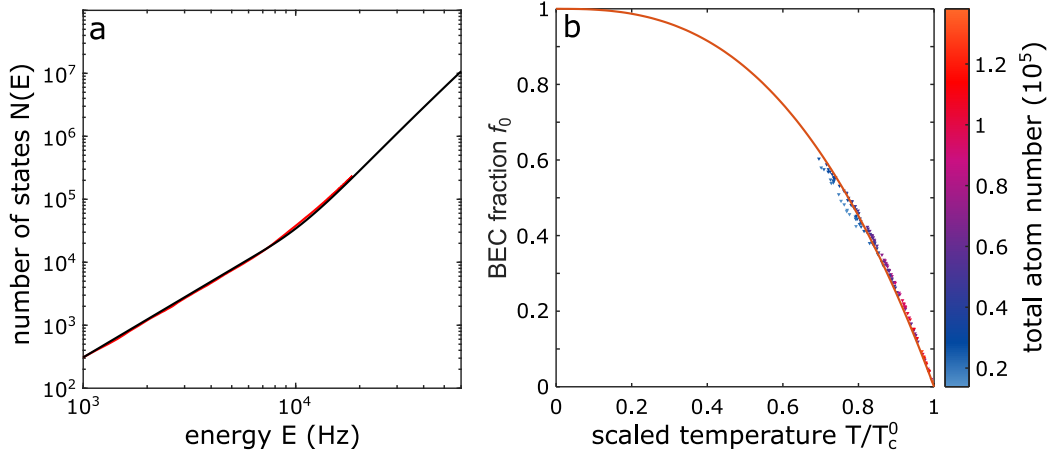
Figure B.1.: Theoretical model of the normal to BEC transition in a harmonically confined lattice of tubes without interactions. **(a)**, number of states $N(E)$ below a certain energy E. the red line is an exact diagonalization of a finite system with hard walls, the black line shows the analytical approximation described in the text. **(b)**, BEC fraction f_0 as a function of scaled temperature T/T_c^0. The symbols show the theoretical results for the parameters measured in the experiment. The color encodes the atom number. The solid line is a fit to these points using the relation $f_0 = 1 - (T/T_c^0)^\alpha$ as expected for a density of states with the form of a power law. The fit results in $\alpha = 2.69(1)$. Adapted from [22].

As a first step towards a density of states we perform a diagonalization of the Hamiltonian matrix corresponding to the position basis choosing a cutoff radius in order to keep the problem finite and tractable. We compute the number of states $N(E)$ (red line in Fig. B.1a) having an energy below a certain energy E because this quantity defines the density of states via $g(E) = \mathrm{d}N/\mathrm{d}E$. However it turns out that we cannot simulate energies high enough for an accurate critical temperature for the parameter range of the experiment.

Therefore we develop an analytical description. In fact, in the first band, the tunnel coupling $J = h \times 12\,\mathrm{Hz}$ is very small compared to the gradients due to the external trap. For example a site in the center of the trap is offset by $\Delta = 1/2m\omega_{\mathrm{sys}}^2 a_{\mathrm{lat}}^2 = h \times 200\,\mathrm{Hz}$ from its nearest neighbour. Therefore, it is a good approximation to assume independent sites for the first band, each site only having the z degree of freedom, since a in-plane excitation would correspond to higher bands. Consequently the spectrum in the lowest band is given by

$$E_{jk} = \frac{1}{2}m\omega_{\mathrm{sys}}^2 r_j^2 + \left(k + \frac{1}{2}\right)\hbar\omega_z, \tag{B.40}$$

with the distance r_j of the tube j from the trap center. For this spectrum $N(E)$ can be computed in the following way. First, the problem is decomposed into a sum over

the sites

$$N(E) = \sum_j N(E, r_j),$$ (B.41)

where the sum runs over all sites. The number of accessible states for a given site is obtained by subtracting the potential energy of the site from the available energy E and, if this is larger than zero, divide it by the quantum of z excitation $\hbar\omega_z$ resulting in

$$N(E, r_j) = \max\left[\lfloor \frac{E - \frac{1}{2}m\omega_{\mathrm{sys}}^2 r_j^2}{\hbar\omega_z} \rfloor, 0\right]$$ (B.42)

We approximate the sum in $N(E)$ by an integral and ignore the rounding down due to $\hbar\omega_z$ being small, yielding

$$N(E) = \int_0^{r_{\max}} \frac{2\pi r \mathrm{d}r}{A_{\mathrm{WS}}} \frac{E - \frac{1}{2}m\omega_{\mathrm{sys}}^2 r^2}{\hbar\omega_z},$$ (B.43)

where the max function was incorporated by including an upper bound in the integral given by $r_{\max} = \sqrt{2E/(m\omega_{\mathrm{sys}}^2)}$. Changing variables in the integral to $\tilde{r} = r/r_{\max}$ results in

$$N(E) = \frac{2\pi}{A_{\mathrm{WS}}} \frac{2E^2}{\hbar\omega_z m\omega_{\mathrm{sys}}^2} \int_0^1 \tilde{r}\mathrm{d}\tilde{r}\left(1 - \tilde{r}^2\right).$$ (B.44)

The integral is now just a number and equals $1/4$. Thus we arrive at the final expression

$$N(E) = \left(\frac{E}{E_0}\right)^2,$$ (B.45)

with

$$E_0 = \sqrt{\frac{\hbar A_{\mathrm{WS}} m\omega_{\mathrm{sys}}^2 \omega_z}{\pi}}.$$ (B.46)

For the parameters of the thermometry experiment we obtain $E_0 = h \times 57\,\mathrm{Hz}$.

Already the second band has a bandwidth which is an order of magnitude larger than the one of the first band. It turns out that the number of states in the higher bands is well described by the relation for particles experiencing the external confinement, but not the lattice. This relation is

$$N(E) = \frac{1}{6}\left(\frac{E}{\hbar\bar{\omega}}\right)^3,$$ (B.47)

with $\bar{\omega} = (\omega_{\mathrm{sys}}^2\omega_z)^{1/3}$ being the geometric mean of the trapping frequencies. This expression needs to be shifted by the band gap $\hbar\Delta_{\mathrm{g}}$ because this energy must be paid

in addition in order to enter all these states. Other than that we just need to add the two expressions to get the analytic approximate number of states as

$$N(E) = \left(\frac{E}{E_0}\right)^2 + \max\left[\frac{1}{6}\left(\frac{E - \hbar\Delta_{\mathrm{g}}}{\hbar\bar{\omega}}\right)^3, 0\right],\tag{B.48}$$

which is plotted as black line in Fig. B.1a. As described, inserting $g(E) = \mathrm{d}N/\mathrm{d}E$ into (B.39) allows the numerical computation of the critical temperature as a function of atom number, which in turn allows to renormalize the temperatures in Fig. 3.6b.

Furthermore we need a model to quantify the shift of the critical temperature that we see in the experiment. Given the density of states we can also compute the theoretically expected BEC fraction as

$$f_0(T) = 1 - \frac{N_{\mathrm{exc}}(\mu = 0, T)}{N_{\mathrm{tot}}} = 1 - \frac{1}{N}\int \mathrm{d}E \frac{g(E)}{e^{\frac{E}{K_{\mathrm{B}}T}} - 1}.\tag{B.49}$$

These values are plotted as a function of the renormalized temperature $T/T_{\mathrm{c}}^0(N_{\mathrm{tot}})$ in Fig. B.1b. It can be seen that the points are almost perfectly on a single line for the experimentally accessed temperatures and atom numbers. Note that due to the fact that the density of states is not a power law this was not clear a priori. It turns out that the points in Fig. B.1 can be fitted by the expression that is obtained for a power law $g(E) = C_\alpha E^{\alpha-1}$ which is

$$f_0 = 1 - \left(\frac{T}{T_{\mathrm{c}}^0}\right)^\alpha.\tag{B.50}$$

The fit yields $\alpha = 2.69(1)$ where the error corresponds to the 68% confidence interval of the fit. This value is used for the fitting in the main text, thus the only free fit parameter is a factor between the non-interacting prediction T_{c}^0 and the actual critical temperature T_{c}.

Appendix C.

Calibrations and conventions

C.1. Lattice calibration

The lattice depth is calibrated using Kapitza Dirac scattering. The intensity of every individual lattice beam can be deduced from the lattice depths of all three possible 1D lattices resulting from pairwise combination of the beams.

Let us consider such a Kapitza-Dirac experiment with a single 1D lattice [112]. We load a BEC into the magnetic trap and subsequently pulse the two lattice beams under consideration for a varying time of the order of microseconds and measure the density after time of flight. Since the intensity stabilization is not possible on such short time scales the pulse is performed with no stabilization. The maximal intensity is just given by the radio frequency provided to the AOMs of the lattice beams. We measure the voltage on the photodiodes of the intensity stabilization and in this way we know that if we later lock on exactly this voltage we get the lattice depth that we had during calibration. For other lattice depths we assume the lattice depth to be linear in the photodiode voltage.

For a short pulse the kinetic energy of the atoms can be neglected in the sense that the light potential

$$V_{1D} = -V_{1D}^{pp} \sin^2\left(\frac{k_{1D}x}{2}\right) \tag{C.1}$$

only imprints a phase pattern onto the cloud but does not redistribute density. Thus the wave function evolves according to

$$\psi(t) = \psi_0 \exp\left[\frac{i}{\hbar}t V_{1D}^{pp} \sin^2\left(\frac{k_{1D}x}{2}\right)\right] \tag{C.2}$$

Using a trigonometric and a Bessel-function identity we can rewrite this as

$$\psi(t) = \psi_0 \exp\left[\frac{i V_{1D}^{pp}t}{2\hbar} - \frac{i V_{1D}^{pp}t}{2\hbar}\cos(k_{1D}x)\right] \tag{C.3}$$

$$= \psi_0 \exp\left[\frac{i V_{1D}^{pp}t}{2\hbar}\right] \sum_{n=-\infty}^{\infty} i^n J_n\left(\frac{V_{1D}^{pp}t}{2\hbar}\right) \exp\left[ink_{1D}x\right]. \tag{C.4}$$
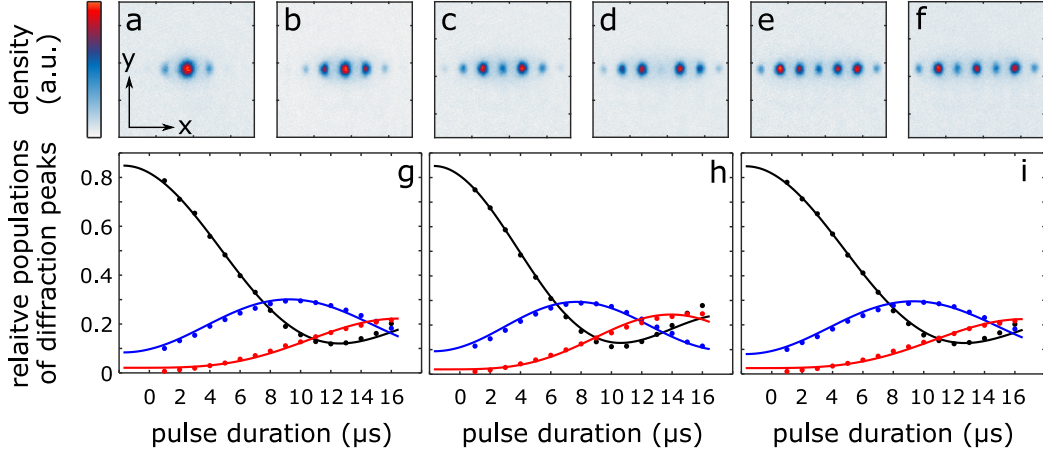
Figure C.1.: Lattice depth calibration using Kapitza-Dirac scattering. **(a-f)**, example images of a time series of Kapitza-Dirac scattering. The duration of the pulse is (a) 1 µs, (b) 4 µs, (c) 7 µs, (d) 10 µs, (e) 13 µs, (f) 16 µs. **(g-i)**, normalized populations of the diffraction orders as a function of time for (g) beams 1&3, (h) beams 2&3, (i) beams 1&2. The colors stand for 0th (black), 1st (blue) and 2nd order (red). A lattice depth of $V_1 = 12.2(2)E_r$, $V_2 = 14.2(3)E_r$ and $V_3 = 16.4(3)E_r$ during calibration is deduced. The error is the 68% confidence interval of the fit.

So if we assume $\psi_0 = |k = 0\rangle$ we get

$$|\langle nk_{1D}|\psi(t)\rangle|^2 = \left[J_n\left(\frac{V_{1D}^{pp}t}{2\hbar} \right) \right]^2. \tag{C.5}$$

Hence the populations in the different diffraction orders evolve in time according to the respective Bessel function. A few example shots of this dynamics are shown in Fig. C.1a-f. We extract the populations of the diffraction peaks by summing over masks and fit these data points using the fit function

$$N_{in}(t) = A_{in} J_n^2 \left((t - t_0)V_i^{fit} \right) + C_{in}, \tag{C.6}$$

where N_{in} denotes the relative atom number in diffraction order $\pm n$ for 1D-lattice i. The important fit parameter is $V_i^{fit} = V_{1D}^{pp,i}/(2\hbar)$ which is half the angular frequency corresponding to the peak to peak 1D lattice depth. All orders of a single lattice are fitted with one lattice depth and the origin of time is the same for all measurements. The amplitude A_{in} and the offset C_{in} is fitted for each time trace individually. The fitted 1D lattice depth is proportional to the geometric mean of the intensities of the corresponding lattice beams. However, to obtain the correct band structure from a simulation we need to know the proportionality constant which in particular also depends on polarization. We determine the constant for the polarization approach by comparing the Hamiltonian matrix element for the coupling of momenta separated by one reciprocal lattice vector resulting from the lattice potential as written in (C.1)

and from the representation (B.11-B.13). For the latter we obtain

$$\left|\left\langle k=0\left|\hat{V}_{12}\right|k=k_{1\mathrm{D}}\right\rangle\right| = \frac{1}{2}\left|\sqrt{V_{1p}V_{2p}} - \sqrt{V_{1s}V_{2s}}e^{i\alpha_2}\right| \qquad = \frac{1}{2}\sqrt{V_1V_2}f_{12} \qquad \text{(C.7)}$$

$$\left|\left\langle k=0\left|\hat{V}_{23}\right|k=k_{1\mathrm{D}}\right\rangle\right| = \frac{1}{2}\left|\sqrt{V_{2p}V_{3p}} - \sqrt{V_{2s}V_{3s}}e^{i(\alpha_2-\alpha_3)}\right| \qquad = \frac{1}{2}\sqrt{V_2V_3}f_{23} \qquad \text{(C.8)}$$

$$\left|\left\langle k=0\left|\hat{V}_{13}\right|k=k_{1\mathrm{D}}\right\rangle\right| = \frac{1}{2}\left|\sqrt{V_{1p}V_{3p}} - \sqrt{V_{1s}V_{3s}}e^{i\alpha_3}\right| \qquad = \frac{1}{2}\sqrt{V_1V_3}f_{13} \qquad \text{(C.9)}$$

with the abbreviations $f_{12} = f(\theta,\alpha_2)$, $f_{23} = f(\theta,\alpha_2-\alpha_3)$, $f_{13} = f(\theta,\alpha_3)$, $f(\theta,\alpha) = |\cos^2\theta - 2\sin^2\theta\exp(i\alpha)|$. This has to be compared to the result when using (C.1):

$$\left\langle k_1|\hat{V}_{1\mathrm{D}}|k_2\right\rangle = \frac{1}{L}\int_0^L e^{ik_1x}\left[-V_{1\mathrm{D}}^{\mathrm{pp}}\sin^2\left(\frac{k_{1\mathrm{D}}x}{2}\right)\right]e^{-ik_2x}\mathrm{d}x \qquad \text{(C.10)}$$

$$= \frac{V_{1\mathrm{D}}^{\mathrm{pp}}}{4}\frac{1}{L}\int_0^L e^{ik_1x}(e^{ik_{1\mathrm{D}}x} + e^{-ik_{1\mathrm{D}}x} - 2)e^{-ik_2x}\mathrm{d}x \qquad \text{(C.11)}$$

$$= \frac{V_{1\mathrm{D}}^{\mathrm{pp}}}{4}\left(\langle k_1+k_{1\mathrm{D}}|k_2\rangle + \langle k_1-k_{1\mathrm{D}}|k_2\rangle - 2\langle k_1|k_2\rangle\right) \qquad \text{(C.12)}$$

$$= \frac{V_{1\mathrm{D}}^{\mathrm{pp}}}{4}\left(\delta_{k_1+k_{1\mathrm{D}},k_2} + \delta_{k_1-k_{1\mathrm{D}},k_2} - 2\delta_{k_1,k_2}\right) \qquad \text{(C.13)}$$

$$= \frac{V_{1\mathrm{D}}^{\mathrm{pp}}}{4} \quad \text{for} \quad |k_1-k_2| = k_{1\mathrm{D}} \qquad \text{(C.14)}$$

By equating the matrix elements that we obtain from the experiment with the theory expressions we get three equations

$$\frac{1}{2}\sqrt{V_1V_2}f_{12} = \frac{\hbar}{2}V_{12}^{\mathrm{fit}} \qquad \text{(C.15)}$$

$$\frac{1}{2}\sqrt{V_2V_3}f_{23} = \frac{\hbar}{2}V_{23}^{\mathrm{fit}} \qquad \text{(C.16)}$$

$$\frac{1}{2}\sqrt{V_3V_1}f_{31} = \frac{\hbar}{2}V_{31}^{\mathrm{fit}} \qquad \text{(C.17)}$$

$$\text{(C.18)}$$

which are solved by

$$V_1 = \frac{\hbar V_{12}^{fit}\hbar V_{31}^{fit}}{\hbar V_{23}^{fit}}\frac{f_{23}}{f_{12}f_{31}} = \hbar\frac{V_{12}^{\mathrm{fit}}V_{31}^{\mathrm{fit}}}{V_{23}^{\mathrm{fit}}}\frac{f_{23}}{f_{12}f_{31}} \qquad \text{(C.19)}$$

$$V_2 = \frac{\hbar V_{23}^{fit}\hbar V_{12}^{fit}}{\hbar V_{31}^{fit}}\frac{f_{31}}{f_{23}f_{12}} = \hbar\frac{V_{23}^{\mathrm{fit}}V_{12}^{\mathrm{fit}}}{V_{31}^{\mathrm{fit}}}\frac{f_{31}}{f_{23}f_{12}} \qquad \text{(C.20)}$$

$$V_3 = \frac{\hbar V_{31}^{fit}\hbar V_{23}^{fit}}{\hbar V_{12}^{fit}}\frac{f_{12}}{f_{31}f_{23}} = \hbar\frac{V_{31}^{\mathrm{fit}}V_{23}^{\mathrm{fit}}}{V_{12}^{\mathrm{fit}}}\frac{f_{12}}{f_{31}f_{23}}, \qquad \text{(C.21)}$$

allowing the reconstruction of the individual depths of the single beams which serve as an input parameter for the band structure calculation.

Conveniently, for the multi-frequency approach, no precise knowledge of the polarization is required. The couplings can be computed from (B.16 - B.18) as

$$\left|\left\langle k = 0 \middle| \hat{V}_{ij} \middle| k = k_{1\mathrm{D}}\right\rangle\right| = V_{ij,0}. \tag{C.22}$$

Thus the 1D lattice depths are connected to the fit results via

$$V_{ij,0} = \frac{\hbar V_{ij}^{\mathrm{fit}}}{2}. \tag{C.23}$$

For the calibration of the geometry phase φ_{g} we analyse the sublattice populations and identify the RF phase which corresponds to equal population, i.e., the honeycomb lattice. This phase corresponds to $\varphi_{\mathrm{g}} = 0$. See [57] for details.

C.2. Cross-check of magnification

We cross-checked the magnification of $M = 2.02$ with a free fall experiment. We released the atoms and waited for a variable time of flight before taking an image. For every image the center of the cloud is determined by a 2D Gaussian fit. In this way we get datapoints for position in pixels y_{pix} as a function of time of flight t_{tof} (Fig. C.2). We model the dynamics by a classical free fall

$$y_{\mathrm{pix}} = \frac{1}{L_{\mathrm{pix,atoms}}} \left[y_0 - \frac{1}{2} g(t_{\mathrm{tof}} - t_0)^2 \right], \tag{C.24}$$

with the length of a pixel in the atoms' plane $L_{\mathrm{pix,atoms}}$, the initial position y_0 and the origin of time t_0 as fit parameters. $g = 9.81\,\mathrm{m/s}^2$ is the gravitational acceleration. The
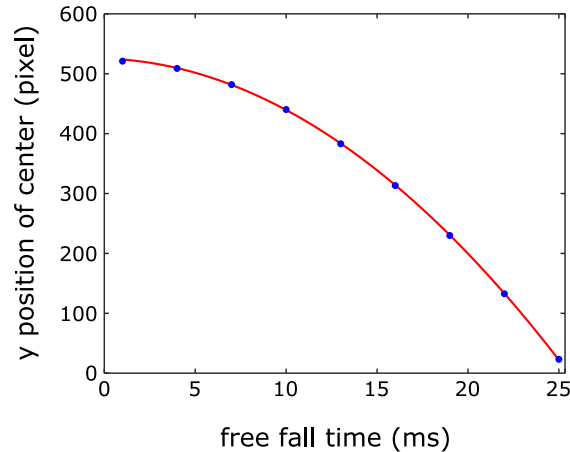
Figure C.2.: Free fall experiment for magnification cross-check. The *y*-position of the center of a Gaussian fit to the cloud is shown as a function of time of flight (circles). Errorbars are much smaller than the symbol size. The red line shows a free fall fit as described in the text.

magnification is then deduced via $M = L_{\text{pix,cam}}/L_{\text{pix,atoms}} = 2.04(2)$, where the error is propagated from the 68% confidence interval of the fit. Thus the used magnification of 2.02 can be confirmed.

C.3. Conversion from camera counts to intensity

When neglecting saturation effects it is sufficient to assume proportionality between camera counts and intensity for the analysis of the atom number. The proportionality constant cancels out in the computation. However, if saturation effects should be taken into account the absolute value of the intensity plays a role making it necessary to calculate the conversion factor from counts to intensity. It is given by

$$C = \frac{M^2}{A_{\text{pixel}}} \frac{E_\gamma}{C_{\text{AD}} \text{QE} \times \text{TE} \times t_{\text{expo}}}, \tag{C.25}$$

with the magnification $M = 2.02$, the pixel area $A_{\text{pixel}} = (13\,\mu\text{m})^2$, the photon energy $E_\gamma = h \times 384\,\text{THz}$, the conversion from analogue photo-electron signal to digital counts $C_{\text{AD}} = 0.26$, the quantum efficiency of the sensor $\text{QE} = 0.93$, the transmission of the imaging system $\text{TE} = 0.9$, and the exposure time $t_{\text{expo}} = 50\,\mu\text{s}$. A part of this factor is the conversion from digital counts to incident photons $C_\gamma = \frac{1}{C_{\text{AD}}\text{QE}\times\text{TE}} = 4.6$.

C.4. Lattice phase drifts

Our 2D lattice is made up of three lattice beams which can have independent phase drifts. These only shift the origin of the lattice but do not modify the lattice geometry [113]. We can extract the lattice origin for every measurement and we observe it to be not distinguishable from random, meaning that the phases are not stable between two consecutive experimental runs.

In order to investigate whether the lattice origin is stable for the time the lattice is actually on, we hold the atoms in a very deep lattice for a variable hold time t_{hold}. Since the lattice is deep it drags the atoms along when it moves which we verified by deliberately displacing the lattice in another experiment. From the random drifts of the lattice we expect a random walk which results in a linear increase of the variance of the position of the atoms for different runs. We extract the variance of the fitted center of the cloud for several hold times based on ~ 30 shots per time. We model the results by a random walk with an offset due to, e.g., mechanical instability of the setup, resulting in a fit function

$$\frac{\sigma^2_{x,y}}{a^2_{\text{latt}}} = t_{\text{hold}}/\tau_{x,y} + \frac{\sigma^2_{0,x,y}}{a^2_{\text{latt}}}. \tag{C.26}$$

The fitted datapoints are shown in Fig. C.3 resulting in $\tau_x = 52(19)\,\text{s}$ and $\tau_y = 27(16)\,\text{s}$ where the error is the 68% confidence interval of the fit. Clearly this is just an
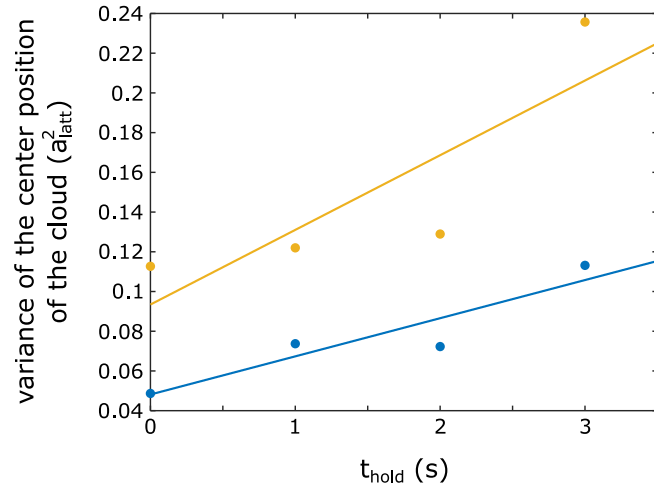
Figure C.3.: Measurement of lattice drifts. Variance of the position of the center of the atomic cloud (blue circles for x-position, ochre circles for y-position) obtained via a Gauss fit as a function of hold time after release. The data is fitted by a linear model as described in the main text (blue line for x-position, ochre line for y-position).

estimation of the drift time scale but we see that it is much larger than experimental time scales of typically few milliseconds to hundreds of milliseconds of hold time in the lattice. We therefore conclude that lattice drifts do not play a role for our observations.

Appendix D.

Data analysis routines

D.1. Extraction of on-site populations

Even though the quantum gas magnifier gives access to sub-lattice site information, for many experiments this information is not relevant or destroyed by the freezing and trap ramping protocol if applied. In these cases we reduce the information of the images to the on-site populations by summing over the density within the Wigner-Seitz cells of the lattice. To this end, we need to determine two parameters: The lattice constant and the lattice origin. Let us start with the algorithm for a triangular lattice. The lattice constant is obtained by fitting a phenomenological function

$$n_{1D}(x) = A e^{-\frac{(x-x_0)^2}{2\sigma^2}} \left[\cos^2 \left(\frac{\pi x}{a_{1D}} + \phi \right) + B \right] \tag{D.1}$$

to the density integrated along y and independently to the density integrated along the direction $-\sqrt{3}/2\boldsymbol{e}_x + 1/2\boldsymbol{e}_y$. The fit parameters are A, x_0, σ, a_{1D}, ϕ, and B and are averaged among all shots and integration directions. The lattice constant of the triangular lattice is then given by $a_{lat} = 2a_{1D}/\sqrt{3}$. The lattice origin is obtained by adjusting the origin of a triangular lattice of circular masks such that the density which is not covered by the circles is minimal. The origin is displaced in a number of steps equal to the rounded lattice constant in pixels from zero to one step less than one lattice vector which would be equivalent to zero displacement. We do not have a phase lock for our lattice beams and even though the lattice origin is stable during the hold times in the lattice it is quasi random for consecutive shots (appendix C.4) making the origin determination necessary for every individual image.

Once the lattice is known, the density is summed over the Wigner-Seitz cells. To reduce aberrations from the finite pixel size, the pixels are refined by replacing every pixel by $(2^{N_{refine}})^2$ subpixels with an atom number equal to the parent atom number divided by the number of subpixels to keep the total atom number fixed. N_{refine} is adjusted depending on the lattice constant as $N_{refine} = \lceil \log_2(10/r_{WS}) \rceil$ with $r_{WS} = 2/\sqrt{3} \times \frac{a_{lat}}{2}$ being the outer radius of the Wigner Seitz cell in pixels. In this way the Wigner-Seitz cell always contains $\sim 10^2$ subpixel. The Wigner-Seitz cells are then implemented as polygons in a continuum and the sum is carried out over all subpixels with their center within the relevant polygon.
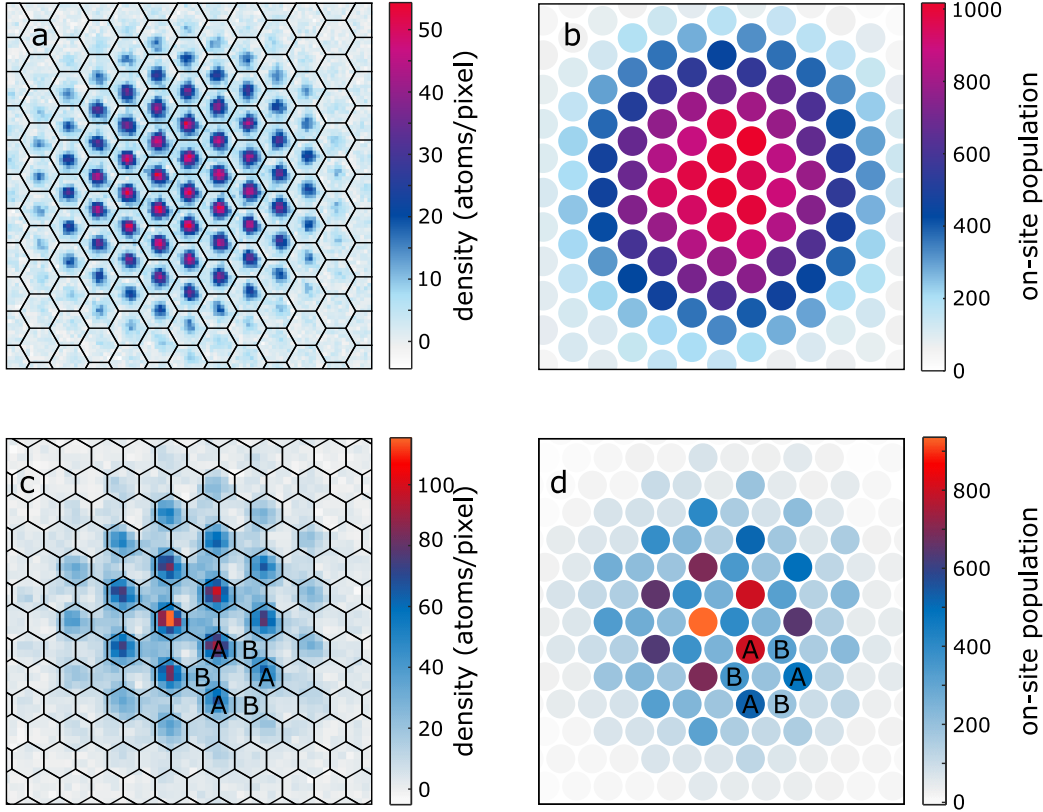
Figure D.1.: Computation of the on-site populations. **(a)**, example density image of a triangular lattice. The Wigner-Seitz cells are determined as described in the text and shown as hexagons in the figure. **(b)**, on-site populations resulting from (a) via summation in the Wigner-Seitz cells. **(c)**, example density image of a boron-nitride lattice. The hexagons show the read-out masks, obtained as described in the text. Six sites are examplarily labelled according to the sublattice they belong to (A or B) to show one honeycomb of the lattice. **(d)**, on-site populations resulting from (d) via summation in the Wigner-Seitz cells. The same lattice sites are labelled as in (c). (a,b) Adapted from [22].

An example image with an overlay of the used polygons can be seen in Fig. D.1a. The resulting on-site populations are plotted in Fig. D.1b.

For the case of a boron-nitride lattice the analysis is similar because for the experiments presented in this thesis the on-site populations were only extracted for situations where one of the two sublattices had most of the population. Therefore this sublattice can be located using the algorithm for a triangular lattice described above. After this location the read-out masks need to be placed differently. In fact a triangular lattice with primitive vectors consisting of a vector between the sublattices and one rotated by 60° is used. This results in the read-out of three triangular sublattices: Two of them corresponding to the actual sublattices and one corresponding to the locations of the potential maxima in the centres of the honeycombs. An

example is given in Fig. D.1c,d. Of course it would be straightforward to generalize the lattice location algorithm to the case of equally populated sublattices by adapting the fit function for the projections and by identifying the phase by maximizing the unmasked population. This would be necessary for uniqueness since the minimizing procedure could identify either of the two sublattices whereas maximizing the unmasked population would uniquely identify the positions of the potential maxima.

D.2. Computation of uncertainty of correlations

Recall that the computation of the correlations are based on the covariance

$$\text{cov}_{jk} = \frac{1}{N-1} \sum_{i=1}^{N} \delta N_j^{(i)} \delta N_k^{(i)}. \tag{D.2}$$

of the residues. The error of the covariance is computed by considering the spread of the fluctuations relative to the best estimate of the covariance, i.e.,

$$\Delta \text{cov}_{jk} = \sqrt{\frac{1}{N} \sum_{i=1}^{N} (\text{cov}_{jk}^{(i)} - \text{cov}_{jk})^2}, \tag{D.3}$$

where $\text{cov}_{jk}^{(i)} = \delta N_j^{(i)} \delta N_k^{(i)}$. This error is then propagated when computing the mean for identical or exactly opposite distance vectors.

D.3. Defringing algorithm

As described in the main text, pointing instabilities between absorption and reference image can cause artefacts in the form of fringes on the results of the absorption imaging analysis. These artefacts can be greatly reduced by using a linear combination of reference images from a set of reference images instead of the single reference image that was taken in the same run. The concept is that the imaging beam has a certain instantaneous profile on a absorption image that is likely to change until the reference image is taken but that there is a high probability that the same profile as on the absorption image will be recorded later on another reference image. The defringing algorithm described here is based on the one introduced in [114–116] and its current implementation is described in [117].

Let us consider a single example absorption image $\boldsymbol{a}^{\text{T}} = (a_1, a_2, ..., a_N)$ which has been rearranged from a rectangular matrix to a column vector. A region of interest around the atomic cloud but excluding it is defined and only this region is considered in the following. Thus, conceptually, the absorption and reference images should be identical in this region. To obtain a reference image that comes as close as possible to this condition we construct such an optimal reference image $\boldsymbol{r}_{\text{opt}}$ starting from a

linear combination

$$\boldsymbol{r}_{\mathrm{opt}} = R\boldsymbol{c} \tag{D.4}$$

of all reference images under consideration $\boldsymbol{r}_1$, $\boldsymbol{r}_2$, ... , $\boldsymbol{r}_M$ which are combined into the matrix $R = (\boldsymbol{r}_1, \boldsymbol{r}_2, ..., \boldsymbol{r}_M)$. The coefficients of the linear combination are the elements of the vector $\boldsymbol{c}$. The optimal reference image should be as close as possible to the absorption image under consideration, where we choose least squares as the metric to measure closeness, i.e.

$$|R\boldsymbol{c} - \boldsymbol{a}|^2 \stackrel{!}{=} \min. \tag{D.5}$$

This minimization is achieved by choosing [118]

$$\boldsymbol{c} = \left(R^{\mathrm{T}}R\right)^{-1} R^{\mathrm{T}}\boldsymbol{a}. \tag{D.6}$$

Eventually the defringed atomic density is computed in the standard way, just using the optimal reference image instead of the reference image from the same run.

Bibliography

[1] P. W. Higgs: "Broken symmetries and the masses of gauge bosons", Physical Review Letters **13** (16), 508–509 (1964). 1, 43

[2] F. Englert and R. Brout: "Broken symmetry and the mass of gauge vector mesons", Physical Review Letters **13** (9), 321–323 (1964). 1, 43

[3] M. C. Cross and P. C. Hohenberg: "Pattern formation outside of equilibrium", Reviews of Modern Physics **65** (3), 851–1112 (1993). 1

[4] O. G. Mouritsen: "Pattern formation in condensed matter", International Journal of Modern Physics B **04** (13), 1925–1954 (1990). 1

[5] F. T. Arecchi, S. Boccaletti and P. Ramazza: "Pattern formation and competition in nonlinear optics", Physics Reports **318**, 1–83 (1999). 1

[6] J. Miles: "On Faraday waves", Journal of Fluid Mechanics **248**, 671–683 (1993). 1

[7] E. Bodenschatz, W. Pesch and G. Ahlers: "Recent developments in Rayleigh-Bénard convection", Annu. Rev. Fluid Mech **32**, 709–778 (2000). 1

[8] A. M. Turing: "The chemical basis of morphogenesis", Philosophical Transactions of the Royal Society of London. Series B, Biological Sciences **237** (641), 37–72 (1952). 1

[9] P. K. Maini, K. J. Painter and H. N. P. Chau: "Spatial pattern formation in chemical and biological systems", Journal of the Chemical Society - Faraday Transactions **93** (20), 3601–3610 (1997). 1

[10] I. Bloch, J. Dalibard and S. Nascimbène: "Quantum simulations with ultracold quantum gases", Nature Physics **8** (4), 267–276 (2012). 1

[11] J. Simon, W. S. Bakr, R. Ma, M. E. Tai, P. M. Preiss and M. Greiner: "Quantum simulation of antiferromagnetic spin chains in an optical lattice", Nature **472** (7343), 307–312 (2011). 1, 44

[12] S. Sachdev, K. Sengupta and S. M. Girvin: "Mott insulators in strong electric fields", Physical Review B **66** (7), 075128 (2002).

[13] R. Ma, M. E. Tai, P. M. Preiss, W. S. Bakr, J. Simon and M. Greiner: "Photon-assisted tunneling in a biased strongly correlated bose gas", Physical Review Letters **107** (9), 095301 (2011). 1, 44

[14] H. Bernien, S. Schwartz, A. Keesling, H. Levine, A. Omran, H. Pichler, S. Choi, A. S. Zibrov, M. Endres, M. Greiner, V. Vuletic and M. D. Lukin: "Probing many-body dynamics on a 51-atom quantum simulator", Nature **551** (7682), 579–584 (2017). 1, 44

[15] Z. Zhang, K. X. Yao, L. Feng, J. Hu and C. Chin: "Pattern formation in a driven Bose–Einstein condensate", Nature Physics **16** (6), 652–656 (2020). 1, 44

[16] F. Böttcher, J. N. Schmidt, J. Hertkorn, K. S. Ng, S. D. Graham, M. Guo, T. Langen and T. Pfau: "New states of matter with fine-tuned interactions: quantum droplets and dipolar supersolids", Reports on Progress in Physics **84** (1), 012403 (2020). 1, 44

[17] B. Eiermann, P. Treutlein, T. Anker, M. Albiez, M. Taglieber, K. P. Marzlin and M. K. Oberthaler: "Dispersion Management for Atomic Matter Waves", Physical Review Letters **91** (6) (2003). 1

[18] L. Fallani, L. De Sarlo, J. E. Lye, M. Modugno, R. Saers, C. Fort and M. Inguscio: "Observation of dynamical instability for a Bose-Einstein condensate in a moving 1D optical lattice", Physical Review Letters **93** (14), 140406 (2004).

[19] M. Cristiani, O. Morsch, N. Malossi, M. Jona-Lasinio, M. Anderlini, E. Courtade and E. Arimondo: "Instabilities of a Bose-Einstein condensate in a periodic potential: an experimental investigation", Optics Express **12** (1), 4 (2004). 1

[20] N. Gemelke, E. Sarajlic, Y. Bidel, S. Hong and S. Chu: "Parametric amplification of matter waves in periodically translated optical lattices", Physical Review Letters **95** (17), 170404 (2005). 1

[21] T. Anker, M. Albiez, R. Gati, S. Hunsmann, B. Eiermann, A. Trombettoni and M. K. Oberthaler: "Nonlinear self-trapping of matter waves in periodic potentials", Physical Review Letters **94** (2), 020403 (2005). 1, 57

[22] L. Asteria, H. P. Zahn, M. N. Kosch, K. Sengstock and C. Weitenberg: "Quantum gas magnifier for sub-lattice-resolved imaging of 3D quantum systems", Nature **599** (7886), 571–575 (2021). 1, 20, 21, 25, 28, 30, 41, 67, 86, 96

[23] I. Shvarchuck, C. Buggle, D. S. Petrov, K. Dieckmann, M. Zielonkowski, M. Kemmann, T. G. Tiecke, W. von Klitzing, G. V. Shlyapnikov and J. T. M. Walraven: "Bose-Einstein Condensation into Nonequilibrium States Studied by Condensate Focusing", Physical Review Letters **89** (27), 270404 (2002). 2

[24] K. Hueck, N. Luick, L. Sobirey, J. Siegl, T. Lompe and H. Moritz: "Two-Dimensional Homogeneous Fermi Gases", Physical Review Letters **120** (6), 060402 (2018). 2

[25] S. Tung, G. Lamporesi, D. Lobser, L. Xia and E. A. Cornell: "Observation of the presuperfluid regime in a two-dimensional bose gas", Physical Review Letters **105** (23), 230408 (2010).

[26] P. A. Murthy, D. Kedar, T. Lompe, M. Neidig, M. G. Ries, A. N. Wenz, G. Zürn and S. Jochim: "Matter-wave Fourier optics with a strongly interacting two-dimensional Fermi gas", Physical Review A **90** (4), 43611 (2014).

[27] P. A. Murthy, I. Boettcher, L. Bayha, M. Holzmann, D. Kedar, M. Neidig, M. G. Ries, A. N. Wenz, G. Zürn and S. Jochim: "Observation of the Berezinskii-Kosterlitz-Thouless Phase Transition in an Ultracold Fermi Gas", Physical Review Letters **115** (1), 010401 (2015).

[28] P. T. Brown, E. Guardado-Sanchez, B. M. Spar, E. W. Huang, T. P. Devereaux and W. S. Bakr: "Angle-resolved photoemission spectroscopy of a Fermi–Hubbard system", Nature Physics **16** (1), 26–31 (2020). 2

[29] P. A. Murthy and S. Jochim: "Direct imaging of the order parameter of an atomic superfluid using matterwave optics", arXiv preprint 1911.10824 (2019). 2, 67

[30] J. F. Sherson, C. Weitenberg, M. Endres, M. Cheneau, I. Bloch and S. Kuhr: "Single-atom-resolved fluorescence imaging of an atomic Mott insulator", Nature **467** (7311), 68–72 (2010). 2, 15, 38

[31] W. S. Bakr, A. Peng, M. E. Tai, R. Ma, J. Simon, J. I. Gillen, S. Fölling, L. Pollet and M. Greiner: "Probing the Superfluid–to–Mott Insulator Transition at the Single-Atom Level", Science **329** (5991), 547–550 (2010). 15, 38

[32] S. Kuhr: "Quantum-gas microscopes: A new tool for cold-atom quantum simulators", National Science Review **3** (2), 170–172 (2016). 2, 15

[33] T. Gericke, P. Würtz, D. Reitz, T. Langen and H. Ott: "High-resolution scanning electron microscopy of an ultracold quantum gas", Nature Physics **4** (12), 949–953 (2008). 2, 15, 31

[34] C. Veit, N. Zuber, O. A. Herrera-Sancho, V. S. Anasuri, T. Schmid, F. Meinert, R. Low and T. Pfau: "Pulsed Ion Microscope to Probe Quantum Gases", Physical Review X **11** (1), 011036 (2021). 2

[35] M. McDonald, J. Trisnadi, K. X. Yao and C. Chin: "Superresolution Microscopy of Cold Atoms in an Optical Lattice", Physical Review X **9** (2), 021001 (2019). 2, 31

[36] S. Subhankar, Y. Wang, T. C. Tsui, S. L. Rolston and J. V. Porto: "Nanoscale Atomic Density Microscopy", Physical Review X **9** (2), 021002 (2019). 2, 31

[37] D. J. Thouless: *The quantum mechanics of many-body systems*, Academic Press, 2nd edition (1972), ISBN 978-0-486-49357-2. 5

[38] R. P. Feynman: "Simulating physics with computers", International Journal of Theoretical Physics **21** (6-7), 467–488 (1982). 5

[39] R. Dinter: "Aufbau und Charakterisierung einer Magnetfalle zur simultanen Speicherung von K und Rb", Diplomarbeit, Universität Hamburg (2004). 5, 7, 8, 84

[40] C. Ospelkaus: "Fermi-Bose mixtures – From mean-field interactions to ultracold chemistry", Ph.D. thesis, Universität Hamburg (2006). 8

[41] S. Ospelkaus-Schwarzer: "Quantum Degenerate Fermi-Bose Mixtures of ^{40}K and ^{87}Rb in 3D Optical Lattices", Ph.D. thesis, Universität Hamburg (2006). 5, 7

[42] C. Gross and I. Bloch: "Quantum simulations with ultracold atoms in optical lattices", Science **357** (6355), 995–1001 (2017). 5

[43] M. H. Anderson, J. R. Ensher, M. R. Matthews, C. E. Wieman and E. A. Cornell: "Observation of Bose-Einstein Condensation in a Dilute Atomic Vapor", Science **269** (5221), 198–201 (1995). 5

[44] K. B. Davis, M. O. Mewes, M. R. Andrews, N. J. Van Druten, D. S. Durfee, D. M. Kurn and W. Ketterle: "Bose-Einstein condensation in a gas of sodium atoms", Physical Review Letters **75** (22), 3969–3973 (1995). 5

[45] B. DeMarco and D. S. Jin: "Onset of Fermi degeneracy in a trapped atomic gas", Science **285** (5434), 1703–1706 (1999). 5

[46] M. Greiner, O. Mandel, T. Esslinger, T. W. Hänsch and I. Bloch: "Quantum phase transition from a superfluid to a mott insulator in a gas of ultracold atoms", Nature **415** (6867), 39–44 (2002). 5, 38

[47] C. A. Regal, M. Greiner and D. S. Jin: "Observation of Resonance Condensation of Fermionic Atom Pairs", Physical Review Letters **92** (4), 4 (2004). 5

[48] M. W. Zwierlein, C. A. Stan, C. H. Schunck, S. M. Raupach, A. J. Kerman and W. Ketterle: "Condensation of pairs of fermionic atoms near a Feshbach resonance", Physical Review Letters **92** (12) (2004). 5

[49] G. Jotzu, M. Messer, R. Desbuquois, M. Lebrat, T. Uehlinger, D. Greif and T. Esslinger: "Experimental realization of the topological Haldane model with ultracold fermions", Nature **515** (7526), 237–240 (2014). 5

[50] M. Aidelsburger, M. Lohse, C. Schweizer, M. Atala, J. T. Barreiro, S. Nascimbène, N. R. Cooper, I. Bloch and N. Goldman: "Measuring the Chern number of Hofstadter bands with ultracold bosonic atoms", Nature Physics **11** (2), 162–166 (2015). 5

[51] A. Mazurenko, C. S. Chiu, G. Ji, M. F. Parsons, M. Kanász-Nagy, R. Schmidt, F. Grusdt, E. Demler, D. Greif and M. Greiner: "A cold-atom Fermi-Hubbard antiferromagnet", Nature **545** (7655), 462–466 (2017). 5

[52] M. Weinberg: "Observation of the amplitude mode in strongly correlated Bose-Einstein condensates", Diplomarbeit, Universität Hamburg (2010). 6

[53] E. L. Raab, M. Prentiss, A. Cable, S. Chu and D. E. Pritchard: "Trapping of Neutral Sodium Atoms with Radiation Pressure", Phys. Rev. Lett. **59** (23), 2631–2634 (1987). 6

[54] D. A. Steck: "Rubidium 87 D Line Data", available online at http://steck.us/alkalidata (2022). 7, 13, 70

[55] R. Grimm, M. Weidemüller and Y. B. Ovchinnikov: "Optical Dipole Traps for Neutral Atoms", Advances in Atomic, Molecular and Optical Physics **42** (C), 95–170 (2000). 9, 10

[56] N. Fläschner: "Ultracold Fermions in Tunable Hexagonal Lattices: From High-Precision Spectroscopy to the Measurement of Berry Curvature", Ph.D. thesis, Universität Hamburg (2016). 9, 10, 11, 71, 79

[57] L. Asteria: "Quantum Gas Magnifier for imaging of ultracold Atoms in highly tunable optical Lattices", Ph.D. thesis, Universität Hamburg (2022). 11, 13, 20, 33, 67, 92

[58] O. Stenzel: *Light–Matter Interaction*, Springer International Publishing, Cham, 1st edition (2022), ISBN 978-3-030-87143-7. 13

[59] G. Reinaudi, T. Lahaye, Z. Wang and D. Guéry-Odelin: "Strong saturation absorption imaging of dense clouds of ultracold atoms", Opt. Lett. **32** (21), 3143–3145 (2007). 13

[60] W. Nolting: *Theoretical Physics 2 : Analytical Mechanics*, Springer International Publishing, Cham (2016), ISBN 978-3-319-40129-4. 16

[61] D. McKay, M. White and B. DeMarco: "Lattice thermodynamics for ultracold atoms", Physical Review A **79** (6), 063605 (2009). 22

[62] S. Trotzky, L. Pollet, F. Gerbier, U. Schnorrberger, I. Bloch, N. V. Prokof'ev, B. Svistunov and M. Troyer: "Suppression of the critical temperature for superfluidity near the Mott transition", Nature Physics **6** (12), 998–1004 (2010).

[63] H. Cayla, C. Carcy, Q. Bouton, R. Chang, G. Carleo, M. Mancini and D. Clément: "Single-atom-resolved probing of lattice gases in momentum space", Physical Review A **97** (6), 061609 (2018). 22

[64] L. Pitaevskii and S. Stringari: *Bose-Einstein Condensation and Superfluidity*, Oxford University Press (2016). 22

[65] C. J. Pethick and H. Smith: *Bose–Einstein condensation in dilute gases*, Cambridge University Press, Cambridge (2008), ISBN 978-0-511-80285-0. 22, 24, 26, 85

[66] J. R. Ensher, D. S. Jin, M. R. Matthews, C. E. Wieman and E. A. Cornell: "Bose-einstein condensation in a dilute gas: Measurement of energy and ground-state occupation", Physical Review Letters **77** (25), 4984–4987 (1996). 26

[67] S. Giorgini, L. P. Pitaevskii and S. Stringari: "Condensate fraction and critical temperature of a trapped interacting Bose gas", Physical Review A **54** (6), R4633–R4636 (1996). 26

[68] R. P. Smith, R. L. Campbell, N. Tammuz and Z. Hadzibabic: "Effects of interactions on the critical temperature of a trapped bose gas", Physical Review Letters **106** (25) (2011). 26

[69] W. Ketterle and N. J. van Druten: "Bose-Einstein condensation of a finite number of particles trapped in one or three dimensions", Physical Review A **54** (1), 656–660 (1996). 26

[70] P. Würtz, T. Langen, T. Gericke, A. Koglbauer and H. Ott: "Experimental demonstration of single-site addressability in a two-dimensional optical lattice", Physical Review Letters **103** (8), 080404 (2009). 27

[71] C. Weitenberg, M. Endres, J. F. Sherson, M. Cheneau, P. Schau, T. Fukuhara, I. Bloch and S. Kuhr: "Single-spin addressing in an atomic Mott insulator", Nature **471** (7338), 319–325 (2011). 27

[72] P. M. Preiss, R. Ma, M. E. Tai, A. Lukin, M. Rispoli, P. Zupancic, Y. Lahini, R. Islam and M. Greiner: "Strongly correlated quantum walks in optical lattices", Science **347** (6227), 1229–1233 (2015). 27

[73] M. Karski, L. Förster, J. M. Choi, A. Steffen, N. Belmechri, W. Alt, D. Meschede and A. Widera: "Imprinting patterns of neutral atoms in an optical lattice using magnetic resonance techniques", New Journal of Physics **12** (6), 065027 (2010). 27

[74] P. B. Wigley, L. M. Starkey, S. S. Szigeti, M. Jasperse, J. J. Hope, L. D. Turner and R. P. Anderson: "Precise wave-function engineering with magnetic resonance", Physical Review A **96** (1), 013612 (2017). 27

[75] H. Schmaljohann, M. Erhard, J. Kronjäger, M. Kottke, S. van Staa, L. Cacciapuoti, J. J. Arlt, K. Bongs and K. Sengstock: "Dynamics of $F = 2$ Spinor Bose-Einstein Condensates", Physical Review Letters **92** (4), 4 (2004). 27

[76] A. M. Kaufman, M. E. Tai, A. Lukin, M. Rispoli, R. Schittko, P. M. Preiss and M. Greiner: "Quantum thermalization through entanglement in an isolated many-body system", Science **353** (6301), 794–800 (2016). 29

[77] M. Schreiber, S. S. Hodgman, P. Bordia, H. P. Lüschen, M. H. Fischer, R. Vosk, E. Altman, U. Schneider and I. Bloch: "Observation of many-body localization of interacting fermions in a quasirandom optical lattice", Science **349** (6250), 842–845 (2015). 29

[78] J. Y. Choi, S. Hild, J. Zeiher, P. Schauß, A. Rubio-Abadal, T. Yefsah, V. Khemani, D. A. Huse, I. Bloch and C. Gross: "Exploring the many-body localization transition in two dimensions", Science **352** (6293), 1547–1552 (2016). 29

[79] C. Vallance: *An Introduction to Chemical Kinetics*, Morgan & Claypool Publishers, San Rafael, CA, USA (2017), ISBN 978-1-6817-4664-7. 30

[80] W. Nolting: *Theoretical Physics 8 : Statistical Physics*, Springer International Publishing, Cham (2018), ISBN 978-3-319-73827-7. 34

[81] N. Gemelke, X. Zhang, C. L. Hung and C. Chin: "In situ observation of incompressible Mott-insulating domains in ultracold atomic gases", Nature **460** (7258), 995–998 (2009). 38

[82] M. Greiner, O. Mandel, T. W. Hänsch and I. Bloch: "Collapse and revival of the matter wave field of a Bose-Einstein condensate", Nature **419** (6902), 51–54 (2002). 38

[83] M. Yamashita, S. Kato, A. Yamaguchi, S. Sugawa, T. Fukuhara, S. Uetake and Y. Takahashi: "Strongly interacting array of Bose-Einstein condensates trapped in a one-dimensional optical lattice", Physical Review A **87** (4) (2013). 39

[84] J. D. Patterson and B. C. Bailey: *Solid-State Physics*, Springer International Publishing, Cham, 3rd edition (2007), ISBN 978-3-319-75322-5. 39

[85] W. Zwerger: "Mott-Hubbard transition of cold atoms in optical lattices", Journal of Optics B: Quantum and Semiclassical Optics **5** (2), 9–16 (2003). 39

[86] D. van Oosten, P. van der Straten and H. T. C. Stoof: "Quantum phases in an optical lattice", Physical Review A **63** (5), 053601 (2001). 41

[87] S. Fölling: "Probing Strongly Correlated States of Ultracold Atoms in Optical Lattices", Ph.D. thesis, Mainz (2008). 41

[88] S. Burger, F. S. Cataliotti, C. Fort, F. Minardi, M. Inguscio, M. L. Chiofalo and M. P. Tosi: "Superfluid and dissipative dynamics of a Bose-Einstein condensate in a periodic optical potential", Physical Review Letters **86** (20), 4447–4450 (2001). 44

[89] N. D. Oppong, G. Pasqualetti, O. Bettermann, P. Zechmann, M. Knap, I. Bloch and S. Fölling: "Probing transport and slow relaxation in the mass-imbalanced Fermi-Hubbard model", arXiv preprint 2011.12411 (2020). 44

[90] H. P. Zahn, V. P. Singh, M. N. Kosch, L. Asteria, L. Freystatzky, K. Sengstock, L. Mathey and C. Weitenberg: "Formation of Spontaneous Density-Wave Patterns in dc Driven Lattices", Physical Review X **12** (2), 021014 (2022). 46, 47, 52, 55, 56, 57, 59, 62, 63, 64, 65

[91] W. Magnus: "On the exponential solution of differential equations for a linear operator", Communications on Pure and Applied Mathematics **7** (4), 649–673 (1954). 46

[92] S. Blanes, F. Casas, J. A. Oteo and J. Ros: "The Magnus expansion and some of its applications", Physics Reports **470** (5-6), 151–238 (2009).

[93] B. Zhu, T. Rexin and L. Mathey: "Magnus expansion approach to parametric oscillator systems in a thermal bath", Zeitschrift für Naturforschung A **71** (10), 921–932 (2016). 46

[94] O. Dutta, M. Gajda, P. Hauke, M. Lewenstein, D. S. Lühmann, B. A. Malomed, T. Sowiński and J. Zakrzewski: "Non-standard Hubbard models in optical lattices: a review", Reports on Progress in Physics **78** (6), 066001 (2015). 47, 67

[95] V. P. Singh, W. Weimer, K. Morgener, J. Siegl, K. Hueck, N. Luick, H. Moritz and L. Mathey: "Probing superfluidity of Bose-Einstein condensates via laser stirring", Physical Review A **93** (2), 023634 (2016). 49

[96] E. Guardado-Sanchez, A. Morningstar, B. M. Spar, P. T. Brown, D. A. Huse and W. S. Bakr: "Subdiffusion and Heat Transport in a Tilted Two-Dimensional Fermi-Hubbard System", Physical Review X **10** (1), 011042 (2020). 56

[97] S. Scherg, T. Kohlert, P. Sala, F. Pollmann, B. Hebbe Madhusudhana, I. Bloch and M. Aidelsburger: "Observing non-ergodicity due to kinetic constraints in tilted Fermi-Hubbard chains", Nature Communications **12** (1), 1–8 (2021). 56

[98] F. S. Cataliotti, S. Burger, C. Fort, P. Maddaloni, F. Minardi, A. Trombettoni, A. Smerzi and M. Inguscio: "Josephson junction arrays with Bose-Einstein condensates", Science **293** (5531), 843–846 (2001). 66

[99] A. Bergschneider, V. M. Klinkhamer, J. H. Becher, R. Klemt, G. Zürn, P. M. Preiss and S. Jochim: "Spin-resolved single-atom imaging of ^{6}Li in free space", Physical Review A **97** (6), 063613 (2018). 67

[100] Jochim-group: *conference talk* (2022). 67

[101] X. Q. Wang, G. Q. Luo, J. Y. Liu, W. V. Liu, A. Hemmerich and Z. F. Xu: "Evidence for an atomic chiral superfluid with topological excitations", Nature **596** (7871), 227–231 (2021). 67

[102] B. Santra, C. Baals, R. Labouvie, A. B. Bhattacherjee, A. Pelster and H. Ott: "Measuring finite-range phase coherence in an optical lattice using Talbot interferometry", Nature Communications **8** (1), 1–8 (2017). 67

[103] D. S. Lühmann: "Twisted superfluid phase in the extended one-dimensional Bose-Hubbard model", Physical Review A **94** (1), 011603 (2016). 67

[104] J. Struck, C. Ölschläger, R. Le Targat, P. Soltan-Panahi, A. Eckardt, M. Lewenstein, P. Windpassinger and K. Sengstock: "Quantum simulation of frustrated classical magnetism in triangular optical lattices", Science **333** (6045), 996–999 (2011). 67

[105] J. Struck, M. Weinberg, C. Ölschläger, P. Windpassinger, J. Simonet, K. Sengstock, R. Höppner, P. Hauke, A. Eckardt, M. Lewenstein and L. Mathey: "Engineering Ising-XY spin-models in a triangular lattice using tunable artificial gauge fields", Nature Physics **9** (11), 738–743 (2013).

[106] C. V. Parker, L. C. Ha and C. Chin: "Direct observation of effective ferromagnetic domains of cold atoms in a shaken optical lattice", Nature Physics **9** (12), 769–774 (2013). 67

[107] S. Baier, M. J. Mark, D. Petter, K. Aikawa, L. Chomaz, Z. Cai, M. Baranov, P. Zoller and F. Ferlaino: "Extended Bose-Hubbard models with ultracold magnetic atoms", Science **352** (6282), 201–205 (2016). 67

[108] S. Mukherjee and M. C. Rechtsman: "Observation of Floquet solitons in a topological bandgap", Science **368** (6493), 856–859 (2020). 68

[109] A. Kshetrimayum, J. Eisert and D. M. Kennes: "Stark time crystals: Symmetry breaking in space and time", Physical Review B **102** (19), 195116 (2020). 68

[110] B. Irsigler, J. H. Zheng and W. Hofstetter: "Interacting Hofstadter Interface", Physical Review Letters **122** (1) (2019). 68

[111] F. Bloch: "Über die Quantenmechanik der Elektronen in Kristallgittern", Zeitschrift für Physik **52** (7-8), 555–600 (1929). 79

[112] S. Gupta, A. E. Leanhardt, A. D. Cronin and D. E. Pritchard: "Coherent manipulation of atoms with standing light waves", Comptes Rendus de l'Académie des Sciences - Series IV - Physics **2** (3), 479–495 (2001). 89

[113] K. I. Petsas, A. B. Coates and G. Grynberg: "Crystallography of optical lattices", Physical Review A **50** (6), 5173–5189 (1994). 93

[114] M. Erhard: "Experimente mit mehrkomponentigen Bose-Einstein-Kondensaten", Ph.D. thesis, Universität Hamburg (2004). 97

[115] J. Kronjaeger: "Coherent Dynamics of Spinor Bose-Einstein Condensates", Ph.D. thesis, Universität Hamburg (2007).

[116] C. F. Ockeloen, A. F. Tauschinsky, R. J. Spreeuw and S. Whitlock: "Detection of small atom numbers through image processing", Physical Review A **82** (6), 061606 (2010). 97

[117] D. Vogel: "Measuring Geometry and Topology of Floquet-Bloch States in and out of Equilibrium with ultracold fermions", Ph.D. thesis, Universität Hamburg (2018). 97

[118] C. L. Lawson and R. J. Hanson: *Solving least squares problems*, Society for industrial and applied mathematics, 1st edition (1995), ISBN 978-0-89871-356-5. 98

Acknowledgements

I am grateful to many people for their support during the course of this thesis.

First of all I want to thank Klaus for giving me the opportunity to pursue a PhD at the bfm experiment. I felt very welcome from the first day and got all the support I needed. Next I want to thank Christof for his great motivation, probably endless experimental proposals and the great discussions. It was really great for me to have such an experienced scientist that I can always talk to. Sometimes I got the impression that Christof knows every paper that was ever published. Furthermore I want to thank my PhD colleagues Luca and Marcel. I had a great time working with you. Luca, your creativity concerning experimental protocols is unmatched. Marcel, you really mastered the experimental control bringing the quality of the magnifier images to perfection. I also want to thank the whole team Sengstock for the great working atmosphere and fun moments. In particular I want to mention Ortwin who picked up an unconventional but great idea to solve our vacuum problems by a treatment of the helicoflex gasket with Fixogum.

I am also grateful to Ludwig, Vijay and Lukas for the fruitful collaboration on the density-wave project. The theoretical understanding we gained by your contribution took the project to another level. I enjoyed the great discussions we had that deepened the understanding of the phenomenon and triggered new experimental perspectives and analyses.

Last but not least I want to thank my family which always supported me – during the thesis and before.